UNIONE EUROPEA
Fondo Sociale Europeo

Ministero dell'Università e della Ricerca

PON RICERCA E INNOVAZIONE 2014-2020

UNIVERSITÀ DEGLI STUDI DI NAPOLI FEDERICO II

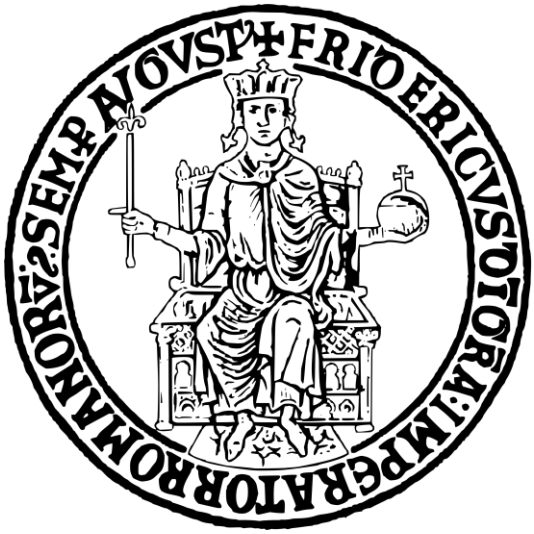

Industrial Engineering Department

XXXV Ph.D. Cycle

Ph.D. Thesis

Characterization and Thermal Aging Tests of Selective Solar Absorbers for Evacuated Flat Plate Collectors

Tutor:

Prof. Marilena Musto

Supervisor:

Dr. Roberto Russo

Candidate:

Antonio Caldarelli

Table of contents

Abstract

Solar energy plays a key role in the energy transition from fossil fuels to renewable energy. The transition from these fuels to renewable energies could extensively and positively impact global warming. The goal is to reduce the use of fossil fuels and, consequently, greenhouse gas emissions, thereby mitigating climate change issues. A non-negligible portion of the energy resources employed by developed countries is currently used for heating and cooling. The industrial sector deserves particular attention because it comprises the largest portion of global energy consumption among the major energy-consuming sectors: industrial, transportation, residential, and commercial. Globally, the industrial sector is responsible for over one-third (37%) of the total energy consumption and a quarter (24%) of the global CO_2 emissions. Solar collectors and thermo-photovoltaic (TPV) may be a gamechanger in the efforts related to industrial transitioning to renewable energy sources. This Ph.D. aims to improve the energy conversion efficiency in High Vacuum Flat Plate Collectors (HVFPCs) and TPV technologies. The HVFPCs are solar collectors capable of supplying mid-temperature output (up to 200 °C), retain all the advantages of a flat plate solar collector (net area is approximately 96% of the gross area), thanks to the vacuum insulation. However, owing to the present state of technology, they remain unsuitable for providing high-temperature heat on a large scale, and therefore, are unable to replace a significant portion of industrial process heat. An optimized solar selective coating and the reduction of the absorber's substrate radiative losses has been proposed to improve the HVFPCs efficiency. A multi-layered structure (Cr-Cr_2O_3 based) appeared to be an interesting solution to achieve high working temperature. The results obtained show an absorber efficiency up to 75% at 300 °C working temperature. Moreover, copper and silver low emissive coating (LEC) seems to best suit the purpose of the absorber's substrate radiative losses reduction. The use of these LEC led to almost doubled the HVFPCs performances. On the other hand, the optimization, development, and realization of selective emitters (SE) has been proposed for the TPV systems. Selective emitters could highly impact on the efficiency of these devices and in reducing heat losses. The proposed SE, is a SiN_x-SiO_2-TiO_2 multilayer structure on tungsten substrate, demonstrating to have a good thermal stability (up to 1000 °C) and the best literature emitter efficiency in 0.63-0.72 eV range. Finally, a novel procedure for the prediction of the service lifetime of solar absorbers for HVFPCs depending on the operating temperatures is proposed to overcome the problems occurred using the current standard (ISO 22975-3:2014). A novel Performance Criterion (PC), that represents the degree of aging of a coating, an appropriate temperature frequency function *f(T)*, that represents how many hours the absorber is at temperature T during one-year operation, were presented. The results obtained following the proposed procedure (decreasing service lifetime with increasing operating temperatures) appear to be more reasonable than those obtained following the standard procedure (increasing service lifetime with increasing operating temperatures), suggesting that the proposed procedure offers a more realistic prediction of service lifetime for absorbers used in HVFPCs.

Nomenclature

Acronyms	
HVFPC	High Vacuum insulated Flat Plate Collectors
SSA	Selective Solar Absorber
TPV	Thermo-photovoltaic
PV	Photovoltaic
STPV	Solar Thermo-photovoltaic
SE	Selective Emitter
E_g	Bandgap energy
ν	Frequency
λ	Wavelength
PC	Performance Criterion
f(t)	Temperature frequency function
c	Velocity of the propagation
ε	dielectric constant
μ	magnetic permeability
c_0	Speed of light in vacuum
n	Refractive index
ρ_λ	Reflection coefficient
α_λ	Absorption coefficient
τ_λ	Transmission coefficient
$B_\lambda(T)$	Spectral irradiance of a blackbody
h	Planck's constant
k	Boltzmann's constant
E_{BB}	Blackbody total emitted power
σ_{SB}	Stefan-Boltzmann constant
$\varepsilon\ (T)$	Thermal emittance
ε(λ)	Surface emissivity
TSC	Transpired solar collector

CPC	Compound Parabolic Concentrator
ETC	Evacuated tubes solar collectors
NEG	Non-Evaporable Getter
α_s	Solar absorptance
η_t	Thermal transfer efficiency
λ_{cut} (T)	Cut-off wavelength
C	concentration factor
η_{abs}	absorber efficiency
w	Weighting factor
T_{amb}	Ambient at temperature
η_{panel}	Panel efficiency
IEA	International Energy Agency
E_T	Activation energy
T_{eff}	Effective constant temperature
PVD	Physical Vapour Deposition
DC	Direct Current diode
RF	Radio Frequency diode
DCMS	DC Magnetron Sputtering
RFMS	RF Magnetron sputtering
DCRMS	DC Reactive Magnetron Sputtering
RFRMS	RF Reactive Magnetron sputtering
MTB	Mini-Test-Box
m_a	Sample mass
c_p	Specific heat
A	Sample Area
P_{in}	Incident Power per unit area
$\bar{\varepsilon}_a(T_a)$	Absorber emittance
$\bar{\varepsilon}_{sub}(T_{sub})$	Equivalent substrate emittance
τ_{glass}	Glass trasmittance

OSA	Optical Spectrum Analyzer
FTIR	Fourier-transform Infrared Spectrometer
ARC	Anti-Reflective Coating
GA	Genetic algorithm
LEC	Low emissivity coating
DB	Diffusion barrier
$P_{out\ ideal}$	PV cell generated electric power
P_{emi}	Emitter emitted power
$\eta_{PV\ cell}$	PV cell power efficiency
J(V)	Current density
q	Elementary charge of a proton
EQE(λ)	External quantum efficiency of the PV cell
m	PV cell ideality factor
T_d	Cell temperature
J_{nr}	Dark current density induced by nonradiative recombination
V	Applied voltage
k	Chemical reaction rate
D_{Arrh}	Arrhenius constant
R	Constant of ideal gas
$PC_{\eta}(T)$	Proposed performance criterion
HTF	Heat transfer fluid
IAM	Incidence angle modifier
O.T.	Operating temperature
t_{LT}	Service lifetime

1. Introduction

Climate change is a real issue that currently engages the entire world: the IPCC (Intergovernmental Panel on Climate Change) predicts a temperature rise of about 1 to 5 °C over the next century, and states that "the range of published evidence indicates that the net damage costs of climate change are likely to be significant and to increase over time". The human activities, the fossil fuels burning, and the industrialization increased the heat-trapping greenhouse gas levels in Earth's atmosphere, causing an increasing of the average global surface temperature and a climate change: scientists have observed that rain has increased by 15% and the sea level has risen by 10.5 cm during the last century [1]. The transition to renewable energy resources could play a key role in the mitigation of the greenhouse gases in the atmosphere. The goal is to reduce the use of fossil fuel and consequently the greenhouse gas emissions, thus mitigating climate change issues [2,3]. In Europe the amount of energy demanded for only heating and cooling is half of the total, while those for electricity and transport are 20% and 31%, respectively [4,5]. The industrial sector deserves particular attention [6] since it comprises the largest portion of global energy consumption among the major energy-consuming sectors [7]. Globally, the industrial sector is responsible for over one third of total energy consumption and a quarter of global CO2 emissions [8]. In particular, the Solar Payback (2017) showed that heat represents three quarters of industrial energy demand worldwide (Fig. 1.1). Of this, only the 9% is supplied by renewable sources, and half of it is required as medium and low-temperatures heat.

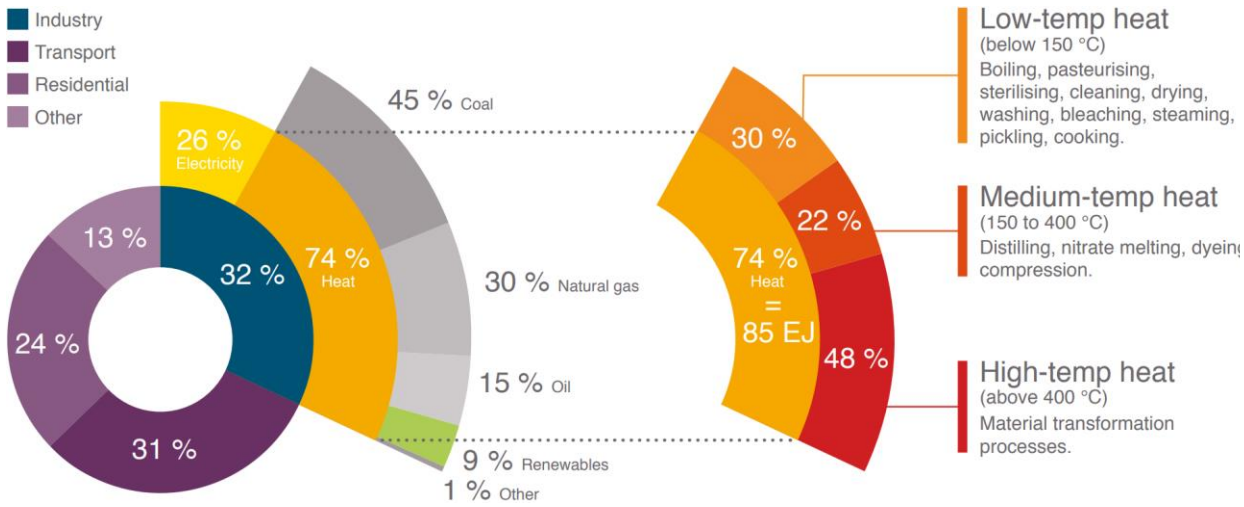

Figure 1.1. Share and breakdown of heat demand in industry: heat represents three quarters of the energy demand of industries world-wide, and half of it is low to medium temperature heat, that could be easily supplied by renewable heat. Source: Solar Payback (2017), based on IEA statistics and calculations by IRENA [9].

According to the National Renewable Energy Laboratory (NREL) [10], "solar energy is a powerful source of energy that can be used to heat, cool, and light homes and businesses", and "more energy from the sun falls on the earth in one hour than is used by everyone in the world in one year".

Furthermore, the environmental impact of solar power is significantly smaller than other power generation methods, in fact the impact is mainly related to the production and supply of the special materials and metals that are required to produce the devices to harness such energy. Solar energy could be easily integrated in industrial plants as a renewable energy source, offering two possibilities: concentrating and non-concentrating solar collection [11]. The technologies most used to produce heat are concentrating solar power (CSP) systems and flat plates. The CSP is mainly used for power plants since its structure is quite complex: it uses mirrors to reflect and concentrate sunlight into a receiver collector, that collects the solar energy. Such systems are suitable for high temperature heat (up to 500 °C), but they can be very expensive and bulky, and their usage is limited by the fact that they can only collect direct solar radiation. Non-concentrating technologies such as flat-plate collectors or evacuated tubes are considerably cheaper and they can be installed almost anywhere, as they use both direct and diffuse solar irradiance, but they do not deliver heat above 100 °C with adequate efficiency. Currently, most projects use non-concentrating technologies since solar heating is economically competitive with fossil fuels at low-medium temperatures. Food and beverage industry, service industry, and textile industry, are examples of industries that need low to medium temperature heat, and it is no coincidence that they represent the main areas in which solar heat has been deployed. Hence, solar collectors could be a gamechanger in industrial transitioning to renewable energy sources, but at the present state of technology they cannot yet provide mid-temperature heat on a large scale, and therefore are unable to replace a significant portion of industrial process heat. A potential solution to overcome the limits of the conventional solar collectors comes from the High Vacuum insulated Flat Plate Collectors (HVFPC), which supply mid-temperature output with high efficiency. In fact, the high vacuum insulation reduces the conductive and convective losses due to the gas, increasing the operating temperature from the old 80-100 °C up to 200 °C, without concentration. Vacuum insulated flat plate collectors concept is known since 1970's [12], but just recently HVFPCs have been introduced on the market by a relatively young company, TVP Solar [13,14], due to the technical challenges involved in the production of a quality product [15]. Unfortunately, the radiative losses due to the hot absorber still survive and rise rapidly with temperature, particularly in the absence of concentration [16]. This limits the use of flat panel devices at temperatures around 150 °C since they experience a fast drop off in the radiative efficiency of the absorber [17]. For this reason, to efficiently use the thermal energy derived from the solar radiation using flat plate solar collectors, an optimized (and low-cost) Selective Solar Absorber (SSA) is required [15]. A selective solar absorber is a surface which can discriminate between solar spectrum and infrared spectrum, being able to capture as much solar light as possible, while emitting as little thermal energy as possible, taking advantage of the difference between the wavelength ranges of the solar spectrum and the thermal radiation emitted by a heated body. Previous works have made progress in improving the optical properties of a solar absorber for mid-high temperature applications: in [18] Ag–Al2O3 nanocermet SSA coatings prepared at different Ag contents on copper, silicon, and glass substrates exhibited $\alpha = 0.93$ in the visible region and $\varepsilon = 0.04 – 0.05$ at 82 °C in the infrared region of the solar spectrum, but the thermal stability test at 400 °C showed degradation in the vacuum annealed coatings due to size decrease of the Ag nanoparticles. Absorbers consisting

of two cermet layers of either W–SiO_2 or Nb–TiO_2, deposited on a molybdenum infrared reflector and coated with an antireflection layer of silicon oxide for mid-temperature operation in collectors for solar thermal electricity plants have been presented in [19]. The optimal values of α and ε for W–SiO2 and Nb–TiO2 were respectively α = 0.91, ε = 0.08 and α = 0.93, ε = 0.09. The properties of a four-layer composite film structure, W/AlSiOx:W(HA)/AlSiOx:W(LA)/AlSiOx, deposited on stainless steel substrate have been investigated in [20] exhibiting α = 0.94 - 0.95 and ε = 0.08 - 0.09 (at 100 °C) and 0.10 – 0.14% (at 400 °C). In [21] a hyperbolic metamaterial made by TiN/SiO2 multilayered structure is studied in order to reduce the emission in the IR range, showing a good selectivity and a high temperature resistance up to 750 °C. However, in these mentioned coatings, the optimization consisted mainly in maximizing the solar absorption without giving attention to the radiative losses. In particular for HVFPCs, the high working temperatures reached without concentration require special attention to be given to the radiative parameters of the selective coating, but the literature still lacks articles about valid SSA coatings for HVFPCs technology and about the evaluation of their thermal stability and service lifetime.

Moreover, also the thermo-photovoltaic (TPV) technologies could play a key role in the transition from fossil fuels to renewable energy. These systems employ a PV module, a heat source (the Sun for STPVs), and a thermal collector [22], and allow thermal radiation emitted by an object heated at temperatures typically above 800 °C to be converted directly into electricity [23]. TPV enable efficient solar energy conversion by shaping the incident spectrum to match the wavelengths useful to the PV cell through the use of intermediate thermal radiation emitter [24]. The ideal thermal emitter is a selective emitter (SE), characterized by a sharp transition from high to low emissivity at the position in the spectrum corresponding to photon energies approximately equal to the bandgap energy (E_g) of the associated PV cell. The choice of the optimal bandgap is determined by the thermal emission spectrum, which in turn is controlled by the emitter temperature and the spectral characteristics of the emitter surface [25]. Several solutions of SE have been already developed in the past [26]. They include bulk emitters, which can be either graybody emitters [27] such as Si, SiC, or metals with [28] and without AR coatings [29]; naturally selective emitters [30], made from rare earth metals (Er, Yb); metamaterials [31]; 1D to 3D [32–34] as well as rod-type [35] or carbon-based nanotube [36] photonic crystals; surface gratings [37], nanostructures [38], as well as metallo-dielectric structures based on refractory materials, such as W, Mo, HfO_2 [39–41]. Although all these solutions have favorable characteristics, they share two main disadvantages: high cost and/or manufacturing complexity, especially when industrialization processes are considered.

To provide solutions to these problems, this thesis focuses on the description and development of new elements useful for improving the performance of solar devices. In fact, this Ph.D. program is born as a part of the FSE-FESR National Operational Program "Ricerca e Innovazione 2014-2020" of the Italian Ministero dell'Istruzione, dell'Università e della Ricerca, and intends to support the promotion and strengthening of fostering collaboration between academic world and private industry in the field of scientific research. For this reason, I have been involved in the

development and optimization of new products in collaboration with the company TVP Solar. The first part of this Ph.D. program has been focused on the increase of the energy conversion efficiency in HVFPCs and thermo-photovoltaic (TPV) technologies.

For the HVFPCs the development of an optimized solar selective coatings and the reduction of the SSA's substrate radiative losses has been proposed. For this purpose, the current state of the art regarding the selective solar absorbers was reviewed to assess which are the solutions that can meet the required criteria. Among the possible designs inspected, multilayer selective absorbers based on chromium and chromium oxide appeared to be the best suited for the purposes of this work. Also, the thermal emittance of some typical metals that can be used as substrates for solar absorbers was studied. Copper and aluminium have the best trade-off between cost of the bulk and optical properties, seems to best suit the purpose of the present study.

For TPV technologies the optimization, development, and realization of selective emitters has been presented. In fact, the development and use of selective emitters could play a key role in increasing the efficiency of these devices and in reducing heat losses: they would act as a "filter" that lets only photons with energy above the bandgap of the photovoltaic cell pass through. The idea is to design easy-to-fabricate selective emitters based on multilayers, as the ones currently available involve mainly metamaterials, metasurfaces, plasmonics structures or nanofabrications, which could be difficult to scale at an industrial level.

One of the main drawbacks in the development of both solar selective coatings and selective emitters is the need for simple and cost-effective solutions, which must be easily reproducible on a large-scale production and used daily in industrial applications. This brought with it many constraints, such as the use of deposition techniques that can be easily applied on an industrial level, the design of structures which avoid complex techniques, the choice of materials inexpensive and easy to handle, etc. In fact, this work represents the first step towards the broader, industrial development of these elements, where all the aforementioned characteristics are fundamental.

The third part of this Ph.D. thesis is concentrated on the elaboration of a novel procedure for the prediction of the service lifetime of solar absorbers for HVFPCs. Currently the standard, named ISO/CD 12592, 2 "Solar Energy – Materials for flat-plate collectors – Qualification test procedures for solar surface durability" [42], is developed for standard collector working in air at low temperature, and it cannot be used also for HVPCs. For this reason, a review of the current standard was done. The Performance Criterion (PC), that represents the degree of aging of a coating, the temperature frequency function *f(T)*, that represents how many hours the absorber is at temperature T during one-year operation, and the procedure flow were revised and adapted to be suitable to evaluate the service lifetime of solar absorbers for HVFPCs.

The thesis work presented has been carried out in collaboration with: University of Naples "Federico II" in Naples (Italy); Istituto di Scienze Applicate e Sistemi Intelligenti "Eduardo Caianiello" (ISASI - CNR) of Naples (Italy); TVP Solar in Avellino (Italy); Purdue University, in West Lafayette (Indiana, USA).

2. Solar thermal collectors and working principles

2.1 Basic principles of optics

An electromagnetic wave is a transverse wave consisting of an electric field vector, and a magnetic field vector, function of position and time, mutually perpendicular and perpendicular to the direction of propagation. Electromagnetic waves are characterized by a parameter, called wavelength λ which represents the distance covered by the radiation in a period, or the frequency ν, which represents the number of cycles in the time unit. Velocity of the propagation c can be expressed as:

$$c = \lambda \nu \tag{2.1}$$

The electromagnetic spectrum represents the range of frequencies of electromagnetic radiation and their respective wavelengths and photon energies. It is illustrated in Fig. 2.1, where it is evident the partition in separate bands: radio waves, microwaves, infrared, visible light, ultraviolet, X-rays, and gamma rays at the high-frequency (short wavelength) end.

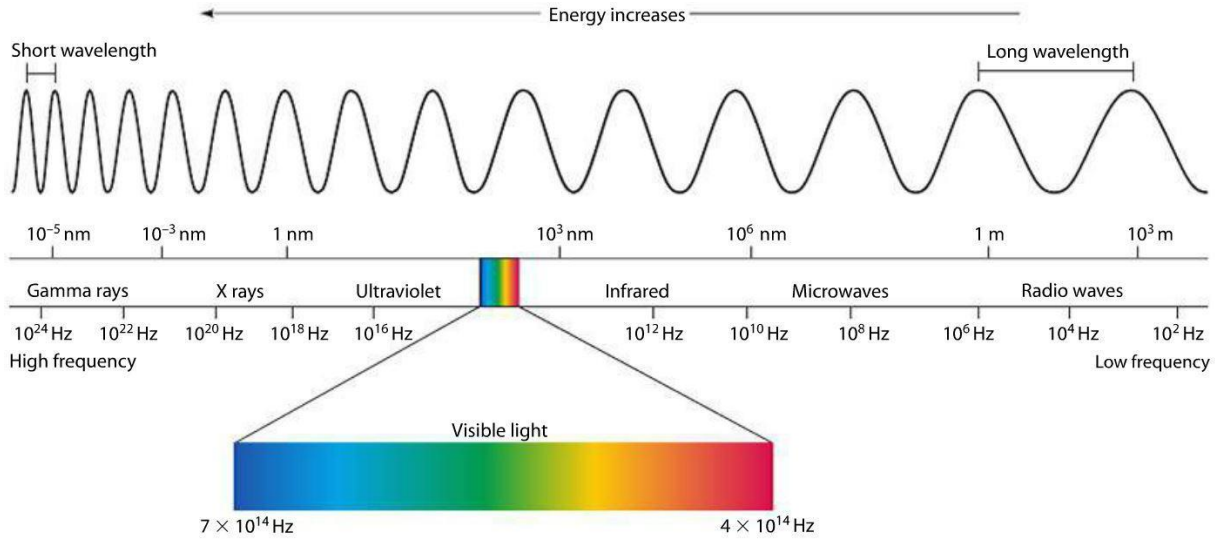

Figure 2.1. The electromagnetic spectrum showing the boundaries between different regions. The coloured inset shows the visible spectrum [43].

The speed defined in Eq. 2.1 can be also related to the dielectric constant (or permittivity) ε and the magnetic permeability μ of the medium in which the wave propagates, as predicted by Maxwell's equations:

$$c = \frac{1}{\sqrt{\varepsilon \mu}} \tag{2.2}$$

Note that ε depends on the properties of the medium considered through the relative permittivity ε_r: $\varepsilon = \varepsilon_r \cdot \varepsilon_0$. The same applies to the magnetic permeability: $\mu = \mu_r \cdot \mu_0$. When light propagates in vacuum it assumes its maximum value, in fact $\varepsilon_r = \mu_r = 1$ and:

$$c_0 = \frac{1}{\sqrt{\varepsilon_0 \mu_0}} \tag{2.3}$$

Where $c_0 = 2.9979 \cdot 10^8$ m/s is the speed of light in vacuum.

Being ε and μ the dielectric constant and magnetic permeability of the medium. We can define:

$$n = \frac{c_0}{c} = \frac{\lambda_0}{\lambda} = \sqrt{\frac{\mu\,\varepsilon}{\mu_0\,\varepsilon_0}} = \sqrt{\varepsilon_r\,\mu_r} \tag{2.4}$$

Being n the refractive index and ε_r and μ_r the relative dielectric and magnetic constant of the medium. The refractive index depends on the frequency of the radiation. Equation 2.4 shows the physical phenomenon that the speed of light becomes slower in a medium with high n. Frequency ν is unaltered when passing from a medium with refractive index n_1 to another with refractive index n_2, while velocity of propagation varies:

$$\frac{c_1}{c_2} = \frac{n_2}{n_1} \tag{2.5}$$

And so does the wavelength:

$$\frac{\lambda_1}{\lambda_2} = \frac{n_1}{n_2} \tag{2.6}$$

While the electromagnetic radiation propagates through a medium and hits the surface of an object, the following phenomena can affect the incident light beam [44], as schematized in Fig. 2.2:

• Reflection: reduction of the light velocity and bending of the rays;

• Absorption: attenuation of the beam as it progresses;

• Transmission: non-absorbed light passes through the medium. If the light goes through the object and bends at an angle, we talk about refraction.

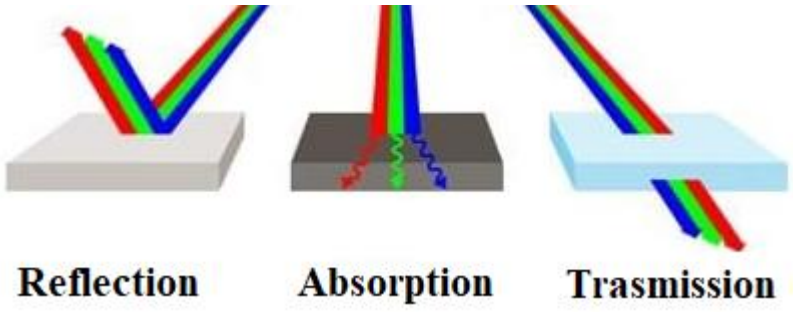

Figure 2.2. Reflection, absorption, and transmission of a light beam incident on a medium.

When the electromagnetic radiation (defined as irradiation, G) hits the surface of a body, part of the radiation is reflected, while the remaining part enters the body and propagates through. If the body is an absorbing medium the light that enters the body will be absorbed and converted into

energy. On the contrary, if the body is transparent, or its thickness is lower than the thickness that is needed to absorb all the radiation, the light that enters the body is transmitted reaching the back surface where it can be reflected again and/or transmitted to the other side. These phenomena can be described by the coefficient of reflection (ρ_λ), absorption (α_λ), and transmission (τ_λ), which corresponds to the reflected, absorbed, and transmitted fraction of the total incoming irradiation, G. Note that the defined coefficients are wavelength-dependent; to indicate the total values (α, ρ, τ) we need to calculate their spectral average. Therefore, recalling the conservation of energy, we can state that the sum of the fraction of light transmitted, absorbed, and reflected must return the intensity of the incident beam, at each wavelength λ. In other words:

$$\alpha G + \rho G + \tau G = G \tag{2.7}$$

The attenuation coefficient a (also called absorption coefficient) is defined as the amount of energy absorbed per unit length and it quantifies the absorption of light by a medium. The attenuation coefficient a must not be confused with the total absorption coefficient α, being α a dimensionless parameter which quantifies the fraction of the incoming radiation G absorbed by the medium. If z is the direction of propagation and the intensity (power per unit area) at position z is I(z), the decrease of the intensity in dz is:

$$dI = -adz \cdot I(z) \tag{2.8}$$

That integrated results in the Beer's law:

$$I(z) = I_0 \, e^{-az} \tag{2.9}$$

Being I_0 the intensity at $z = 0$.

Absorption and the refraction can be incorporated into a single quantity named complex refractive index, $\tilde{n}$. The complex refractive index allows to calculate the reflectivity R, and hence the transmissivity T. $\tilde{n}$ is usually defined as:

$$\tilde{n} = n + ik \tag{2.10}$$

The real part of $\tilde{n}$ (n) is the refractive index as defined in equation 2.4. The imaginary part (k) is called extinction coefficient. The extinction coefficient is directly related to the attenuation coefficient a:

$$a = \frac{4\pi k}{\lambda} \tag{2.11}$$

Fresnel equations describe the behaviour of the electromagnetic radiation when it crosses an interface dividing two materials with different refractive index [45]. These equations can be used to evaluate reflection, absorption and transmission coefficients depending on wavelength, angle of incidence and polarization of the incoming light radiation.

It is possible to relate the refractive index of a medium to its dielectric constant, ε_r:

$$n = \sqrt{\varepsilon_r} \tag{2.12}$$

Being $\varepsilon_r = \varepsilon_1 + i\varepsilon_2$, results:

$$\varepsilon_1 = n^2 - k^2 \tag{2.13}$$

$$\varepsilon_2 = 2nk \tag{2.14}$$

2.2 Thermal radiation and blackbody emission

There exist three different processes of thermal energy (heat) transfer, also known as modes [46]. The first mode is named conduction and refers to the heat transfer that occur across the medium; the second mode is the convection, which represents the heat transfer that occur between a surface and a moving fluid at different temperatures; the third and last mode is the thermal radiation: all surfaces at a certain temperature emit energy in form of electromagnetic waves. While conduction and convection modes require the presence of a material medium to allow the energy transfer, radiation does not. In fact, radiation transfer occurs most efficiently in vacuum.

At high temperature the thermal radiation represents an important mechanism of thermal loss, that significantly affects the performances of the collectors. To properly define the thermal radiation of a body, blackbody radiation should be introduced first. Blackbody radiation is defined as the thermal radiation emitted by an idealized physical body, which is called a blackbody. A blackbody in thermal equilibrium is both a perfect absorber and a perfect emitter, in the sense that it both absorbs end emits the same or more energy than any other object at the same temperature, for all the wavelengths. The spectral irradiance $B_\lambda(T)$ (Wm^{-3}) of a blackbody is described by Plank's radiation law [47], in SI units:

$$B_\lambda(T) = \frac{2\pi h c^2}{\lambda^5 \left(e^{\left(\frac{h\,c}{k\,\lambda\,T}\right)} - 1 \right)} \tag{2.15}$$

In Eq. 2.15 h is the Planck's constant, $h = 6.62 \cdot 10^{-34}$ J ·s, c the speed of light (m/s), λ the wavelength (m), $k = 1.38 \cdot 10^{-23}$ J/K is the Boltzmann's constant, and T the temperature in Kelvin degrees. Nevertheless, the conventional unit used for blackbody spectral irradiance is in $Wm^{-2}\mu m^{-1}$.

The total emitted power E_{BB}(Wm^{-2}) is obtained by integrating the blackbody spectral irradiance over all the wavelengths:

$$E_{BB} = \sigma_{SB}\, T^4 \tag{2.16}$$

Being σ_{SB} ($Wm^{-2}K^{-4}$) the Stefan-Boltzmann constant.

As temperature increases, the maximum intensity of black body radiation is shifted to shorter wavelengths, according to the Wien's displacement law, $\lambda_{max} = b/T$, b = 2898 μm · K [48]. Wien's law indicates an inverse relationship between wavelength and temperature: higher the temperature, shorter the wavelength at which the peak is placed. Figure 2.3 shows how, for increasing

temperature, the peak of blackbody radiation has higher intensity and shift towards shorter wavelengths, according to Wien's law.

The thermal radiation spontaneously emitted by an object is called thermal emittance and it can be defined as the ratio between the power emitted by the object itself and the power emitted by a blackbody at the same temperature (eq. 2.17). For most of the solar thermal applications the thermal radiation spectrum is generally limited in the infrared range between approximately 1 μm and 50 μm.

$$\varepsilon\,(T) = \frac{\int_0^\infty \varepsilon\,(\lambda)\, B_\lambda\,(T)}{E_{BB}(T)} \tag{2.17}$$

Where ε(λ) is the surface emissivity, $0 \leq \varepsilon \leq 1$.

2.3 The solar spectrum

The Sun's surface behaves like a blackbody at a temperature of about 5800 K, with some near-zero intensity regions due to the light absorption in the atmosphere. As the solar radiation passes through the atmosphere, part of it is absorbed, reflected, or scattered. Direct radiation is defined as the radiation that reaches Earth's surface without being scattered, travelling on a straight line from the sun, down to the surface of the earth, whereas the radiation having experienced scattering processes in the atmosphere is defined as diffuse radiation. The total radiation that reaches Earth's surface is given by the sum of the direct and diffuse irradiation. The orientation of a surface is a fundamental parameter when dealing with direct irradiance, on the contrary the maximum amount of diffuse radiation can be gathered when the surface is laying down horizontally, since diffuse radiation is generally equally distributed throughout the sky. Because the solar spectrum varies according to the location and time of the year, Fig. 2.3 shows the two standard solar irradiance at the Earth's surface, as defined by the American Society for Testing and Materials (ASTM) G173-03, for an Air Mass (AM) of 1.5 [49]. The AM1.5 Global spectrum is intended for flat plate collectors and has an integrated power of 1000 W/m^2. The AM1.5 Direct plus circumsolar spectrum includes the direct beam from the sun plus the circumsolar component. It has an integrated power density of 900 W/m^2 and it is intended for solar concentrator. It is worth to notice that terrestrial solar radiation is limited to the range of wavelength between 0.3 μm and approximately 2.5 μm, i.e. ultraviolet, visible and near-infrared ranges (UV/VIS/NIR).

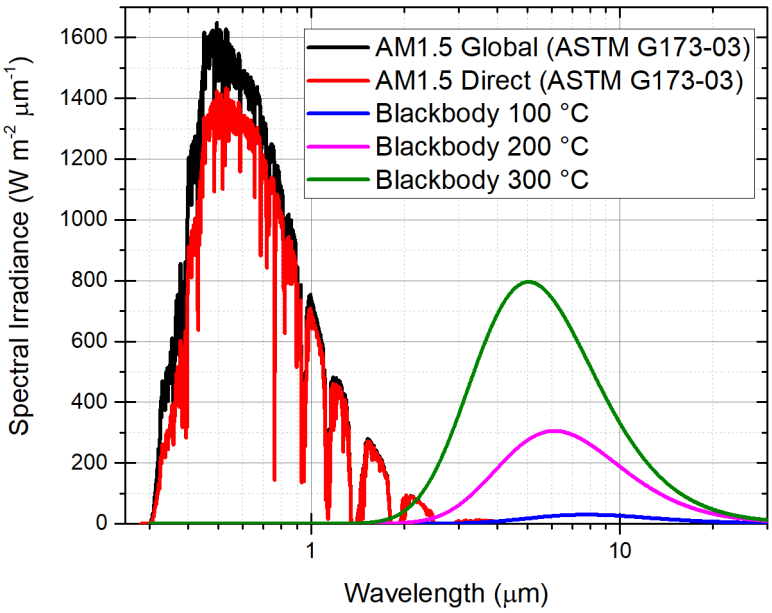

Figure 2.3. Standard solar spectra for terrestrial use and black body radiation spectra.

2.4 Solar thermal collectors

Solar thermal collectors are devices used to collect the solar radiation and convert it into thermal energy through a transport medium. Solar thermal collectors can be generally outlined as shown in Figure 2.4. Solar thermal devices are mainly divided into two categories: concentrated and unconcentrated Solar Thermal devices [11]. Concentrators mainly collect direct solar radiation and a small portion of the diffuse light that fall within the acceptance angle. They enable high temperature outputs, but the need of a tracking infrastructure can add to the expense and complication of the devices themselves. Unconcentrated solar thermal collectors on the other hand, can collect both diffuse and direct irradiance, and they are considerably cheaper, but their use in industrial process heat suppling is limited by the low temperatures output. Losses in a solar collector are to be identified with:

- Reflection losses due to both the glass cover and the solar absorber surface. They can be reduced by using anti-reflective glass and optimized coatings.

- Conduction losses, due to the necessary connections between the high temperature components and the collector frame. They can be reduced by using the right insulating materials and a careful design.

- Losses due to the internal gases: at ambient pressure the main mechanism is represented by convection losses, at moderate vacuum pressures gas convection becomes negligible while gas conduction losses are still present. For high vacuum pressures ($<10^{-2}$ Pa) both convection and conduction losses due to the internal gases are negligible.

- Radiative losses due to the thermal radiation coming from high temperature components (mainly the solar absorber). They can be reduced by acting on the selective coating and the substrate properties.

The thermal collectors are usually classified in terms of the working temperature as:

• low-temperature technologies, involving working temperatures below 70 °C requested by applications like space or water heating, etc.;

• medium-temperature technologies, with temperatures between 70 °C and 200 °C of interest for solar cooling, solar distillation, etc.;

• high-temperature technologies, with temperatures above 200 °C useful in solar thermal power generation systems.

The main types of solar collector devices used for solar water heating systems are presented in this section: unglazed collectors, flat plate collectors, evacuated tubes, parabolic troughs.

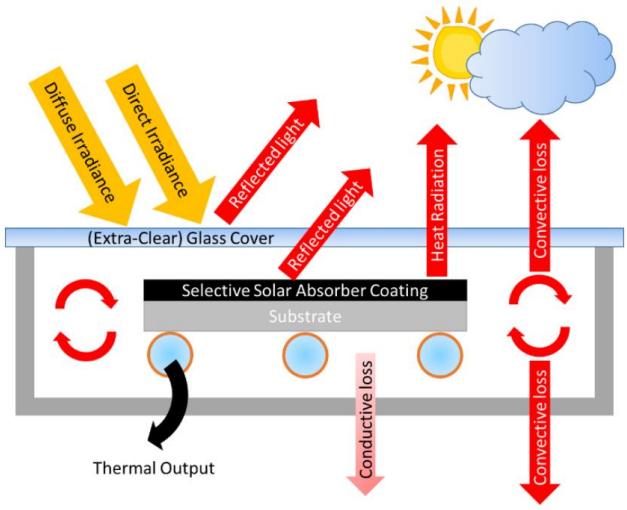

Figure 2.4. Solar collector conceptual drawing

2.4.1 Unglazed collectors

Typically, unglazed collectors (fig. 2.5) consist of a dark metallic or black plastic absorber plate without a cover. The absence of glazing allows them to absorb a larger portion of the solar energy, but because they are not insulated a large portion of the heat absorbed is lost, particularly when it is windy. In fact, they are mostly involved in low temperature applications, below 30 ◦C, such as for heating swimming pools. The most common type of unglazed collector on the market is the transpired solar collector (TSC), widely used in Canada and USA. They use solar energy to heat the absorber surface (usually steel or aluminium), which transmits thermal energy to the ambient air. The contact surface between the absorber and air is increased by drawing air through the multiple small perforations into the cavity between the skin and building facade.

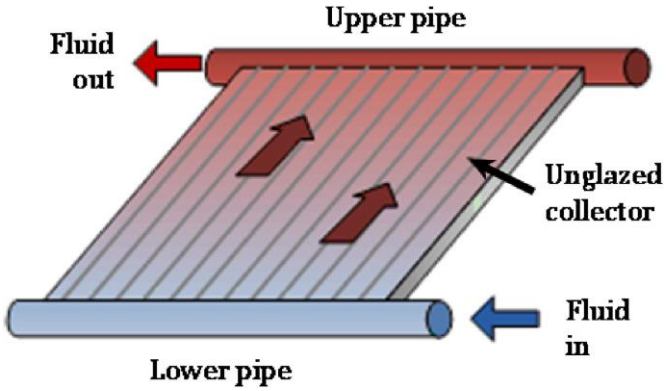

Figure 2.5. Schematic representation of an unglazed collector [50].

2.4.2 Parabolic trough collectors

Parabolic trough collectors consist of concave parabolic shaped high reflecting mirrors that concentrate solar light onto a receiver pipe located in the focus of the parabola as shown in Fig. 2.6. A single-axis tracking mechanism is used to angle both solar collectors and heat receivers toward the sun, ensuring that all the solar radiations fall parallel to mirrors axis. The heat collection element (HTE) consists of a solar absorber pipe insulated by an evacuated glass tube. Because of the high temperature outputs of the concentrating technologies, the solar absorber is usually made of a stainless-steel pipe equipped with a selective solar coating. The operating temperature of the system is in the range of 200-500 °C and the geometric concentration ratio of the parabolic-trough system is in the range of 30–100 [51]. The heat transfer fluid used is generally synthetic oil, but molten salts can be used when there is the need to reach high temperatures [52]. Large scale power plants need a storage system to overcome the inconsistency of the solar energy source. Although these collectors guarantee high temperature outputs as discussed, with relatively high efficiency, their use is limited by the fact that they only collect direct-beam sunlight requiring high cleaning standards for the mirrors and tracking systems to efficiently harness solar energy in day-light hours, resulting in high maintenance costs and installation issues.

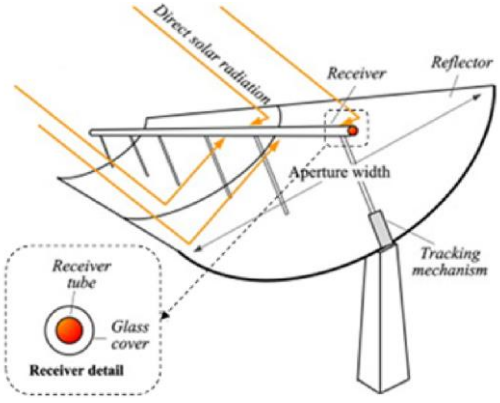

Figure 2.6. Schematic representation of a Parabolic trough collector. Adapted from [50].

2.4.3 Compound Parabolic Concentrator

Another trough-type technology that concentrates solar energy onto a tube receiver is the Compound Parabolic Concentrator (CPC) (fig. 2.7). Two symmetric parabolic segments with different focal lengths are combined to enable the collection of any solar radiation entering the collector aperture within an acceptance angle onto the tube receiver by means of multiple internal reflections. This allows CPCs to operate without continuous tracking. They have been found to provide the best optics for systems with a low solar radiation concentration and can be designed with low concentrating ratios (<5). They are well-suited for medium-to high temperature applications [53].

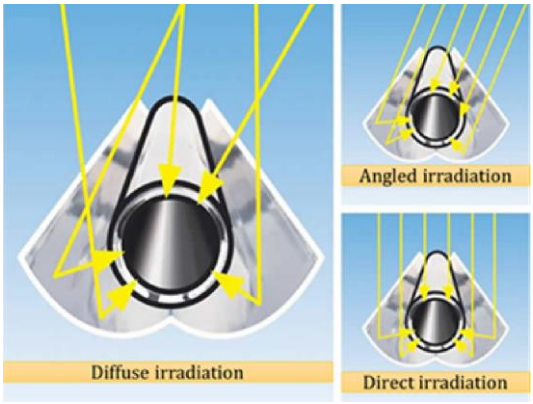

Figure 2.7. Schematic representation of a Compound Parabolic Concentrator. Adapted from [50].

2.4.4 Flat Plate Collectors

Conventional flat-plate collectors (fig. 2.8) can collect both the direct and the diffuse component of radiation. Their basic structure is relatively simple: a metallic chamber is equipped with a transparent glass cover on the top that let the solar radiation hit a solar absorber which, thanks to its adequate characteristics (on which we will focus on later), absorb the solar radiation. A transport medium, which is often a fluid like oil or water, flows into the conducting pipes. Both for the better price-to-performance ratio and for the easier mounting options (on the roof, standalone, etc.), flat systems are spreading a lot. Unfortunately, their demand is currently limited only to the more common low temperature applications (e.g. in residential sites, to heat or cool water and environments). In fact, their temperature output is too low ($\simeq$ 150 °C) to meet the industrial requirements of medium and high-temperature heat (above 250 °C). This is because there are various sources of loss in these devices: reflection losses, due to the glass cover and the absorber; conduction and convection losses, caused by the various connection elements within the panel and by the gas trapped into the chamber; radiative losses, mainly generated from the absorber, but a small part comes from all the components at high temperature.

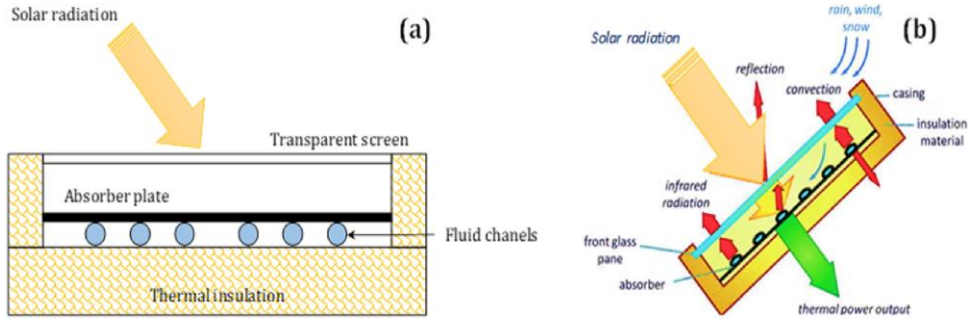

Figure 2.8. Schematic representation of a conventional flat-plate collector: (a) basic schema; (b) heat transfer phenomena. Adapted from [50].

As flat-plate collectors have the potential of reaching performance higher than that of compact parabolic concentrating collectors [54], it is essential to improve their performance and work to extend the applicability of these systems. Fortunately, all the above causes of loss can be reduced with a proper design of the collector and with the use of new or improved elements.

The thermal losses from the absorber to the ambient significantly affect the flat plate collector efficiency. A simple way to reduce the losses is to partially evacuate the panel. Figure 2.8 shows how partial evacuation, down to 10^3 Pa (regime of gas heat conduction independent from pressure) allows to get rid of conductive losses. To further reduce the thermal losses a gas more appropriate than air can be used to reduce the thermal conductivity, introducing a sealed and gas-filled flat collector. Gas like Argon, Xenon or Krypton have been studied to serve to this purpose (see Figure 2.9) [18]. The typical employed pressures are in the range of 10^2 - 10^4 Pa. This sealed design guarantees to the collector a longer service lifetime because the solar selective coating is protected against environmental agents.

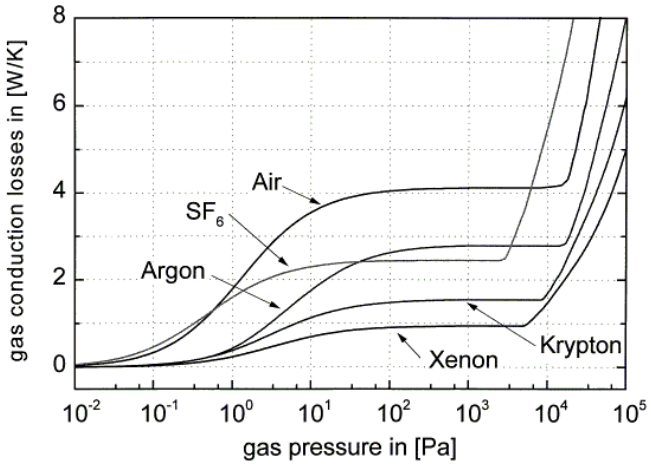

Figure 2.9. Heat losses by gas heat conduction from the hot absorber to the casing in a flat-plate collector in dependency of the gas pressure in the collector casing for different filling gases. The typical operation pressure ranges in the plateau between 100 and 10^4 Pa (adapted from [55]*).*

2.4.5 Evacuated tubes collectors

A way to enhance the performances of a solar collector is to evacuate the space between the absorber and the external box, taking advantage of the vacuum as an efficient isolation mechanism to eliminate the convection losses. We already discussed how partial evacuation, down to 10^3 Pa (regime of gas heat conduction independent from pressure) allows to get rid of conductive losses. Further reducing the gas pressure down to about 10^{-2} Pa allows to eliminate the gas conduction losses too, as shown in Figure 2.10. Evacuated tubes solar collectors (ETC) use a series of sealed glass tubes equipped with an inner solar absorber (Figure 2.10). The absorber can be either a metallic fin with a selective coating and attached to a metal (or glass) pipe that circulates the heat transfer fluid, or the pipe itself can be 'painted' with a solar coating. An anti-reflective coating can be deposited on the inner and outer surfaces of the glass tubes to improve transparency. Vacuum help preserving both the selective and the inner anti-reflective coating. Glass-metal evacuated tubes need a high vacuum tight seal at one or both sides of the evacuated tube. The glass-to-metal seal connects the brittle glass material to a metal with usually different thermal expansion coefficients.

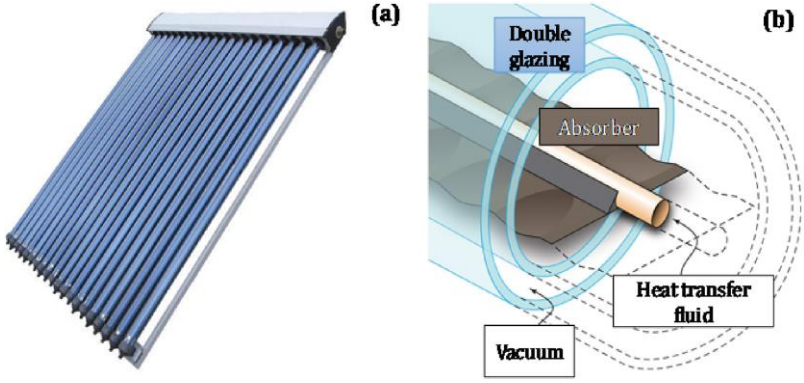

Figure 2.10. (a) Evacuated tube collectors; (b) representation of a concentric tube. Adapted from [50].

Hence, temperature differences lead to thermal stresses in the seal itself putting the vacuum tightness at risk [56]. Glass-glass evacuated tubes are a way to solve glass-metal seal issues because glass-to glass seal is very reliable. They are made with two borosilicate glass tubes fused together at one or both ends, vacuum is made between the two concentric tubes and the absorber is placed in the inner tube. The drawback of this configuration is that two glass layers reduce the transparency leading to higher optical losses. To avoid this issue the selective coating could be deposited directly on the inner glass tube, but the poor glass heat conduction would affect the thermal exchange. Vacuum pressure used are of the order of 10^{-2} Pa [57]. A getter pump (metallic compounds designed to absorb the gas molecules, such as hydrogen, water, and other gases, that permeate into the vacuum envelope over time) is commonly evaporated inside the high vacuum tubes to keep a good vacuum pressure over the time. Life of the vacuum lies between 5 to 15 years depending on the type of collector. Evacuated tube collectors can achieve high temperatures (above 200 °C) with high efficiencies, taking advantage of the high vacuum insulation [58].

However evacuated tube collectors have a discontinuous absorbance area and cover only a fraction of their occupied area (gross area), because of the space between the glass tubes and the vacuum gap between each tube and its absorber inside. ISO 9806 standard states that the efficiency of solar thermal collectors should be measured in terms of gross area, and this might favour flat plates type collectors.

2.4.6 High Vacuum Flat Plate Collectors

High Vacuum Flat Plate Collectors (HVFPC) combine the advantages of Evacuated tubes and flat plate collectors. HVFPCs are evacuated down to 10^{-2} Pa or lower pressure, allowing to eliminate both convection losses and gas conduction losses. For this reason, HVFPC should not be confused with partially evacuated collectors. The first collector making use of high vacuum insulation was developed at CERN [59], while TVP SOLAR SA was the first company to commercialise Solar Keymark certified collectors in 2012 [60]. HVFPC are more complicated to realize than ETC, as they need to support the external structure against the atmospheric pressure and a glass-metal seal to join the glass cover and the metallic part of the vacuum envelope. To support the glass against atmospheric pressure an array of pins is used, so the absorber plate is provided with holes to properly accommodate the pin structure (also considering thermal expansion issues) (Figure 2.11, [61]). To prevent outgassing that will inevitably raise the internal pressure affecting the performances, only materials with low vapour pressure should be used for the collectors. To efficiently keep high vacuum insulation HVFPCs make use of Non-Evaporable Getter pumps (NEG), which can be regenerated in situ by exposure to solar light. HVFPC technology offers the highest efficiency among the other non-concentrating technologies [15], but their practical realization is a technical challenge.

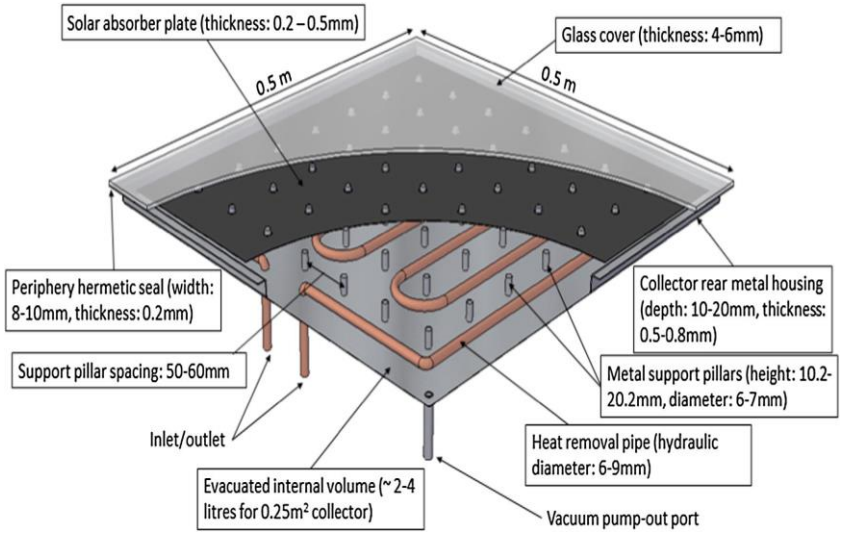

Figure 2.11. Conceptual design of a 0.25 m^2 High Vacuum Flat Plate solar Collector (Henshall et al. [61]*).*

2.4.6.1 The HVFPC by TVP Solar

The solar thermal collectors produced by TVP Solar is showed in Fig. 2.12: it consists of two return and supply copper pipes, a support glass, and an absorber coated on a copper substrate and enclosed between a highly transparent glass cover and a stainless-steel vessel. The glass support structure has pins capable to sustain the pressure exerted on the external glass, to realize a more solid structure, while the font glass is welded to the rest of the system by an adhesive paste. Therefore, the absorber has holes that must include the pins. To guarantee the proper vacuum seal, the panel is tested by using a leaks detector and helium as a tracer gas. Finally, the system is baked in a proper oven at high temperature. The working principle of the HVFPC could therefore be summarized as follows: as the absorber gets hotter, heat is transferred through the copper pipes to the transfer fluid, which raises its temperature. Of course, part of the heat emitted by the absorber is also transferred to the surrounding space: to minimize losses from the bottom and lateral sides, the collector has been insulated with aluminium. Figure 2.12 shows the efficiency of MT-Power high vacuum collector produced by TVP Solar. Such collectors are optimized to operate within the range 80 - 180 °C. They are Solar Keymark certified by ITW Stuttgart (see certificate N. 011-7S1890 F). It is clear from the graph in Figure 2.12 how these collectors can achieve an efficiency as high as 45% at $T_m - T_a$ = 160 °C (being T_m and T_a the absorber and ambient temperature respectively), while stagnation temperature is higher than 300 °C. Such performances are achieved without solar concentration, featuring zero maintenance, and avoiding the added extra costs deriving from the need of a complicated tracking system as well as cleaning of the reflectors, resulting in reduced system costs [13,14].

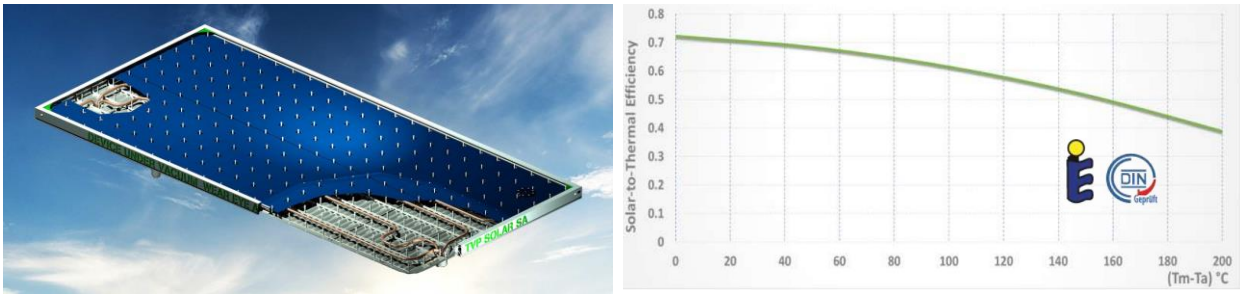

Figure 2.12. Left) TVP Solar High Vacuum Evacuated Flat Plate Collector. Right) Efficiency of MT-Power v 4.0 high vacuum insulated collector by TVP Solar (adapted from [14]*).*

The system is highly reliable, 100% recyclable and designed as ideal thermal energy source for large-scale applications between 80 °C and 180 °C such as: air conditioning, desalination, and process heat. In fact, the high vacuum insulation, and the careful choice of the materials to use in the fabrication allow those systems to achieve a high efficiency up to operating temperature of 200 °C, as shown in Fig. 2.13: at 150 °C, the panel efficiency is of 50% and it reaches the stagnation point with 0% efficiency at about 300 °C. In particular, to avoid degassing (that in turn raise the internal pressure), low vapor pressure materials are used. Nevertheless, Fig. 2.13 shows that, even though vacuum encapsulation brings many advantages, both the optical and the radiative contributions to the global losses remain. The latter increases with the fourth power of the

temperature (as stated by the Stephan-Boltzmann law in eq. 2.16), limiting the efficiency of the devices. Therefore, in the next section we will discuss various strategies useful to overcome/reduce this problem.

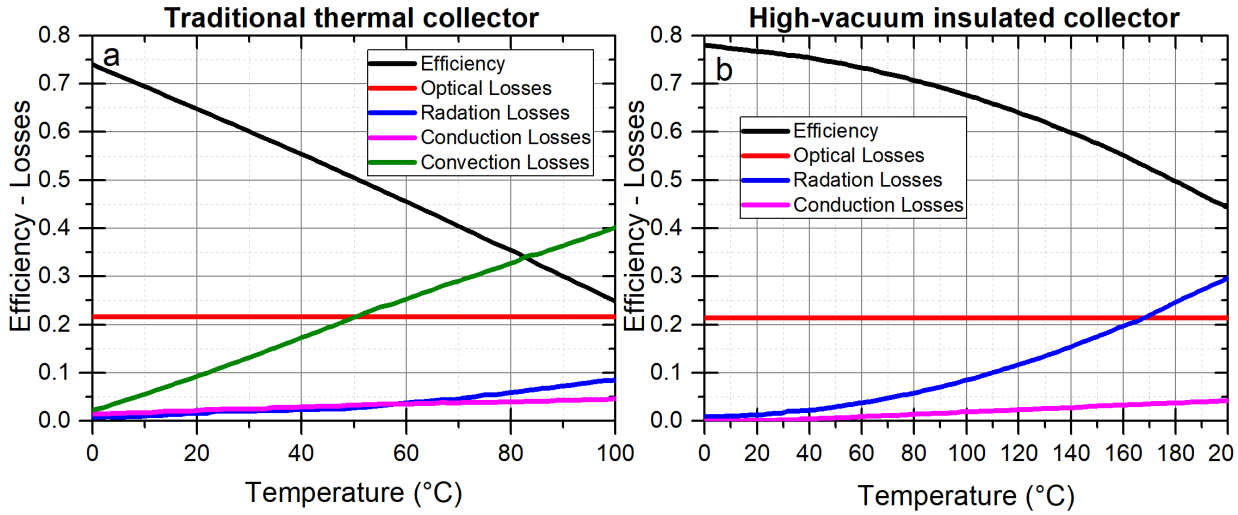

Figure 2.13. Effects of high vacuum insulation on the performance of a flat plate solar collector. a) Efficiency and losses in a standard flat plate solar collector without vacuum insulation. b) Efficiency and losses of a high vacuum insulated flat plate solar collector. In a high vacuum flat plate solar collector, the radiative losses become the main loss mechanism.

3. Selective Solar Absorber

Flat plate solar thermal collectors, independently from the presence of vacuum insulation, are equipped with a solar absorber. This component converts the solar light into heat and transfers it toward the pipes containing the working fluid through thermal conduction. High thermal conductivity of the absorber is mandatory to reduce the temperature gradient between the absorber and the fluid, which is cause of loss on the overall conversion performance. For this reason, absorbers designed for flat collectors are always made of copper or aluminium, since a thickness as small as few tenths of millimetre is enough to guarantee the proper heat transfer [62]. Being metals notoriously reflective, the surface exposed to the glass, dedicated to solar light absorption, is commonly coated by absorbing materials reaching fractions of total absorbed solar light above 90% [63]. The common temperature range of application for this kind of absorbers is below 100 °C, as they are used in flat collectors for domestic purposes, like water heating. Their maximum reachable temperature is limited by convection of air between the absorber-glass space and by conduction through the insulation material placed below the absorber to fill the gap with the vessel bottom. Because of the limited operating temperature, the radiative emission in the Infra-Red wavelengths of the absorber is just a secondary contribution to losses which are mainly driven by conductive and convective mechanisms. Nonetheless, the absorber design is aimed at maximizing the solar light absorptance and simultaneously limiting the emitted thermal radiation to negligible levels [64].

3.1 Selectivity

Selectivity is defined as the property of a solar absorber to differentiate between the wavelengths of the solar spectrum radiation and the infrared wavelengths that are characteristic of the blackbody radiation temperature. Since solar radiation spectrum is limited to relatively short wavelengths UV/VIS/NIR, whereas a realistic terrestrial application is in the range of infrared wavelengths, an effective Selective Solar Absorber (SSA) should be able to discriminate between solar spectrum and infrared spectrum, being able to capture as much solar light as possible, while emitting as little thermal energy as possible. The selectivity of an absorber can be characterized introducing the solar absorptance and the thermal emittance. The spectral emittance ε_λ could be defined as the ratio between the radiation energy emitted by the object itself $E_\lambda\,(T, Surface)$ that depends by the temperature T and the surface, and the energy emitted by a blackbody at the same temperature $B_\lambda\,(T)$ dependent by the temperature T:

$$\varepsilon_\lambda(T, Suface) = \frac{E_\lambda(T,Surface)}{B_\lambda\,(T)} \tag{3.1}$$

The total emittance $\varepsilon\,(T, Surface)$ or thermal emittance is obtained by integrating over all the wavelengths:

$$\varepsilon\,(T, Surface) = \frac{\int_0^\infty \varepsilon_\lambda(T,Suface)\,B_\lambda\,(T)\,d\lambda}{\int_0^\infty B_\lambda\,(T)\,d\lambda} \tag{3.2}$$

When radiative energy interacts with a given surface, part of it could be reflected, while another fraction could be absorbed and the remaining fraction could be transmitted, defining the spectral absorption, reflection, and transmission coefficients, α_λ, ρ_λ, and τ_λ respectively. The sum of the three coefficients is 1 (see Equation 2.7):

$$\alpha_\lambda + \rho_\lambda + \tau_\lambda = 1 \tag{3.3}$$

For opaque surfaces transmittance is equal to 0, resulting in the following relationship:

$$\alpha_\lambda = 1 - \rho_\lambda \tag{3.4}$$

According to Kirchhoff's law, for a given surface in thermal equilibrium, absorptivity and emissivity are equal:

$$\alpha_\lambda\,(T, Suface) = \varepsilon_\lambda\,(T, Suface) \tag{3.5}$$

Where α_λ and ε_λ are defined as the spectral absorptivity and spectral emissivity respectively, and they should both be considered as dependent on the temperature and the surface type. Even if, according to Kirchhoff's law, α_λ and ε_λ are equal at the equilibrium, α_λ is conventionally intended for the solar spectrum range while ε_λ is conventionally intended for infrared blackbody emission range. This formulation let us define the spectral absorptivity and spectral emissivity as dependent by the reflectivity:

$$\alpha_\lambda\,(T, Suface) = \varepsilon_\lambda\,(T, Suface) = 1 - \rho_\lambda\,(T, Suface) \tag{3.6}$$

This allows us to write spectrally averaged solar absorptance and the thermal emittance as follows (for convenience dependence from the surface will be omitted from now on):

$$\alpha_s(T) = \frac{\int_0^\infty (1-\rho_\lambda)\, S(\lambda)\, d\lambda}{\int_0^\infty S(\lambda)\, d\lambda} \tag{3.7}$$

$$\varepsilon\,(T) = \frac{\int_0^\infty (1-\rho_\lambda)\, B_\lambda(\mathrm{T})\, d\lambda}{\int_0^\infty B_\lambda(\mathrm{T})\, d\lambda} \tag{3.8}$$

Being $S(\lambda)$ (Wm^{-3}) the spectral solar irradiance.

Because of α_λ negligible dependence on the temperature, the spectrally averaged absorptivity will be simply identified with the nomenclature α_S [65].

Thermal transfer efficiency η_t is defined as the solar irradiation converted into thermal energy at a certain temperature T and solar concentration C:

$$\eta_t = \alpha_s - \frac{\varepsilon\,(T)\,\sigma_{SB} T^4}{C \cdot G_{Sun}} \tag{3.9}$$

Being G_{Sun} (Wm^{-2}) the integrated solar spectrum. Thermal transfer efficiency η_t allows to derive important energetic considerations as regarding the selective solar absorbers.

3.2 Ideal Selective Absorbers

The ideal selective solar absorber is a reference point when dealing with selective absorbers. Ideally, its behaviour would be well described by the dash-dotted lines in Fig. 3.1), exhibiting an absorptivity curve described by:

$$\alpha_\lambda = \begin{cases} 1, & if \ \lambda < \lambda_{cut}(T) \\ 0, & if \ \lambda > \lambda_{cut}(T) \end{cases} \tag{3.10}$$

where λ_{cut} (T) is the cut-off wavelength, defined as the transition wavelength from high-to-low absorptivity that maximizes the efficiency at a certain working temperature. Generally, this transition occurs at the wavelength where the absolute value of blackbody emission exceeds the incident solar radiation [66], because after this wavelength the power emitted will be higher than the absorbed. The λ_{cut} (T) decreases with increasing the operating temperature, as highlighted in Fig. 3.1. When the operating temperature increases over 200 °C, the blackbody emission starts to overlap the solar spectrum and λ_{cut} is such that a significant part of the solar spectrum is in the range for which $\alpha_\lambda = 0$, which means that part of the incoming solar radiation will be lost in favour of reduced thermal radiation losses (Figure 3.1).

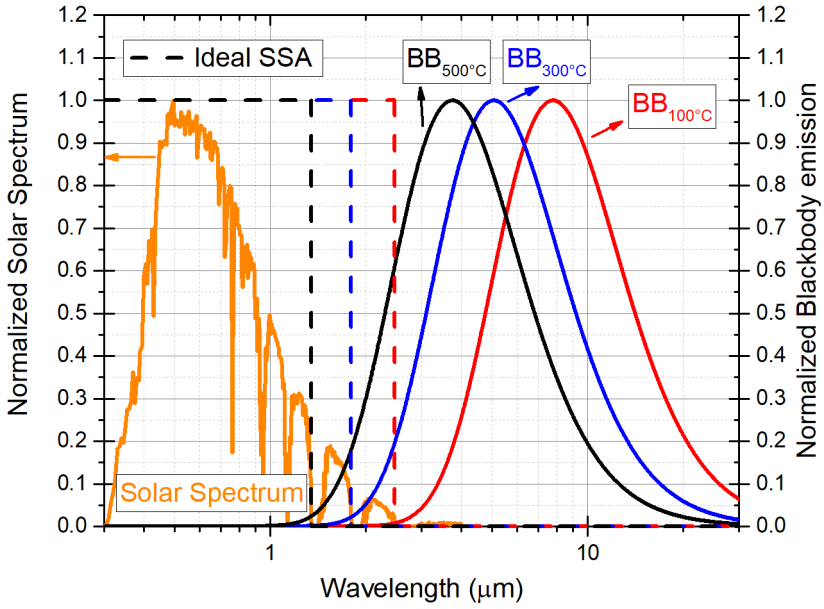

Figure 3.1. Normalized solar spectral irradiance (orange line) and normalized BB emission spectra at different temperatures: 100 °C (solid red line), 300 °C (solid blue line), and 500 °C (solid black line). Ideal absorptivity curves for solar selective absorbers with different cut-off wavelength λ_{cut}, depending on the operating temperature (dashed lines).

It is clear from equation 3.9 that, in absence of concentration (concentration factor C = 1), the thermal efficiency η_t has a strong temperature dependence due to the Stephan Boltzmann emission term that can be mitigated by a very low value of the thermal emittance. The presence of concentration C >1 reduces the radiation loss term, and the emittance loses importance with respect

to the solar absorptance term. Since the blackbody irradiance is temperature dependent, also the ideal λ_{cut} that maximizes the thermal efficiency, depends on the absorber operating temperature and as well as on the concentration factor, as illustrated in Figure 3.2.

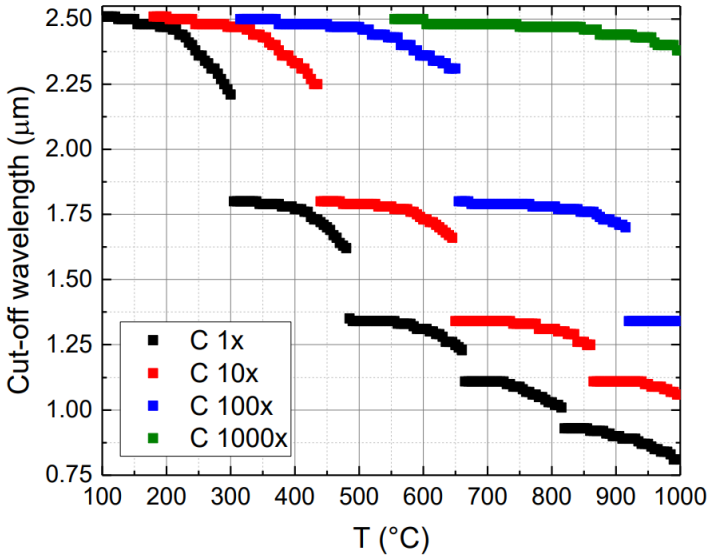

Figure 3.2. Ideal cut-off wavelength as function of the absorber temperature for different concentration factors.

3.3 Relative importance of α and ε

Temperature is a key parameter in the design of a selective absorber and the proper importance must be given to the role of α and ε. A very deep analysis was conducted about this subject by Cao et al. in 2014 [66]. They came out with a formula to quantitative estimate the relative importance of α and ε for all the possible solar thermal applications and introduced two important concepts that guided the designing activity of the novel absorbers presented in this thesis: absorber efficiency η_{abs}, eq. 3.11, and weighting factor w, eq. 3.12.

$$\eta_{abs} = \frac{q_h}{G_{Sun}\, C} = \alpha - w\varepsilon \tag{3.11}$$

$$w = \frac{\sigma_{SB}(T_{abs}^4 - T_{amb}^4)}{G_{Sun}\, C} \tag{3.12}$$

The absorber efficiency η_{abs} is postulated as the ratio between the heat directed to the pipes q_h of the collector and the total solar irradiance G_{Sun} incident over the absorber, considering the presence of the concentration factor C due to the presence of reflectors, see eq. 3.11. η_{abs} is also expressed as combination of α and ε through weighting factor w which fixes the relative importance between the two parameters. w is defined as the ratio between the maximum exchangeable heat via radiation with the ambient at temperature T_{amb} and the solar light incident over the absorber, G_{Sun} times C. In other words, w quantifies the relative importance of the emission mechanism against the light absorption. In the following Fig. 1.4, w calculated by eq. 3.12 is shown versus T_{abs} for three

different levels of concentration C = 1, 10 and 100 at fixed T_{amb} of 25 °C and G_{Sun} of 1 kWm^{-2}. The region w > 1 is marked by the yellow background. As expected, for a fixed C, the increase of T_{abs} produces the increase of w while for a fixed T_{abs}, an increase of C reduces w. From this graph it is possible to focus the situation about the plate absorbers for unconcentrated panels. The lack of reflectors limits the use of Fig. 1.4 just to the curve C = 1. In case of traditional not evacuated flat panels, the maximum reachable temperature is around 100 °C, matching values of w sensibly lower than 1. On the other hand, thanks to the high vacuum insulation, the operating temperature can reach values up to 200 °C and w increases up to 2. This profound change of w cannot happen for any other solar devices working with concentration, as the absorption mechanism is always more important than emission (w < 1).

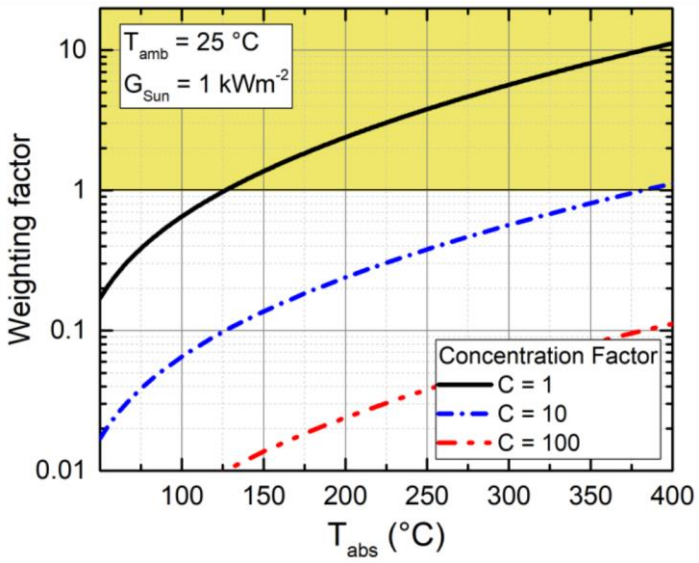

Figure 3.3. The weighting factor w calculated by eq. 3.12 is shown as function of the absorber temperature T_{abs} for three concentration factors C = 1, 10 and 100 for a fixed ambient temperature T_{amb} = 25 °C and solar irradiance G_{Sun} of 1 kWm^{-2}. The yellow zone stresses the points where w is bigger than 1, that is the unique condition of evacuated flat plate panels without concentration.

3.4 Types of Selective Solar Absorbers

The introduction in the market of the HVFPCs working without concentration up to 200 °C is relatively recent, and the lack of plate absorbers designed to work under these new condition of w > 1 pushed the research toward their study and optimization. The design and production of novel absorbers optimized to work at w > 1 lead to the analysis of the most adopted manufacturing processes. Six are the basic techniques to build a selective solar absorber. They are well known in literature [17,67] and a summary scheme is reported in Fig. 3.4 and listed below:

• **intrinsic absorbers** [68]. They are made of materials with intrinsic selectivity (transition metals, semiconductors), induced by dielectric dispersion as a function of wavelength. Unfortunately, no natural materials have a perfect ideal selectivity;

• **semiconductor-metal tandems** [69,70]. The semiconductor (most likely Si, Ge, and PbS), which efficiently absorbs the visible light, is deposited over a metal reflector, which reflects the long wavelength radiation;

• **multilayer absorbers** [71,72]. They consist of alternating layers of dielectric and metal and the working principle is based on the multiple reflections at the layer's interfaces, which enhance the absorption of the incoming light;

• **ceramic-metal composites** (cermets)) [66,73]. They consist of nanoscale metal particles embedded in a ceramic matrix, and are made of an AR layer, one or more cermet layer(s) that act as the primary absorber, and a reflective substrate to help minimizing the absorption of undesired IR wavelengths. They show a good selectivity at high temperatures;

• **textured surfaces** [74,75]. In this case dendrite or porous microstructures are used to generate multiple internal reflections, to trap the incident light in the visible spectrum while rejecting the longer wavelengths (IR range);

• **photonic crystals** [76,77]. They are made of periodic arrangements of materials with high and low dielectric constants. It generates a photonic bandgap in which certain wavelengths are fully reflected for all incident angles and polarizations.

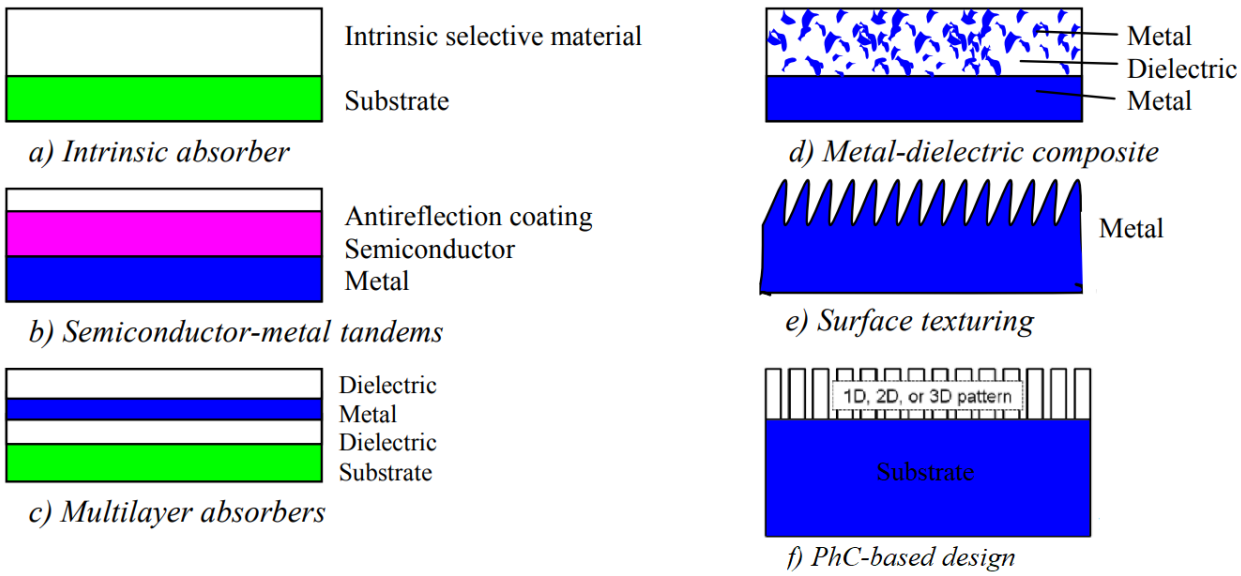

Figure 3.4. Schematic of the various design of selective solar absorbers: (a) intrinsic absorbers, (b) semiconductor-metal tandems, (c) multilayer absorbers, (d) cermets (metal-dielectric composites), (e) surface texturing, and (f) PhC-based designs. Adapted from [16].

3.5 Substrates

Many of the presented selective solar absorbers make use of a metallic IR reflector substrate, because they take advantage of the properties of the coating that will efficiently absorb the visible

light while being transparent to the long-wavelength radiation, that will be reflected by the low emissivity metal reflector. With that said, the thermal emittance of the metallic substrate ($\varepsilon_{sub}\ (T)$) is a parameter of primary importance in terms of overall efficiency of the collector (eq. 3.13). This is particularly true for high vacuum insulated collectors. In fact, for standard flat plate collectors the absorber uncoated side is insulated by rock wool, while the coated side is in air or inert atmosphere, plus they will not reach high temperatures and so and it is not useful to provide a low emissivity surface finishing to further reduce substrate emissivity. In HVFPCs the solar absorber is suspended in the vacuum envelope, and both the coated and uncoated side of the absorber exchange heat mainly in form of thermal radiation with the surroundings. For this reason, together with the high temperatures reached thanks to the high vacuum insulation, it is extremely useful to provide a low emissivity substrate to reduce the thermal losses.

$$\eta_{panel} = \alpha_s - \frac{\varepsilon_{abs}\,(T)\,\sigma_{SB}(T_{abs}^4 - T_{amb}^4)}{C \cdot G_{Sun}} - \frac{\varepsilon_{sub}\,(T)\,\sigma_{SB}(T_{abs}^4 - T_{amb}^4)}{C \cdot G_{Sun}} \qquad (3.13)$$

The ideal substrate, in addition to good optical properties should be cheap, chemically stable and have high temperature resistance. Table 3.1 (adapted from [78]) lists the thermal emittance of some typical metals that can be used as substrates for solar absorbers. Copper and aluminium have the best trade-off between cost of the bulk and optical properties, and they are the most used substrates. Stainless steel has a thermal emittance of one order of magnitude higher than the lower emissive metals as copper, but its use is almost mandatory for absorbers that should resist to high temperature applications, thanks to its superior mechanical properties and thermal stability.

Table 3.1. Thermal emittance for some typical metals in increasing order. Approximate range to 500 °C, from lowest to highest value. (Adapted from [78]*)*

Thermal Emittance	**Materials**
0.01-0.03	Pure silver (Ag), polished
0.02-0.03	Pure copper (Cu), polished
0.02-0.03	Pure gold (Au), polished
0.03	Pure tungsten (W)
0.02-0.06	Pure aluminium (Al), polished, unoxidized
0.05	Wrought commercially pure aluminium (Al)
0.05	Pure iron (Fe), unoxidized
0.05-0.07	Pure nickel (Ni), polished
0.04-0.09	Commercially pure nickel (Ni), cleaned
0.07	Pure molybdenum (Mo)

0.06-0.1	Pure chromium (Cr)
0.1	Carbon steel, polished
0.2-0.3	Austenitic stainless steel, cleaned
0.2-0-4	Ferritic stainless steel, polished

3.6 Thermal Stability

Thermal stability is a rather important parameter for selective solar absorbers because a stable absorber guarantees its performances all along its service lifetime (that should be superior or at least equal to the lifetime of the solar collector itself, usually 20-25 years). The thermal stability is defined as the capacity of the materials to withstand performance degradation due to changes of the properties of the material generated by high temperature activated processes and thermal shocks. Thermal shocks could affect the performance of multiphase solar absorbers because the difference between the expansion coefficients of the various phases generate thermal stress among the phases leading to microcracking, peeling, bulging [79]. Solid state diffusion mechanisms between the different phases of the coating and between the coating and the substrate involve alteration of the optical properties and a deterioration of the performances of the coatings [80]. Diffusion barriers are used to limit or slow down interdiffusion phenomena. Exposure to air, humidity, water, and pollutants are another cause for deterioration of the absorber, but not in the case of high vacuum insulated collectors, where thermal stress and diffusion are the main important mechanisms in terms of performance deterioration.

3.6.1 Short duration heat treatment

Short duration heat treatments consist in heating the solar absorber in a vacuum furnace at temperatures usually higher than the operating ones, for short periods of time (order of 10 hours). Preliminary information about the thermal stability of the coating could be collected by measuring the optical properties of the coating before and after the heat treatment. Example of this kind of treatment could be found in [66,81].

3.6.2 Accelerated ageing

Absorber optical properties are measured and optimized during design process at room temperature, but these properties may vary with the operating temperature and can change during the operation time. For this reason, it is advisable to evaluate the optical properties of the absorber at working temperature and predict the aging behaviour of these coatings. The International Energy Agency (IEA) formulated an accelerated thermal stability testing and service life predication method for solar absorber coatings [42]. This method is currently the standard named ISO/CD 12592, 2 "Solar Energy – Materials for flat-plate collectors – Qualification test procedures for solar surface durability". Such standard, being developed for standard collector working in air at low temperature. The standard assumes that the degradation is caused by diffusion processes according to the Arrhenius' law. The activation energy E_T, according to Arrhenius' law, is the fundamental coating parameter that determines the ageing resistance at the operating temperature.

The exponential temperature dependence of the Arrhenius law allows to perform accelerated aging tests using a temperature higher than the operating temperature and to estimate the failure time (the time at which the absorber efficiency is reduced more than the value defined according to the reported standard). However, the absorber temperature changes during the normal working conditions. Such temperature variations can be summarized by a temperature frequency function f(T) that represents how many hours the absorber is at temperature T during one-year operation. It is possible to replace the function f(T) with an effective constant temperature T_{eff} that produces the same aging effect than the real f(T). The degree of aging of a coating can be evaluated through the Performance Criterion (PC), which can be evaluated by measuring the optical characteristics of the absorber. The PC value is periodically measured during the tests, and the ageing test is stopped when a measurement returns a PC value higher than the one defined as the maximum degradation for a service lifetime of 25 years (Standard ISO/CD 12592, 2). The time when the PC reaches its maximum acceptable value during testing is not experimentally accessible and it is usually extrapolated from the different measurements and used to evaluate the service lifetime. Because this method has been developed for collectors working in air at low temperature, it is not adequate to evaluate the service lifetime of solar absorber in HVFPCs. For this reason, a review of the current standard is necessary, and it will be a part of this PhD study (section 7).

3.7 Summary

The keys aspects of primary importance to achieve high solar-to-thermal conversion efficiency, especially when the thermal radiation is the main thermal loss mechanism, as in the case of HVFPCs, are the control of the radiative properties of the Selective Solar Absorbers (section 3.3) and the decrease of the substrate thermal radiation losses (section 3.5). The use of a multilayer structure appears to be the best suited for the control of the radiative properties of the SSA, because it allows to manage thermal emission still guaranteeing high solar absorption and excellent thermal stability, they have a flexible design, and they are easy to be realized at industrial level. To proof the service lifetime of SSA working in HVFPCs, the current standard must be revised in order to take in account the relative importance of thermal emittance and the higher working temperature of HVFPCs.

4. Methods and experimental setups

Thin film and coatings that are the basis of selective solar absorber designs and architectures are usually fabricated using Physical Vapour Deposition techniques (PVD). PVD defines a variety of vacuum-based deposition methods, for which the target material is evaporated from a solid (or liquid) source and then condensed in solid phase on the substrate [82]. Most used PVD techniques are sputtering and evaporation. A variety of techniques are used to characterize the properties of the fabricated coating like surface composition, depth distribution, film thickness, structure, roughness. These techniques are based on probing methods as scanning probe methods, photon, electron, and ion methods [83]. This chapter briefly introduces the PVD fabrication methods and thin film characterization instrumentation used in this work. A custom made calorimetric instrument and a vacuum oven developed in collaboration with TVP Solar [13] and CNR-ISASI [84] of Naples is also described in this chapter.

4.1 Sputtering

Sputtering deposition is a type of physical vapour deposition technique based on the sputtering phenomena: when a solid surface is bombarded with energetic ions, surface atoms of the solid are scattered backward due to collisions between the surface atoms and the energetic particles as shown in Figure 4.1 [85].

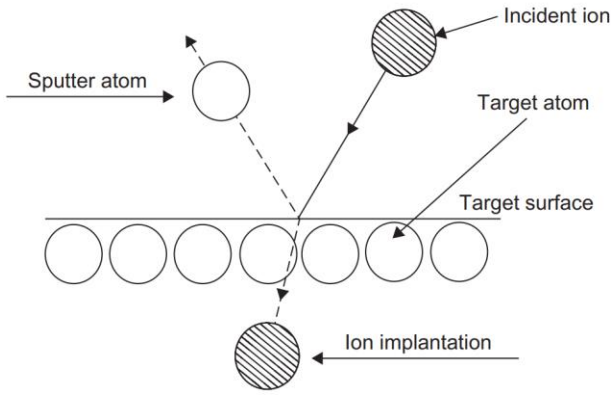

Figure 4.1. Sputtering process, scheme of concept. (Adapted from [85]*).*

Sputtering deposition technique allows to deposit film coatings of thickness that ranges from a few Angstroms to micrometres. There are several types of sputtering systems including Direct Current (DC) diode, Radio Frequency (RF) diode, DC Magnetron Sputtering (DCMS) and RF Magnetron sputtering (RFMS), DC Reactive Magnetron Sputtering (DCRMS) and RF Reactive Magnetron sputtering (RFRMS). The simplest system is the DC diode, shown in Figure 4.2, left. The system is composed of two planar electrodes (a cathode and an anode). The surface of the cathode is composed by the material to be sputter-deposited, while the substrates are placed on the anode. To sustain the sputtering process, the vacuum chamber is filled with an inert gas (usually Argon), at pressure of the order of 1^{-5} Pa. By applying a DC voltage between the electrodes, a glow discharge (plasma) is generated. The Ar^{+} ions generated in the glow discharge are accelerated by the potential

difference towards the cathode where they hit and sputter the target material that leaves the cathode and ends on the substrates. In DC sputtering systems the target needs to be an electrical conducting material to ensure the current flow (thus the glow discharge) between the electrodes. If the target is an electrical insulator the sputtering discharge cannot be sustained because positive surface charges will build up on the target insulator material. For insulating materials Radio Frequency (RF)s puttering is used. RF technique works alternating the electrical potential between the electrodes to avoid a charge building up the target. Figure 4.2, right shows an RF system [85].

A sputtering process is defined as reactive sputtering when the atoms sputtered from a target (usually a metal target) and reactive molecules introduced in the system during the deposition chemically react to form and deposit on the substrate a compound thin film. As a reactive source is usually used a gas. The gas source can be a pure reactive gas or a mixture of pure gases or a mixture inert gas – reactive gas [85]. The introduction of reactive processes complicates inevitable the deposition because control over the new additional parameters is needed. Usually sputtering processes are subject to hysteretic behaviours that may affect the deposition. Parameters like partial pressure of the reactive gas or the pumping speed are of fundamental importance to control the reactive process and the quality of the film [86]. Reactive sputtering process can be carried on all the standard sputtering equipment like (DC), (RF), (DCMS) and (RFMS), and it is widely used in coating industry.

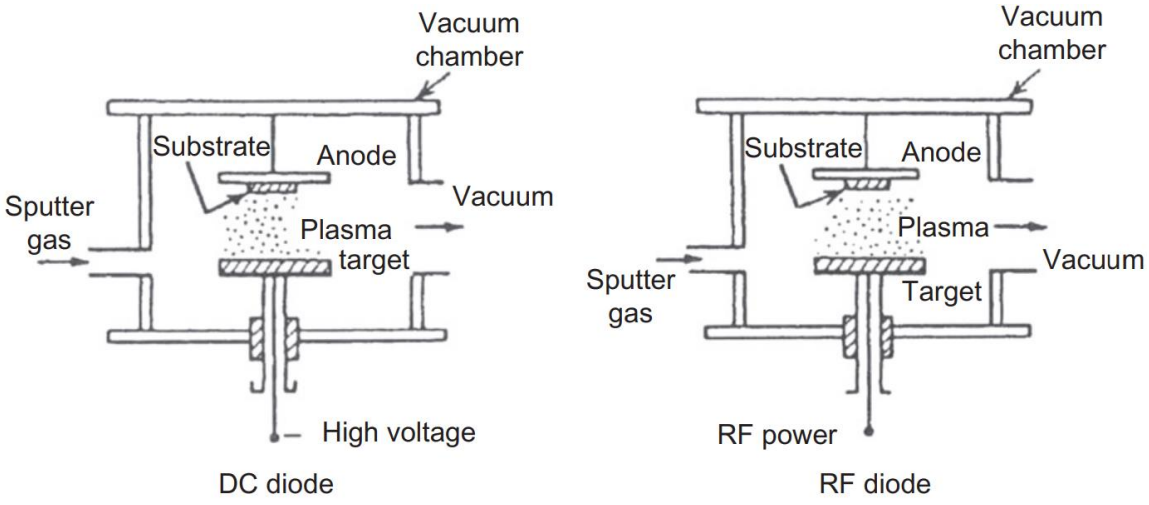

Figure 4.2. Sputter deposition systems: DC and RF diode. (Adapted from [85]*)*

Lowering the pressure in the chamber could increase the deposition rates of the sputtering process, and it could avoid process gas molecules being included in the growing film, affecting the film properties. Due to the low working gas pressure, the sputtered particles traverse the discharge space without collisions, which results in high deposition rate and a film with less impurities. If the pressure is too low however, the plasma discharge cannot be sustained as too few positive ions can be generated (few particles per unit volume due to the low pressure will result in few collisions between electrons and process gas particles). To lower the pressure magnetron sputtering is

introduced (Figure 4.3). In magnetron sputtering systems a magnetic field is used to trap electrons in the glow discharge, by driving them along drift paths in closed loops. The electron trapping effect increases the collision rate between electrons and inert process gas molecules allowing to sustain the plasma. So, the magnetic field increases the plasma density, which leads to increases of the current density at the cathode target, effectively increasing the sputtering rate at the target [85].

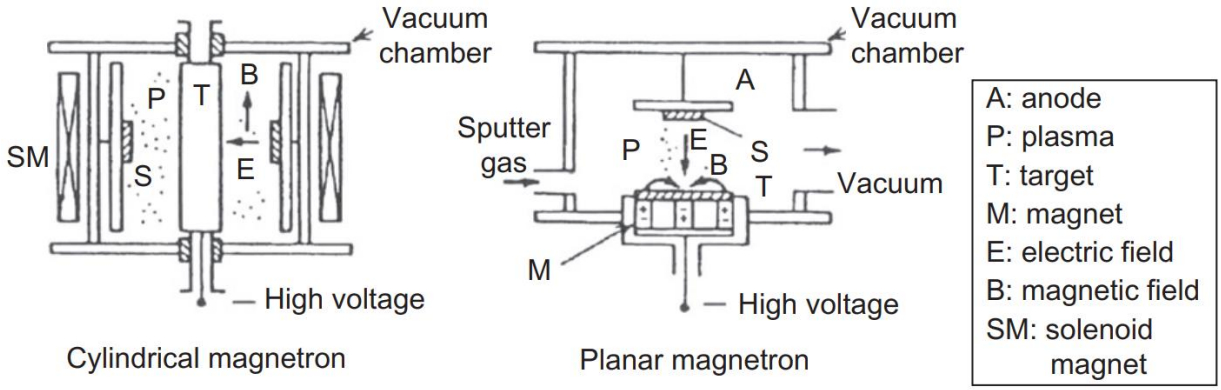

Figure 4.3 Sputter deposition systems: magnetron sputtering. (Adapted from [85]*)*

Experimental setup

The sputtering system used to deposit the multi-layer coating samples presented in this thesis is shown in Figure 4.4. The system has a cylindrical vacuum chamber equipped with four sputtering targets of 10 cm diameter placed at 90 degrees from each other, Figure 4.4 b). A rotating supporting disc with four sample holders allows to place the substrates under the desired cathode and deposit up to four different materials without breaking the vacuum, Figure 4.4 c). The distance between the cathodes and the substrate is set to 10 cm, and the substrate is static during deposition. Flow rates are controlled by means of flowmeters and mass flow controllers. Pressure in the chamber, during the sputtering process, is measured by a capacitance gauge (Pfeiffer CMR 364). All samples are loaded in the chamber the day before and pumped down overnight by a 1500 l/s turbomolecular pump to obtain the same base pressure of about $2x10^{-5}$ Pa. Before gas injection, the pumping speed is reduced by a throttle valve without affecting the base pressure. A rotating shutter placed at few cm from the cathodes (Figure 4.4 b)) is used to control the deposition time and, as consequence the layer thickness.

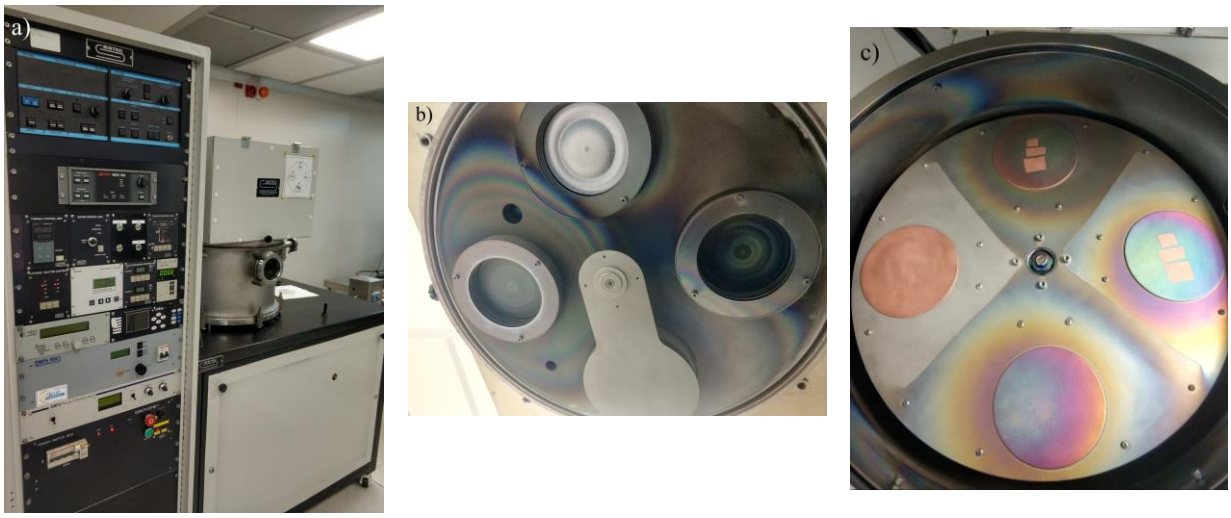

Figure 4.4 Sputtering deposition system. The sputtering apparatus a). Sputtering targets b). Rotating supporting disc with four sample holders c).

4.2 Electron beam

Electron beam evaporation (e-beam) is a physical vapour deposition technique, useful to produce thin film coatings. Using e-beam technique we can deposit film coatings of thickness that ranges from a few Angstroms to micrometres. Figure 4.5 shows the basics of electron beam deposition technique. An electron beam is usually generated by thermionic emission. The generated beam is accelerated thanks to a potential difference of the order of 10 kV. Using focusing magnets the high kinetic energy electron beam is focused on the material to be evaporated. Part of the kinetic energy of the electrons is converted into thermal energy, causing the material evaporation. Vapours of the target material will deposit on the substrates properly arranged in the upper part of the vacuum chamber. The evaporating material could be in form of ingots or pellets, and a crucible is usually used to contain the pellets. The filament that generates the beam and the target material are placed in a way that they don't see each other, to prevent the filament to be covered with the evaporating materials. A magnetic field provided by the so-called 'deflecting magnets' is used to bend the beam and direct it to the target. Additional magnetic fields could be used to steer the beam over a larger surface of the evaporation material. In electron beam systems the pressure in the vacuum chamber needs to at least lower than 10^{-2} Pa to allow the passage of the electrons from the electron cannon to the target material and avoid arcs generation. Rotating sample holders are often used to guarantee thickness uniformity of the deposited film on the substrate. To monitor the thickness of the deposited film during the deposition thickness monitors are used. Thickness monitors are usually based on an exposed oscillating quartz crystal whose frequency decreases as material accumulates. Because the thickness monitor is positioned at a certain distance from the substrate to avoid interferences, it measures a thickness that will be different from the actual thickness on the substrate, so a tooling factor (geometry dependent) is used to correct the reading output of the thickness monitor, so that it corresponds to the actual thickness of the coating on the substrate.

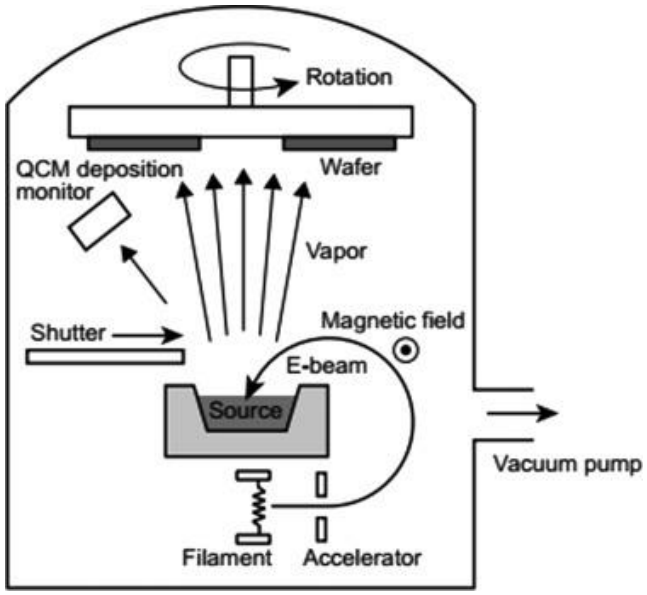

Figure 4.5. Electron beam physical vapour deposition technique, scheme of concept (adapted from [87]*)*

Experimental setup

Figure 4.6 shows some details of the electron beam apparatus used to deposit some of the presented multilayer absorbers. The deposition chamber is equipped with an electron beam evaporation source and four routable crucibles, Figure 4.6 d): it is possible to deposit the desired number of layers alternating the four materials without breaking the vacuum. The e-beam system used is equipped with a rotating planetary that guarantees the samples thickness uniformity and the deposition of several substrates in the same conditions, Figure 4.6 c). A thermocouple allows to monitor temperature during the whole process: samples temperature never exceeds 80 °C. Prior to depositions, the vacuum chamber is pumped down to a base pressure of 10^{-5} Pa and the materials are slowly outgassed to remove unwanted trapped gases (impurities). The deposition is controlled by a thickness monitor (Inficon model XTC/3). The tooling factor of the thickness monitor was calibrated depositing a thicker layer (about 500 nm) that was measured using a profilometer (KLA Tencor P-15). The step to be measured was obtained by lift-off procedure in acetone, using standard photolithographic technique. The thickness monitor automatically controls the e-beam current, to keep the evaporation rate constant, as well as a shutter that stops the deposition once the desired thickness has been deposited. A careful calibration allowed us to obtain a thickness control in the order of 1 nm. All the depositions shown in this work have been carried out on smooth unheated glass substrates (roughness 1 nm).

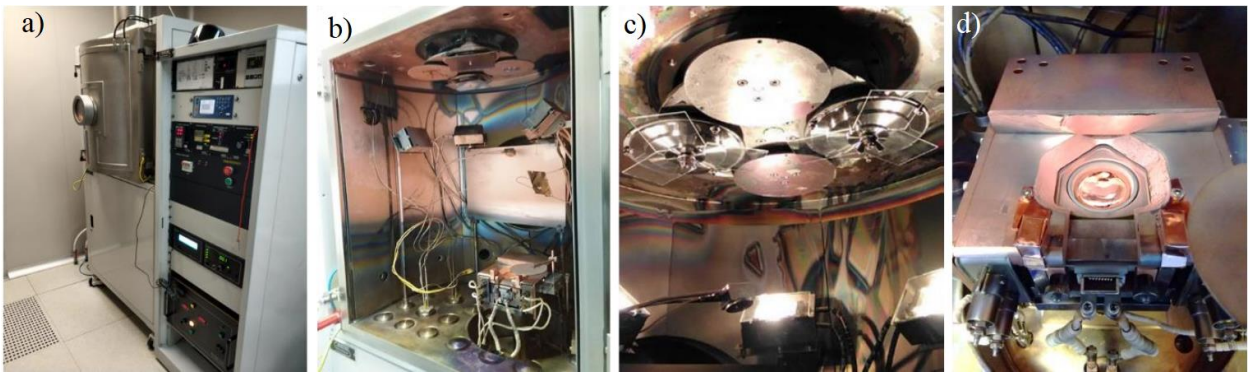

Figure 4.6. E-beam deposition system. The electron beam apparatus a). Vacuum chamber b). Glass substrates mounted on the rotating planetary (thickness monitor sensor is also visible) c). Multiple crucible e-gun and copper crucible.

4.3 Mini Test Box

The Mini-Test-Box (MTB) is a custom experimental apparatus used to measure the absorptance and the thermal emittance of SSA in operating conditions (high vacuum, high temperatures) [88]. Figure 4.7 shows the Mini Test Box apparatus: it consists of a stainless steel high-vacuum chamber, closed by an extra-clear float glass, which can host a flat absorber suspended by four springs of negligible thermal conductivity (visible in Figure 4.7c). The internal pressure is kept below 10^{-3} Pa by a turbomolecular pump in order to suppress convection and to reduce residual gas thermal conduction down to a negligible level. A thermocouple fixed to the sample measures the temperature of the absorber under investigation. Additional thermocouples record the temperature of the vessel and the glass. An array of LED lights is used to perform indoor measurements (Figure 4.7 b, c). The LED system has been calibrated to precisely control the supplied power per unite area and guarantee the spatial uniformity of the light irradiance. Details about LED system are in [89]. The Mini Test Box is also equipped with a tilting support and a pyranometer to carry on outdoor measurements with solar irradiation spectrum [90] (Figure 4.7 a).

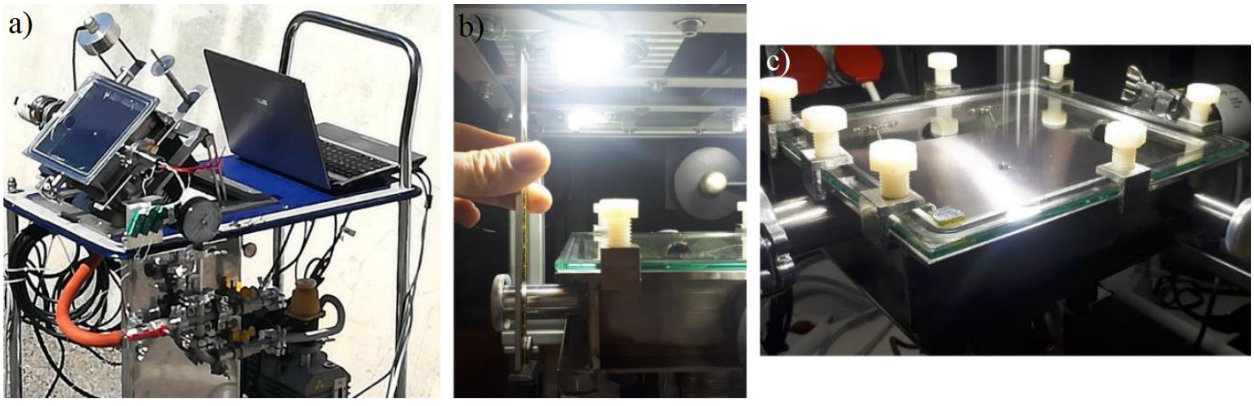

Figure 4.7. Figure 4.3.1 Mini Test Box apparatus under direct solar illumination (a) and under LED light illumination (b and c).

The Mini Test Box measures the actual absorptance and thermal emittance using a calorimetric approach. The variations of the temperature of the sample are strictly related to the absorbed power and the radiative power losses through the following power balance equation:

$$m_a\, c_p(T_a) \frac{d\,T_a}{dt} = \alpha_L\, A\, \tau\, P_{in} - \bar{\varepsilon}_a(T_a)\, \sigma\, A\, (T_a^4 - T_{amb}^4) - \bar{\varepsilon}_{sub}(T_{sub})\, \sigma\, A\, (T_a^4 - T_{amb}^4) \quad (4.1)$$

Being m_a the sample mass, c_p the specific heat, α the absorptance, A the sample Area, P_{in} the incident Power per unit area, $\bar{\varepsilon}_a(T_a)$ the absorber emittance, $\bar{\varepsilon}_{sub}(T_{sub})$ the equivalent substrate emittance. During cooling down phase illumination is stopped and $P_{in} = 0$: Equation 4.1 allows to evaluate the thermal emittance of the tested sample $\varepsilon_{sample}(T_a) = \bar{\varepsilon}_a(T_a) + \bar{\varepsilon}_{sub}(T_{sub})$, because the only unknown term is $\varepsilon_{sample}(T_a)$ itself. Once $\varepsilon_{sample}(T_a)$ has been calculated Equation 4.1 can be used during heating up phase data to evaluate α. A detailed description of the measurement can be found in [65,91]. The behavior of an absorber mounted in the MTB has also been numerically simulated using COMSOL Multiphysics [92].

The Mini Test Box also allows to perform experimental measurements of the efficiency of a solar coating at different temperatures through stagnation measurements. To perform the efficiency measurements the absorber is illuminated with different light power using the calibrated LED illumination system described in [89] and the absorber stagnation temperature is recorded. In such configuration the power losses are equal to absorbed power:

$$\varepsilon(T_{aS})\ \sigma_{SB}(T_{as}^4 - T_{amb}^4) + \varepsilon_{sub}\, \sigma_{SB}(T_{as}^4 - T_{amb}^4) = \tau_{glass}\, \alpha_L\, P_{LED}(T_{aS}) \quad (4.2)$$

where the solar spectrum is replaced by the spectrum of the LED lump used to illuminate the absorber [89], $P_{LED}(T_{aS})$ is the light power provided by the calibrated LED system and T_{aS} is the absorber stagnation temperature at the given LED power. As consequence, at $T = T_{aS}$ the efficiency can be calculated, as reported below:

$$\eta(T) = \tau_{glass}\, \alpha_s - \frac{\tau_{glass}\, \alpha_L\, P_{LED}(T_{aS})}{H} \quad (4.3)$$

where H is the irradiated power chosen as reference and set to 1000 Wm^{-2}, $\tau_{glass} = 0.91$, $\alpha_S = 0.95$ in the case of Mirotherm® coating actually mounted on TVP Solar high vacuum flat collectors. Figure 4.8 reports the Mirotherm® overall efficiency (as from Equation 3.13, chapter 3.5) when mounted in the MTB (blue solid line), the numerical simulation of the experimental setup (red dash-dot line) and the overall efficiency experimentally measured using Equation 4.3 (black dots).

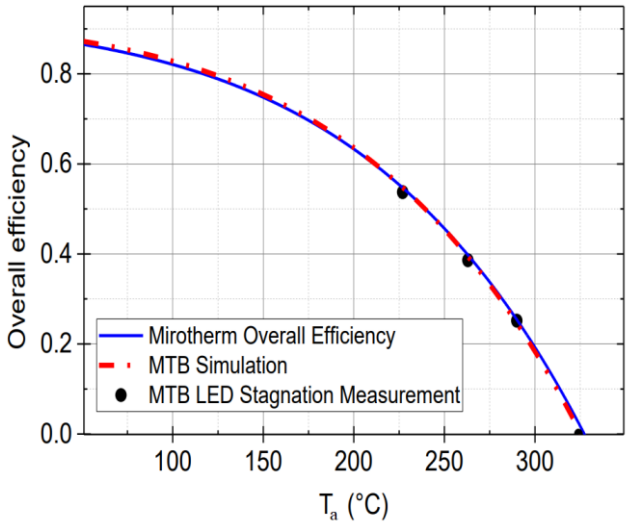

Figure 4.8. Overall efficiency versus Absorber temperature T_a (°C): Mini-Test-Box (MTB) simulated efficiency (red, dash dot), Led Measured MTB efficiency (black dots), Mirotherm® overall efficiency calculated using Equation 3.13 (blue solid line).

4.4 Vacuum Oven

The Vacuum Oven is a custom experimental apparatus used to perform aging test; it can work till 500 °C with high precision temperature control. Figure 4.9 shows the Vacuum Oven apparatus: it consists of a stainless steel high-vacuum chamber, with three copper plates inside supported by a steel structure (visible in Figure 4.9b). The copper plates are the heating elements, and they have a slot for the absorber of 10x10x0.8 cm^3, which represents the samples holder. The plates are heated by home-made heating cartridges; they consist in a ceramic tube with 4 holes in which a tantalum wire is inserted (Figure 4.9c). The wire tantalum is heated thanks to Joule effect and consequently the copper plates are heated. The Seneca Z-DAQ-PID controller was used to control the power to be driven to heating cartridges. It receives as input the temperature measured by a 4 wires PT100 inserted inside each copper plate and gives as output a 0-10 V signal. This signal is used as dimming controller for a Mean Well ELG-200 power supply, which deliver the exact amount of power to the heating cartridges. Thanks to this setup it is possible to control the temperature inside each copper plate with an uncertainty of ± 1 °C. The internal pressure is kept below 10^{-4} Pa by a turbomolecular pump to suppress convection and to reduce residual gas thermal conduction down to a negligible level.

An example of a test is reported in Figure 4.9d; it is important to notice that a high heating up and cooling down rates are necessary to minimize the time around the testing temperature. The heating up rate (max 8 °C/min) was adjusted through to the PID parameters optimization, considering also to avoid a temperature overshoot, while to obtain high cooling down rate (max 11 °C/min), nitrogen was fluxed inside the chamber at the end of the test to increase the pressure and trigger convection phenomena.

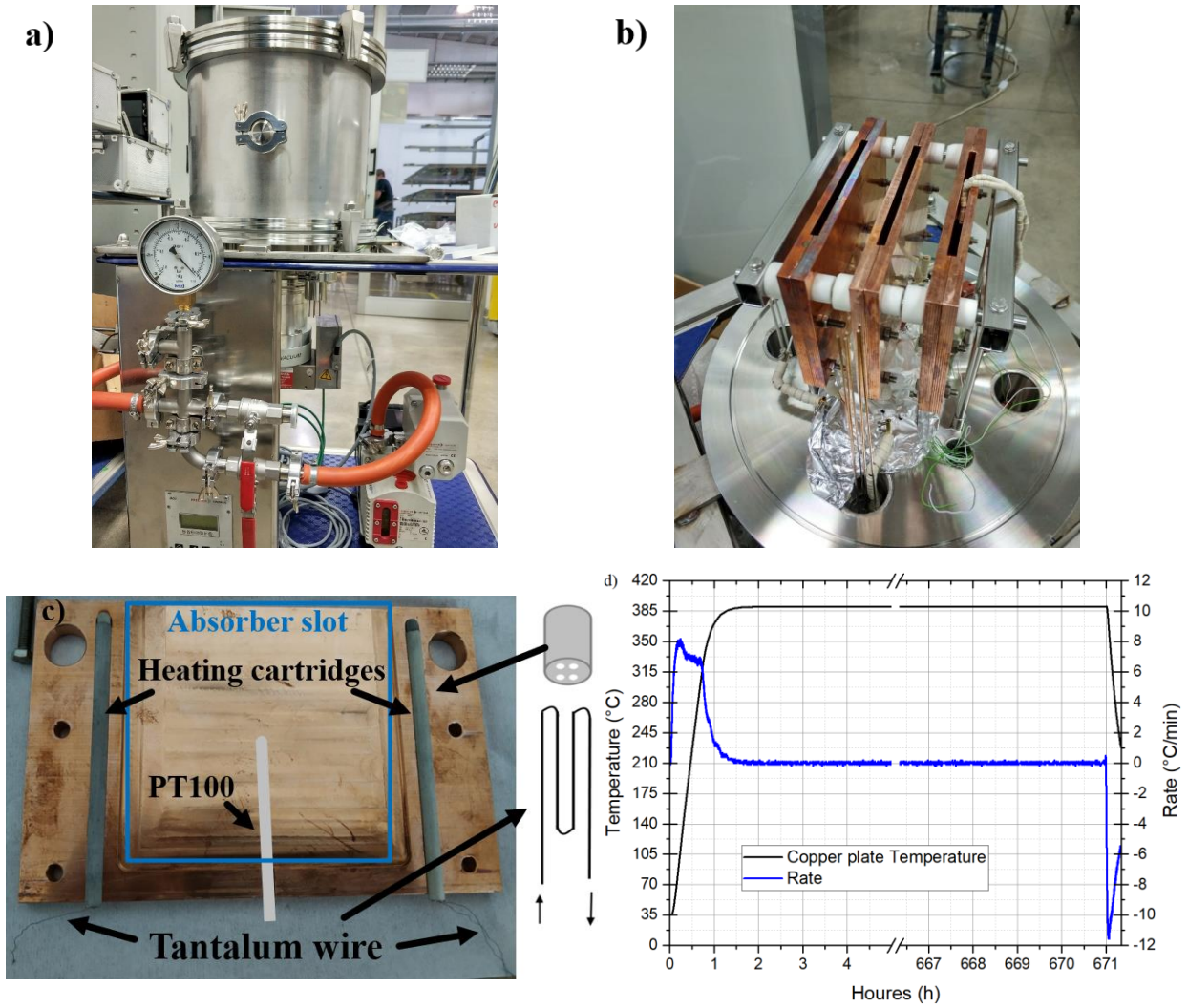

Figure 4.9. a) Vacuum Oven apparatus, b) Vacuum Oven inner part, 3 copper plates supported by the stainless steel structure, c) Copper plate particular, d) Example of a test at 390 °C.

4.5 Ellipsometry

Ellipsometer is by far the most important and complex instrument in our study, as it allows to characterize the film thickness and optical constants. Its layout and working principle are shown in Fig. 4.10: by means of an optical fiber, the light ejected from a source reaches the polarizer, where the state of polarization of the light is defined. Then, the light strikes the sample, and the reflected component is modulated and sent to the analyzer and monochromator, that separates the light into its various components before it reaches the detector.

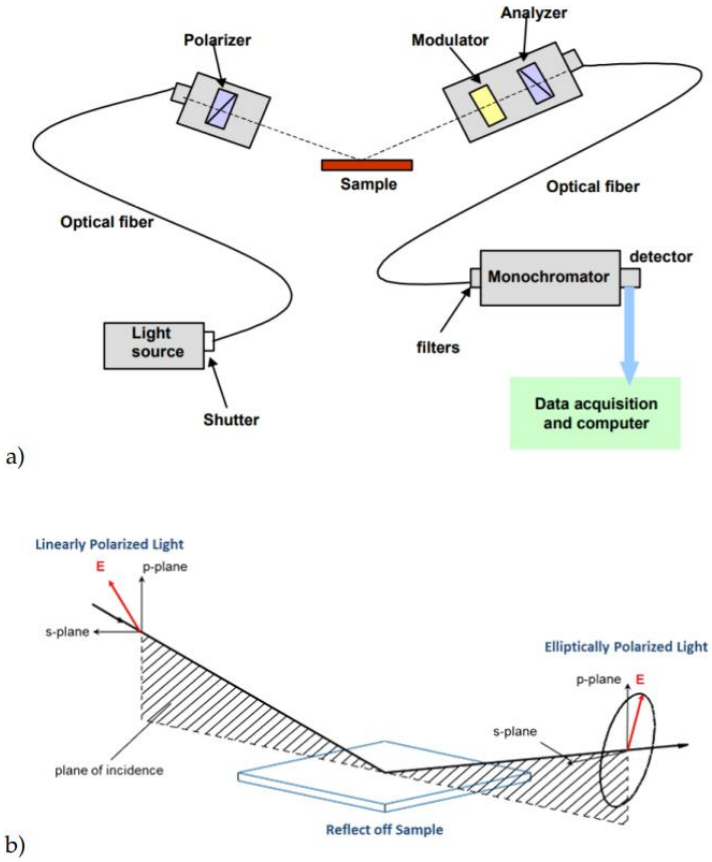

Figure 4.10. a) Layout and b) working principle of a classical ellipsometer.

Ellipsometric measurements are based on the measurement of the change in polarization of the light incident on the sample of interest and depends on the optical properties and thickness of the individual materials included in the sample. The change in polarization is quantified by the amplitude ratio and phase difference:

$$\rho = \frac{r_p}{r_s} = \tan(\psi)e^{i\Delta},$$
$$\tan(\psi) = \frac{|r_p|}{|r_s|} \in [0, 90°], \quad (4.4)$$
$$\Delta = \delta_p - \delta_s \in [0, 360°].$$

The quantities r_p and r_s are the Fresnel reflection coefficient for s- and p-polarization, respectively, while ψ and Δ are the ellipsometric angles: from them it is possible to obtain the optical properties of the sample. Unfortunately, they cannot be directly converted into the optical constants of the material, but are used to validate a material structure model that allows to predict the material optical properties, i.e. the complex refractive index, by means of mathematical relations, dispersion formulae. There are several degrees of freedom in this analysis: incident angle, as well as thickness,

roughness and refractive index of each layer included in the sample. Any of these properties is varied to improve the match between experiment and calculation. Therefore, it is important to carefully choose the model and control the χ^2 value returned by the fit, which defines its quality. Figure 4.11 shows an example of the measured quantities Ic and Is, which are functions of ψ and Δ according to:

$$I_s = \sin(2\psi) \cdot \sin(\Delta), \qquad (4.5)$$

$$I_c = \sin(2\psi) \cdot \cos(\Delta).$$

and the relative fit lines, which agree with the measurement.

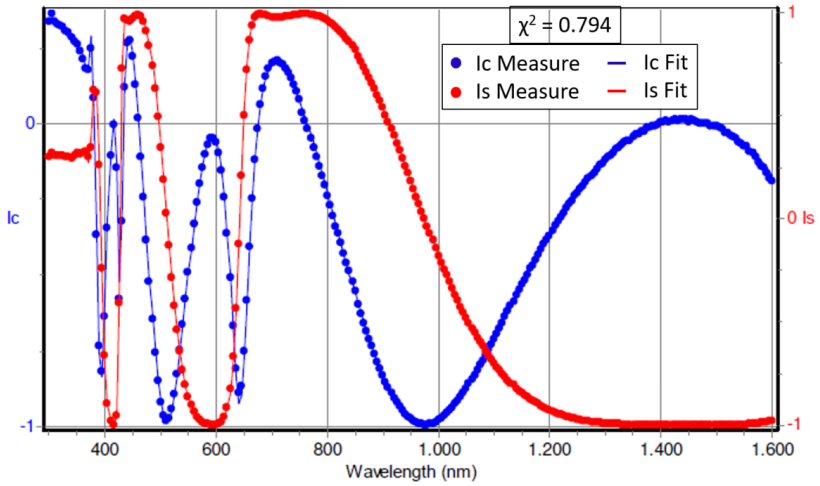

Figure 4.11. Example of a good fit ($\chi^2 < 1$): the ellipsometric measured quantities I_c and I_s (blue and red dots, respectively) and the fitted quantities (I_c as a blue line and I_s as a red line) are compared.

In our analysis, the model used to fit the ellipsometric data faithfully reproduces the experimental samples. Also, two additional thin layers were included to simulate the roughness at the interface between the substrate and the film and on the film surface, as shown in Fig. 4.12. Measurements must be conducted at the Brewster angle (θ_B) of the substrate, where the highest sensitivity is observed. In fact, it corresponds to an angle of incidence at which the p-polarized light is perfectly transmitted through a transparent dielectric surface, with no reflection. It can be calculated from the indices of the two media:

$$\tan(\theta_B) = \frac{n_1}{n_0} \qquad (4.6)$$

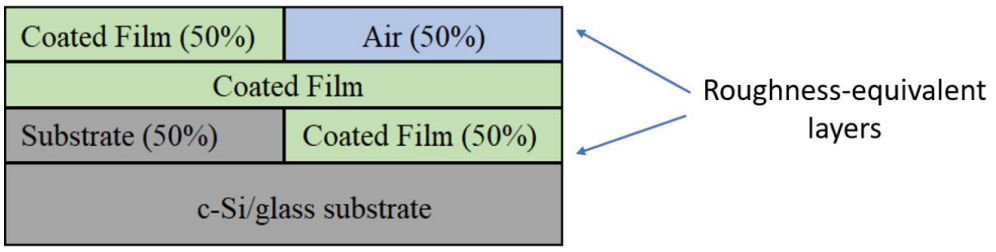

Figure 4.12. Diagram of samples (not to scale), including roughness-equivalent layers.

Experimental setup

Measures of the samples in this work were carried out using a phase modulated spectroscopic ellipsometer by Horiba Jobin Yvon – UVISEL [93]. The ellipsometer is equipped with a xenon lamp and two detectors: it can analyze the optical response in the wavelength range from 190 nm to 2100 nm. A picture of the ellipsometer setup is shown in Figure 4.13.

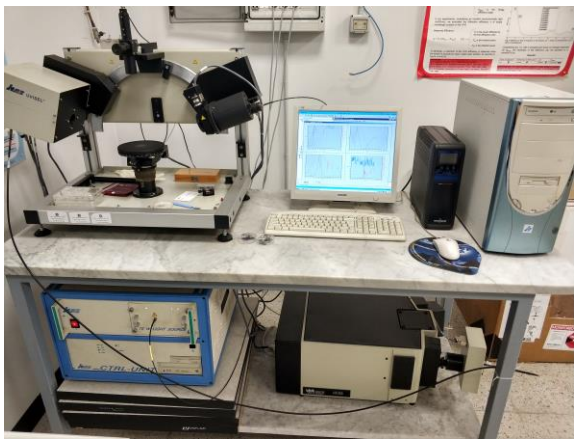

Figure 4.13. Spectroscopic ellipsometer Horiba Jobin Yvon – UVISEL, used for ellipsometric measurements

To obtain reproducible and reliable results all the films to be analyzed were deposited on aluminum film, thick enough to be considered optically infinite, and grown on a glass support to be optically flat. An optically flat substrate allows to neglect the roughness parameter in the models that describe the fabricated thin film sample. Incidence angle of the incoming polarized light could be varied, and it is set so 70° for aluminum substrates. Software DeltaPsi from Horiba allows to perform data analysis of the measured samples. Figure 4.14 shows the ellipsometric measured quantities Ψ and Δ (dotted) and the relative fitting (lines) for a Cr_2O_3/Cr bilayer on Aluminum substrate, model in Figure 4.14, inset. Forouhi-Bloomer formula was the dispersion model used for the chromium oxide [94,95], while for chromium and titanium metals Drude-Lorentz [96] dispersion relation has been used (details in section 5.1).

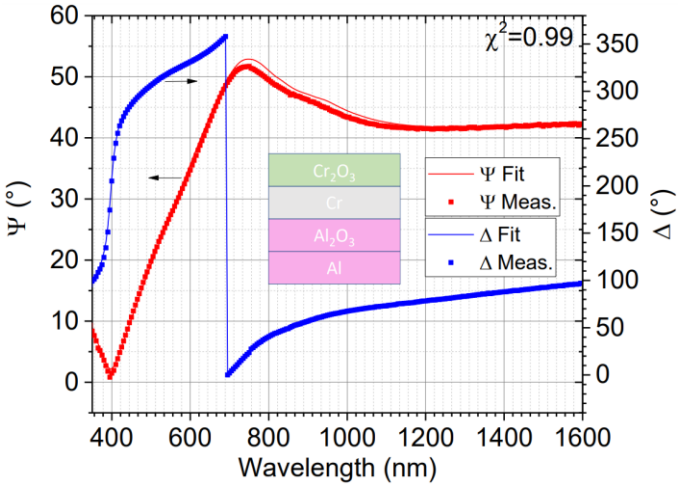

Figure 4.14. Measured ellipsometric quantities Ψ (red, dotted) and Δ (blue, dotted), and the same fitted theoretical quantities Ψ (red line) and Δ (blue line). Al substrate is optically infinite, thickness for Al_2O_3, Cr and Cr_2O_3 is of 7, 15 and 70 nanometers.

4.6 Integrating sphere and OSA

An integrating sphere coupled with an Optical Spectrum Analyzer (OSA), showed in Fig. 4.15, was used to perform hemispherical reflectance measurements, in the short wavelengths' region, from 350 to 1750 nm. The inner part of the integrating sphere is coated with a diffusive material which provides a high reflective surface and allows to obtain a homogeneous distribution of radiation thanks to the multiple Lambertian reflections on the inside of the sphere. A light source illuminates the sample and the fraction of light reflected by the sample under analysis is read by the spectrometer, which measures the spectral power (Wnm^{-1}) over the range of investigated wavelengths. Then, the reflected power can be estimated from the comparison with a measurement made on a reference sample, which has a known reflectivity (ρ_{ref}):

$$\rho = \frac{R_{sample}}{P_i} = \frac{R_{sample} \cdot R_{ref}}{P_i \cdot R_{ref}} = \frac{R_{sample}}{R_{ref}} \cdot \rho_{ref} \qquad (4.7)$$

where P_i is the power intensity incident on the sample, R_{sample} and R_{ref} the spectral power reflected by the sample and by the reference sample, respectively. The reference sample used in this work is the Spectralon WS-1-SL diffuse reflectance standard from Labsphere, with a 99% reflectivity in the range of 400 to 1500 nm, while > 96% reflectivity in the range of 250 to 2000 nm. Alternatively, optical transmittance spectra in the range of 200 nm to 2500 nm can be recorded using a spectrophotometer. The working principle is shown in Fig. 4.14: a lamp provides the source of light; the beam of light strikes the diffraction grating, which works like a prism and separates the light into its component wavelengths. The grating is rotated so that only a specific wavelength of light reaches the exit slit; at this point the light interacts with the sample and the detector measures the transmittance of the sample, i.e. the amount of light that passes completely through the sample and strikes the detector.

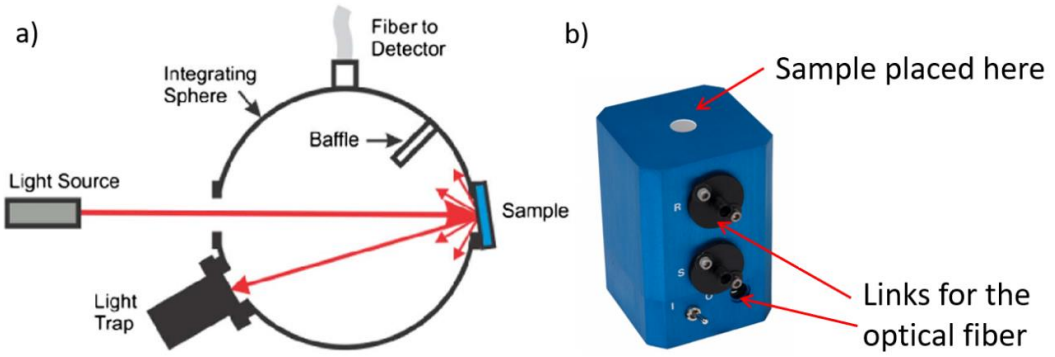

Figure 4.15. Working principle (a) and design (b) of the integrating sphere.

4.7 Fourier Transform Infrared Spectroscopy (FTIR)

The Fourier-transform Infrared Spectrometer (FTIR) has been used for reflectance measurement in the range of 1.5 µm to 30 µm. The working principle of this instrument is shown in Fig. 4.16: a broadband infrared light beam is sent to an interferometer which produces an optical signal with all the IR frequencies encoded into it. Then, the light beam hits the sample, which absorb a fraction of light at certain wavelengths and the signal is decoded by applying a Fourier Transform (FT). The FT convert the intensity-time spectrum into intensity-frequency, and the spectral reflectance is estimated from the comparison with a reference sample.

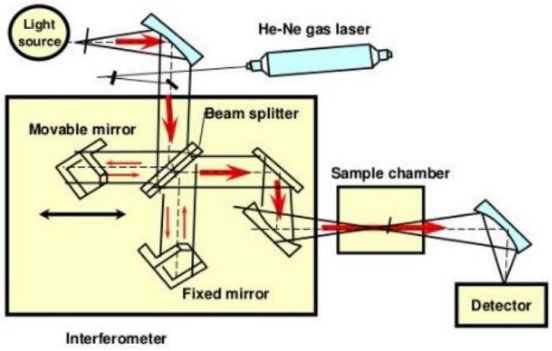

Figure 4.16. Fourier Transform Infrared Spectroscopy (FTIR), working principle.

Experimental setup

For NIR to FIR measurements (1.4-20.0 µm) Jasco FT/IR 6300 Fourier Transform Infrared Spectrometer has been used, aluminium film has been used as the reference reflectance standard. Figure 4.17 shows experimental result of optical spectroscopy carried out with the Integrating sphere (blue line) and FT-IR experimental measurements (green line) (numerical simulation of the coating is also reported). The two instruments overlap in the range 1.00-1.75 µm indicating a good agreement between the two different measurement techniques.

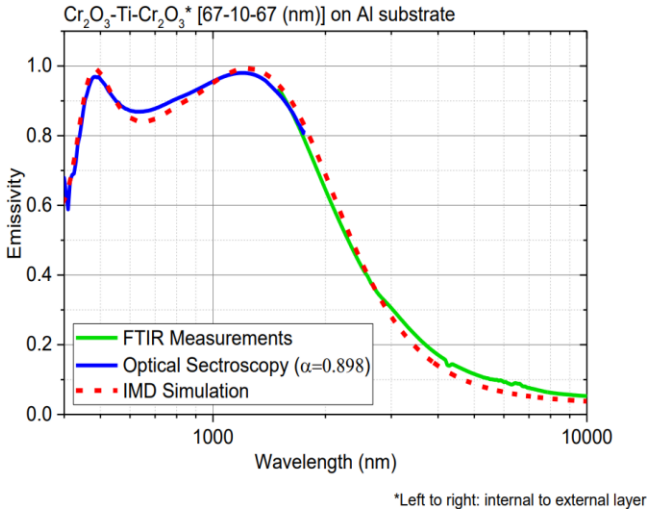

Figure 4.17. Cr_2O_3-Ti-Cr_2O_3 multi-layer on Al substrate: experimental result of optical spectroscopy carried out with the Integrating sphere (blue line), FT-IR experimental measurements (green line), numerical simulation of the multilayer (red dotted line)

4.8 Profilometry

A profilometer is an instrument used for measurements of surface properties, i.e. roughness, step height, etc. Its working principle is shown in Fig. 4.18: a probe tip, in direct contact with the surface to measure, moves linearly along it record the vertical change (z-direction), which is useful to reconstruct the surface profile. Measurements of step height are usually obtained using standard photolithography, i.e. by applying a mask on the substrate before deposition and chemically removing it after deposition of the thin film, and are useful to estimate the deposition rate. An example of this kind of measurement is shown in Fig. 4.18.

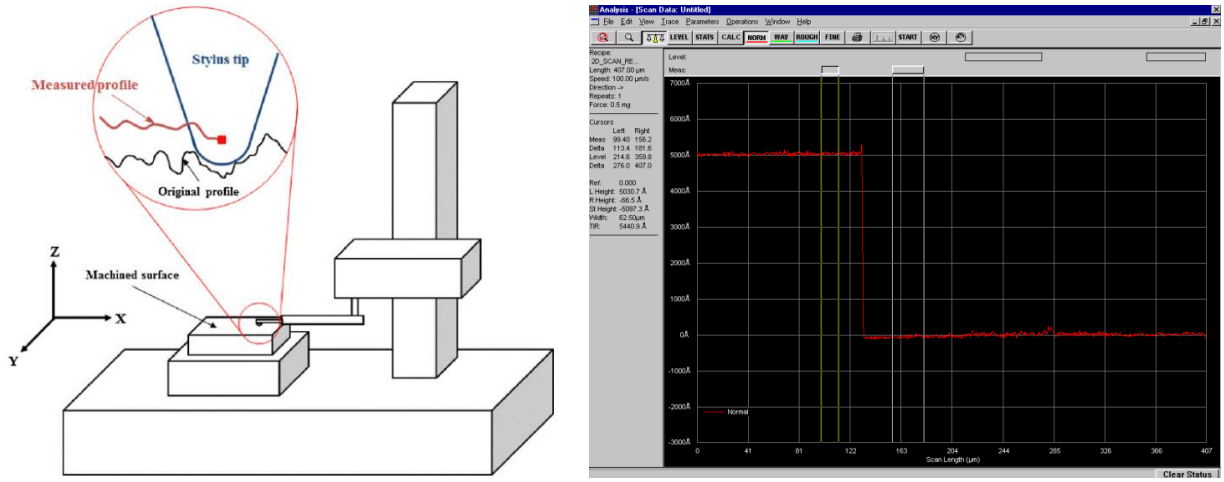

Figure 4.18. a) Working principle of a stylus type profilometer [97]*, b) Step height measurement measured with KLA Tencor P-15 profilometer.*

5. Improvement of energy conversion efficiency in HVFPCs

As discussed in section 3.3 the emerging technology of HVFPCs places itself in a new field where the high working temperatures without concentration require special attention to be given to both solar absorptance and thermal emittance in the design of the selective coatings. The two most widespread solar thermal devices (Concentrating solar power (CSP) and standard flat plate solar collectors) justify the lack of interest by both the SSA manufacturers and the researchers in fine-tuning the thermal emittance against solar absorptance. In fact, for CSP the solar absorptance is dominating over thermal emittance because of the high value of the concentration ratio, while for the flat plate collectors the greater importance of solar absorptance over thermal emittance is justified by the low temperature output [66] (details in section 3.3). Commercial solution of solar selective coatings such as Mirotherm® and Sunselect® from Alanod [98], and several types of TiNOx® from Almeco [99] still result in excellent performances up to 150 °C, but for higher temperatures no marketed solutions neither research studies that propose a valid SSA coating optimized for HVFPC technology are released. There are in fact authors that tried to optimize a coating suited for high vacuum insulated flat collectors obtaining encouraging results but still far from being optimal. For example, Thomas et al. [100] optimized a solar coating for mid-temperature unconcentrated application, obtaining a stagnation temperature of about 230 °C under vacuum, still too low for the potentiality of HVFPCs. The same authors declare that the coating could be further optimized to potentially increase the stagnation temperature to about 300 °C, but they did not show experimental evidence, and not even in this case they would be able to outperform the existing commercial absorbers. The purpose of this PhD research project is to develop a method to optimize solar selective coatings well suited for HVFPCs emerging technology, focusing on a simple-to-realize, industrially feasible and robust selective coating, for both low and medium-high temperature applications. Among the possible SSA designs, as discussed in section 3, multilayer selective absorbers appear to be the best suited for the purposes of this work, because they allow to control thermal emission still guaranteeing high solar absorption and excellent thermal stability [101]. Multilayer architecture ensures the highest performance designs built and tested to date [17], their design is really flexible because it meets the need of having coatings qualified for different operating temperature by simply changing thickness of the layers leaving the architecture unchanged, it is easy to simulate and to optimize, while being simple to be industrially realized. As discussed in 3.4, multilayer absorbers consist in a stack obtained alternating a dielectric thin layer (high absorptance in visible range, transparent in Infrared region) and a metal layer, thin enough to allow for partial transparency. An antireflective layer is often used to reduce the reflection due to the generally high refractive index of the dielectrics composing the interference stack, further enhancing the performances of the coating. Like most of the selective solar absorbers designs they also make use of a metallic IR reflector substrate. Chromium Oxide and Chromium proved to be valid candidates for the dielectric layer and metal layer respectively. The choice fell on these materials because Cr_2O_3/Cr structure has been already deeply studied above all in form of ceramic-metal composite, being applied in commercial absorbers such as Mirotherm® or Sunselect® by Alanod [98]. A

$Cr_2O_3/Cr/Cr_2O_3$ multilayer deposited by e-beam has also been studied, showing interesting optical properties [102] and good thermal stability [103]. Last but not least, these materials are relatively cheap and easy to be handled. A single SiO_2 layer is used as antireflective coating to improve absorptance, while aluminum and copper are used as metallic IR reflector substrate.

5.1 Multilayer SSA Cr_2O_3/Cr based: optimization via custom algorithm

During this PhD project efforts have been made to perfect a new optimization method, based on the efficiency of the real coating that is considered as the fitness function of the optimization algorithm. The new optimization algorithm allows to find the best trade-off between solar absorptance and thermal emittance, that is strictly linked to the to the shape of the reflectivity spectrum $\rho(\lambda)$ of the coating. This method is particularly suited for the emerging technology of the unconcentrated flat plate solar collectors under high vacuum insulation, as they are able to reach high working temperature without concentration, with thermal emittance gaining importance on the solar absorptance [104]. The drawback of multilayer selective coatings is that multilayer coating architecture working principle is strongly based on multiple reflections at the interfaces between the layers composing the stack, so the performances of such solar absorbers are strongly affected by the thickness of the various layers. Aiming at the industrial mass production of these Selective Solar Absorbers we need to consider that the control on the deposition parameters could not be perfect, introducing errors on layer thicknesses, thus affecting the performances of the coatings. So, it is interesting to add to the designing stage a new, important parameter, that is the robustness of the performances of the coating for unpredicted errors on the thickness of the layers. Including this new factor as a part of the optimization process of a selective coating offers the possibility to pick not the absolute maximum of the solution, i.e. the coating with the highest performance in the range of possible solutions, but the coating with the highest performances that ensures the proper robustness for given errors on layer thickness.

5.1.1 Materials and architecture

For the multilayer selective solar absorber, Cr_2O_3 and Cr were chosen as the dielectric and high-absorption metallic layers, respectively. Further, copper was selected as the low-emissive metallic substrate, while the SiO_2 thin film served as the antireflective coating.

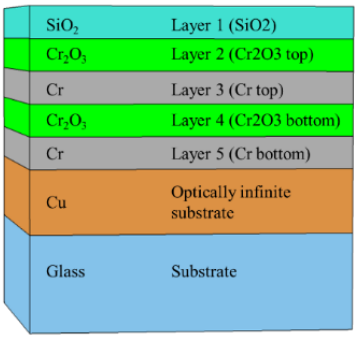

Fig. 5.1 Architecture used for the multilayer coating.

To exclude the effect of roughness on the radiative properties of the solar absorber, a low-emission substrate was deposited onto a smooth glass substrate. An optically thick copper layer (250 nm) was deposited using e-beam vapor deposition and then exposed to atmospheric air. Figure 5.1 shows the architecture used for the multilayer coating. As shown in the figure, a five-layer structure was used. The chromium layer directly deposited on the copper substrate acted as a bonding layer, while preventing the formation of emissive copper oxides during reactive sputtering deposition. Further, this layer was also integrated into the optimization process, allowing it to be part of the absorbing package.

5.1.2 Samples preparation and deposition techniques

To deposit the thin films, a magnetron sputtering machine has been used. Cr and Cr_2O_3 thin films are deposited using a 99.99% pure Cr cathode by means of DC Magnetron Sputtering (DCMS) and DC Reactive Magnetron Sputtering (DCRMS) process respectively. Argon was used as a sputtering gas for Cr deposition and oxygen was added as a reactive gas for Cr_2O_3 deposition. For Cr deposition, argon flow was set at 3.3 sccm corresponding to a pressure of 0.2 Pa. During Cr_2O_3 deposition an oxygen flow of 1.6 sccm was chosen to obtain stable deposition condition that produces Cr_2O_3 films with the required dielectric properties. The multilayer Cr_2O_3/Cr/ Cr_2O_3 is completed with SiO_2 thin film used as Anti-Reflective Coating (ARC) and deposited by RF magnetron sputtering (RFMS) technique in pure argon atmosphere. The deposition conditions, for the various layers, are reported in Table 5.1 [105]. The parameters of the copper substrate are also reported in the table to complete the SSA structure. E-beam PVD technique has been used for the deposition of the copper film that acts like the optically thick substrate. The deposition was performed in a vacuum pressure of $4 \cdot 10^{-5}$ Pa with a deposition rate of 2 Å per second. The uniformity of the deposition on the substrates is guaranteed by a rotating planetary. Prior to copper layer deposition the glass substrates have been cleaned with soapy water first, then with ultrasonic baths in both acetone and isopropyl alcohol, and finally dried with a nitrogen flux. The reported deposition rates are calculated by the ratio between the layer thickness measured with the profilometer (KLA Tencor P-15) and the recorded deposition time. The step height to calibrate the deposition rates are typically about 300 nm and they are obtained in dedicated layers by lift-off procedure in acetone, using standard photolithographic techniques.

Table 5.1. Deposition parameters for the layers composing the Cr_2O_3/Cr based multilayer stack.

Layer	PVD	Ar flow (sccm)	O_2 flow (sccm)	Power (W)/ Current (A)	Discharge Voltage (V)	Deposition Rate (nm/s)	Pressure (Pa)
Cu	E-Beam Evaporation	/	/	/	/	0.2	4E-5
Cr_2O_3	DCRMS	3.3	1.6	0.5A	390	0.14	0.3
Cr	DCMS	3.3	0.0	0.3A	300	0.44	0.2
SiO_2	RFMS	4.0	0.0	200W	/	0.11	0.3

5.1.3 Optical characterization

To evaluate the refractive indices of the material constituting the multilayer absorber we used the ellipsometric technique. Measures were performed on layers deposited in the same conditions reported in section 5.1.2. Since on the copper surface it is present a copper oxide that growths in time, to obtain reproducible and reliable results the layers to be analyzed were deposited on a different substrate, consisting of an aluminum film, thick enough to be considered optically infinite, and grown on a glass support to be optically flat. Thickness and complex refractive index ñ of the film were obtained by fitting the experimental data with numerical data returned by an optical model of the sample in which material dispersions are described by the proper dispersion formula. The experimental data were fitted by using the Forouhi-Bloomer formula for the chromium oxide [94,95], while for chromium Drude-Lorentz [96] dispersion relation has been used. Figure 5.2 a) and b) show the refractive index dispersion for both chromium and chromium oxide which best fits the ellipsometric experimental data, used for the optical simulations.

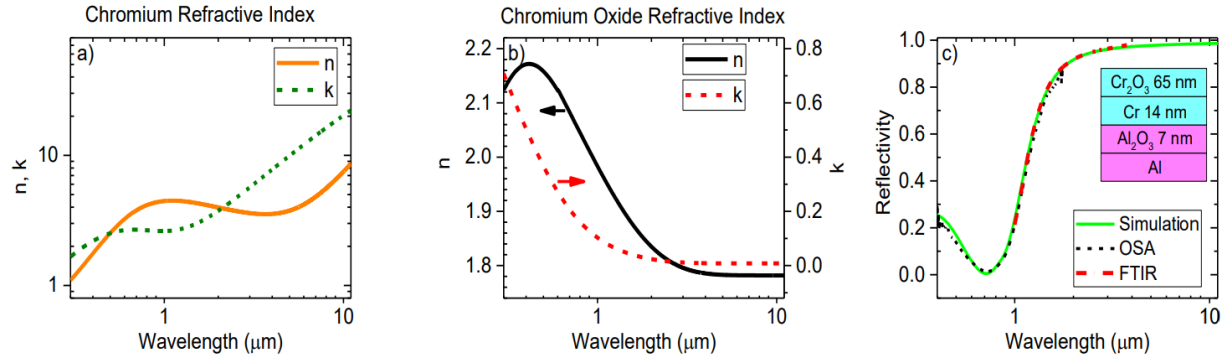

Figure 5.2. Refractive index and extinction coefficient obtained by fitting ellipsometric measurements for Chromium a) and Chromium Oxide b). c) The agreement between experimental data and simulation obtained using the reported refractive indices is shown: simulation (green, solid line), Optical Spectrum Analyzer (OSA) (black, dash line), Fourier Transform Infrared Spectroscopy (FTIR) (red, dash-dot line).

The refractive index of the pure Cr layer (Figure 5.2 a) shows the typical metallic characteristics (n and k indices increasing with wavelength), where k value greater than zero in all the wavelength range indicates that Cr layer is primarily responsible for the light absorption. Both the real and imaginary parts of Cr_2O_3 refractive index (Figure 5.2 b) decrease with the wavelength, showing a characteristic dielectric behavior. In particular, k index reaches values close to zero already in the visible region, which indicates the transparent properties of the film at longer wavelength. The reported refractive indices were able to fit Cr_2O_3 film for thicknesses from 15 nm up to 100 nm and Cr layer from 5 to 30 nm and they were obtained by fitting experimental data of several samples. The use of optically smooth surfaces allowed to exclude surface roughness effects in the models. Since the ellipsometric analysis is limited in the range between 300 nm and 1600 nm, refractive indices of both chromium and chromium oxide have been extended outside the measured wavelength range by using the respective dispersion relations. The results show good agreement with literature data [106–108]. Reflection measurements further confirm the effectiveness of the

obtained refractive indices: Figure 5.2 c) shows a comparison between measured and simulated reflection of a Cr_2O_3/Cr bilayer on aluminum substrate (model and layer thickness in inset). Integrating sphere coupled with an Optical Spectrum Analyzer (OSA) was used to measure the reflectance in visible and near-infrared range (0.35-1.75 μm) and Fourier Transform Infrared Spectroscopy (FTIR) was used to measure reflectance in range 1.00-4.00 μm. The two instruments overlap in the range 1.00-1.75 μm indicating a good agreement between the two different measurement techniques. The optical simulation of the sample under investigation uses the refractive indices reported in Figure 5.2 and literature data for Al_2O_3 and Al substrate [96,106,109]. The agreement between optical simulation and the reflectance measurements validates the studied refractive index for both chromium and chromium oxide in the whole wavelength range.

5.1.4 Optimization using genetic algorithm and robustness

A genetic algorithm (GA) was chosen to optimise the efficiency calculated using the MATLAB code. This algorithm is able automatically change the thickness of each layer and calculate the emissivity ε(λ) of the stack at each wavelength. The emissivity is computed according to the transfer matrix method [110] utilizing the experimental refractive indices. This search-based method is frequently used to solve constrained and unconstrained optimisation problems and to find optimal solutions for applications that are not well suited for solving classical optimisation algorithms, including problems wherein the objective function is discontinuous, nondifferentiable, stochastic, or highly nonlinear. GA is well suited for this application because it offers the possibility of sweeping a potentially large number of solutions (thickness combinations in this work case) and exploring the search space in a relatively short computational time. Further, being a global random search algorithm, the GA is independent of the gradient of the fitness function and carries less risk of being stuck in the local minima of the solution. Moreover, it is also independent of the initial conditions; however, the search space must be defined. This algorithm can maximize a fixed multilayer structure, without taking in account the layer position as design variable. The GA settings are the default parameters settled by MATLAB, the main settings are: population size = 50, number of generations = 500 and crossover fraction = 0.8.

The thickness of each layer was calculated through a Genetic Algorithm (GA) developed in MATLAB. At each iteration, the GA changes the thickness of the individual layers and, starting from the experimentally determined refractive indices and using the transfer matrix method, calculates the corresponding multilayer reflectivity spectrum. For each reflectivity spectra, ρ(λ), the GA derives the spectral emissivity/absorptivity of the structure, ε(λ)/α(λ). In fact, according to Kirchhoff's law of thermal radiation [111,112] and the principle of conservation of energy, the emissivity/absorptivity of an opaque object at thermal equilibrium satisfies the following relation: ε(λ) = α(λ) = 1 - ρ(λ). Once the emissivity/absorptivity is known, the GA evaluates the solar absorptance α_S and thermal emittance ε(T) according to eqs. (5.1) and (5.2) respectively:

$$\alpha_S = \frac{\int_{0\ \mu m}^{\infty \mu m}[1-\rho(\lambda)]S(\lambda)d\lambda}{\int_{0\ \mu m}^{\infty\ \mu m} S(\lambda)d\lambda} \qquad (5.1)$$

$$\varepsilon(T) = \frac{\int_0^\infty [1-\rho(\lambda)] E_{bb}(\lambda,T) d\lambda}{\int_0^\infty E_{bb}(\lambda,T) d\lambda} \quad (5.2)$$

where S(λ) ($Wm^{-2}\mu m^{-1}$) and $E_{bb}(\lambda, T)$ ($Wm^{-2}\mu m^{-1}$) are the solar radiation spectrum and the blackbody radiation spectrum respectively, depending on the radiation wavelength λ (μm) and temperature T(K). Next, these radiative parameters were used to evaluate the SSA efficiency (Eq. (5.3)):

$$\eta_{coat}(T_h) = \frac{q_h}{H} = \alpha_S - \frac{\varepsilon(T_h)\sigma_{SB}(T_h^4 - T_{amb}^4)}{H} \quad (5.3)$$

where q_h (Wm^{-2}) is the heat flux to the thermal system, T_h (K) is the absorber temperature, T_{amb} (K) is the environmental temperature, H (Wm^{-2}) is the sun-irradiated power, and σ_{SB} ($Wm^{-2}K^{-4}$) is the Stefan-Boltzmann constant. The $\eta_{coat}(T_h)$ was used as fitness function of the GA algorithm, allowing the maximization of this parameter.

To consider the robustness of the performances with error on layer thickness, the constraint introduced set the maximum loss in efficiency to be 2 percentage points, for errors on the layer thickness being within the 20% range. The constraint introduced in the GA sets the fitness function to acquire values only within a particular range for a particular percentage error in the thicknesses of the layers constituting the stack. Thus, solutions that are unable to respect the constraint are rejected, and the algorithm returns only thickness combinations that satisfy the constraints.

5.1.5 Results

5.1.5.1 Simulation results

Figure 5.3 shows the results of the optimization process performed using the GA and a commercial absorber (Mirotherm® from Alanod). Two different coatings were considered and optimised for working temperatures of 200 °C, and 300 °C (OPT_200, and OPT_300, respectively). Table (5.2) presents the optimal thickness combinations, solar absorptance values, and thermal emittance values for the two optimized and the commercial coatings. The reduction in metallic layers thickness for the OPT_300 compared to the OPT_200 allows to have a significant reduction in thermal emittance value at the expense of solar absorptance value.

Figure 5.3a shows the spectral reflectivity of the three coatings in comparison with the normalized solar spectrum. It is evident the way the cut-off wavelength $\lambda_{Cut\text{-}Off}$ shifts toward shorter wavelengths as the target working temperature increases. This shifting in $\lambda_{Cut\text{-}Off}$ is due to the blackbody emission peak shifting toward shorter wavelengths, and it is a well-known behavior for the ideal selective solar absorber.

The introduced optimization method based on the efficiency as a fitness function allows to find the best trade-off between solar absorptance and thermal emittance, that is strictly linked to the to the shape of the reflectivity spectrum ρ(λ) of the coating. This method is particularly suited for the emerging technology of the unconcentrated flat plate solar collectors under high vacuum insulation, as they are able to reach high working temperature without concentration, hence

requiring special attention to be given to both solar absorptance and thermal emittance in the design of the selective coatings.

Figure 5.3b shows the thermal emittance for the three coatings versus the temperature of the absorber. The coating optimized for higher working temperature (300 °C) shows a reduction in the thermal emittance of approximately 70% with respect to the Mirotherm coating. The reduction in the thermal emittance that reduces the radiative losses is obtained at the expense of 6% reduction in solar absorptance (see table 5.2).

Table 5.2. Optimal thickness combinations, solar absorptance α_S values and thermal emittance ε (T) for commercial coatings and OPT_200 and OPT_300.

Sample	T opt. (°C)	Layer thick. (Layer 1 to 5) (nm)	α_S	ε (100 °C)	ε (200 °C)	ε (300 °C)
Mirotherm®	-	-	0.945	0.062	0.070	0.081
OPT_200	200	72-55-10-27-15	0.936	0.026	0.031	0.040
OPT_300	300	65-45-8-14-10	0.889	0.017	0.020	0.025

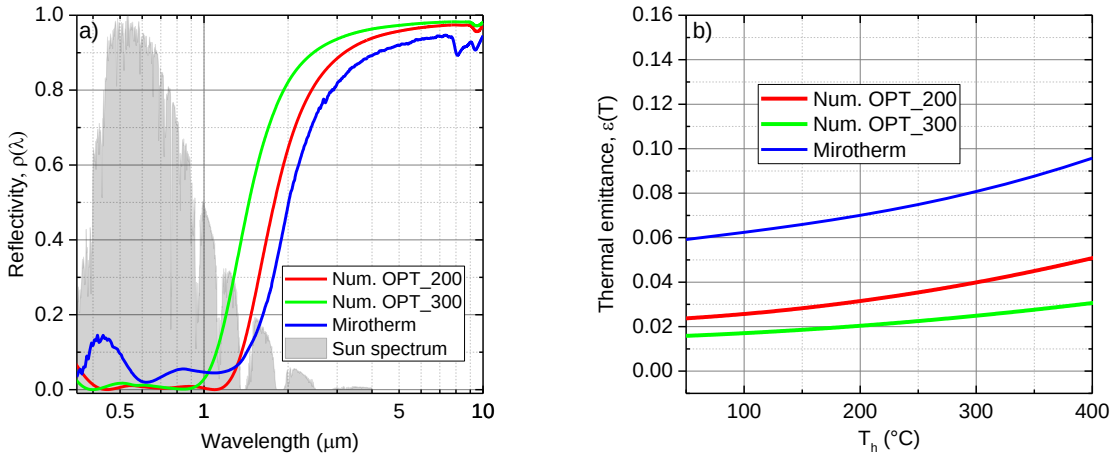

Fig. 5.3. Optical simulations. (a) Spectral reflectivity of two coatings optimised for a target temperature of 200, 300 °C (red, green curve, respectively) and of the commercial coating (blue line). Normalised sun spectrum, grey filled area. (b) Temperature dependent thermal emittance of two coatings optimised for a target temperature of 200, 300 °C (red, green curve, respectively) and of the commercial coating (blue line).

Figure 5.4 reports the coating efficiency (Eq. (5.3)) for the simulated multilayer for 1000 Wm^{-2} incident power; the optimization process guarantees the highest efficiency at the setpoint temperature in every case. The way the reduction in the absorptance in favor of a low thermal emittance translates in a lower value of the radiation losses is evident from the efficiency curve. This consequently led to lower efficiency at low temperatures but facilitates the maintenance of higher efficiencies at higher working temperatures.

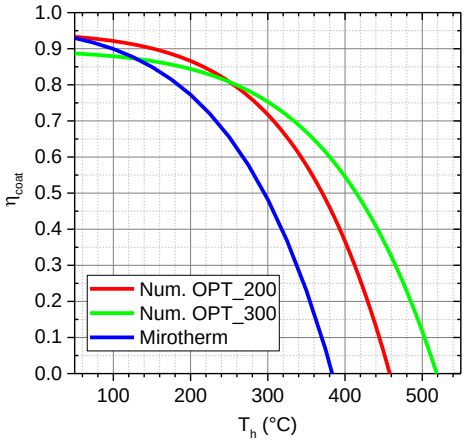

Fig. 5.4 Optical simulations of coating efficiency η_{coat} of two coatings optimised for a target temperature of 200, 300 °C (OPT_200, OPT_300; red, green curve, respectively) and of the commercial coating (blue line).

Influence of errors on layer thickness: robustness

To verify the robustness of the solution with respect to thickness variations, the efficiency for different thickness combinations of the multilayer stack was calculated. Each multilayer stack is obtained by varying the thickness of each layer around its optimal value. The maximum percentage error of the layer thickness was set to ±20% around the optimal thickness for each layer. To simplify the representation, only the values at the extremes of interval (+20% and -20%), coupled with the optimal thickness values, are reported in the figure. Thus, three different thickness values are possible for each layer. With three possible thickness values for each layer, and because the multilayer stack is composed of five layers, a total of 3^5=243 combinations are possible, identifying 243 possible multilayer stacks (combinations). In Fig. 5.5, the combinations are numbered sequentially from combination 1 to combination 243. Figure 5.5 clearly shows how the coatings are very stable in terms of efficiency; with a 20% error in layer thickness, on all the possible combinations, the efficiency difference is maintained below or at most equal to 2 percentage points. This figure shows an overview of the relationship between the variation in the thickness and its effect on the efficiency of the coating at the target optimization temperature. For example, the OPT_200 coating efficiency varies more smoothly with the combinations than the coating OPT_300. This can be attributed to the chromium bottom layer, which in the coating optimized at 200 °C reaches a thickness as high as 70 nm.

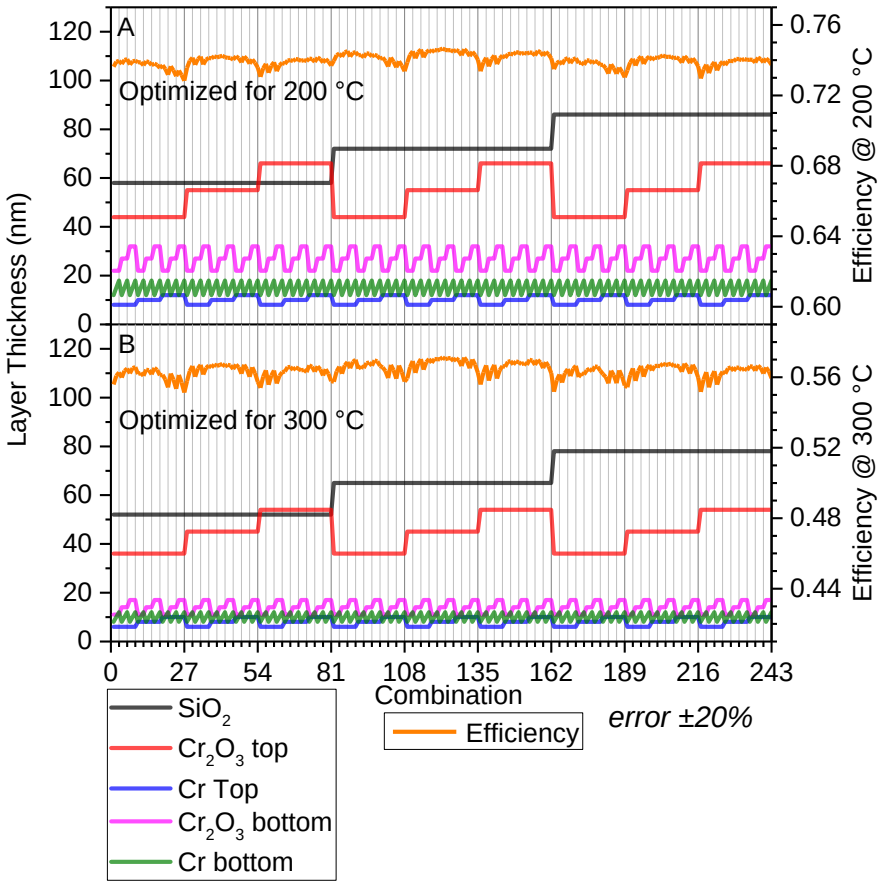

Fig. 5.5 Coatings OPT_200, OPT_300 (panel A, B respectively). x axis: each i^{th} combination identifies a different stack in terms of thickness, obtained by varying the thickness of each layer around its optimal value, in the case of three possible values for each layer and error=±20%. Left y axis: thickness value of each layer in nanometres for the i^{th} combination. Right y axis: efficiency evaluated at the target optimisation temperature related to the i^{th} combination.

Figure 5.6 shows the spectral emissivity 1- ρ(λ) for the two coatings optimized at 200, and 300 °C as red, and green dashed lines, respectively. The light-colored areas around the optimized curves represent the spectral emissivity curves for the 35 combinations for the same three coatings. This figure shows the way the variations in the layer thickness identify a band around the optimal value, defining the radiative parameters of each stack which determine the efficiency trend in Fig. 5.5. Moreover, it is evident that the change in layer thickness does not result in leaps in the reflectivity curves, but in a smooth transition around the optimal value inside the defined band.

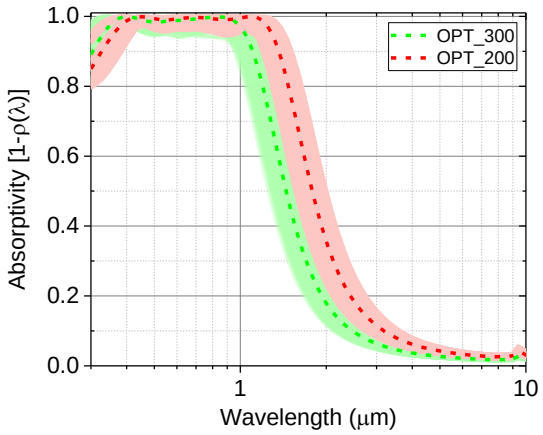

Fig. 5.6. Spectral emissivity 1- ρ(λ) for the coatings OPT_200 and OPT_300, in red and green. Dash curves: optimal thickness stack. Solid line curves light color: emissivity curves obtained by varying the thickness of each layer around its optimal value, in the case of three possible values for each layer and error = ± 20%.

Figure 5.7 shows, for each combination, the solar absorptance α_S (left y axis, purple) and the efficiency and thermal emittance ε(T) at the target optimization temperature for the two optimized coating (panel A, B), descending from spectral emissivity curves 1- ρ(λ) of Fig. 5.6.

This figure clearly shows the relative importance of the solar absorptance α_S and the thermal emittance ε(T) in determining the efficiency at different working temperature of the coating. It is interesting to note the way each of the three coatings handled these parameters differently.

For the coatings optimized at 200 and 300 °C, an overall decrease in both the solar absorptance and thermal emittance was observed, together with an increased variation in α_S and a decrease in ε(T). A higher variation in α_S does not considerably affect the efficiency of the solar absorber, whereas variations in thermal emittance are limited. Further, an analysis of the coatings OPT_200 and OPT_300 clarifies the importance of thermal emittance on the solar absorptance value with increasing temperature and clarifies the primary importance of considering the relative importance of α_S and ε(T) with the working temperature.

The optimization algorithm automatically satisfies the need to control α_S and ε(T) as a function of the target working temperature, fine-tuning the layer thickness to ensure the best performance, and the robustness required with errors in the thickness during the deposition stage.

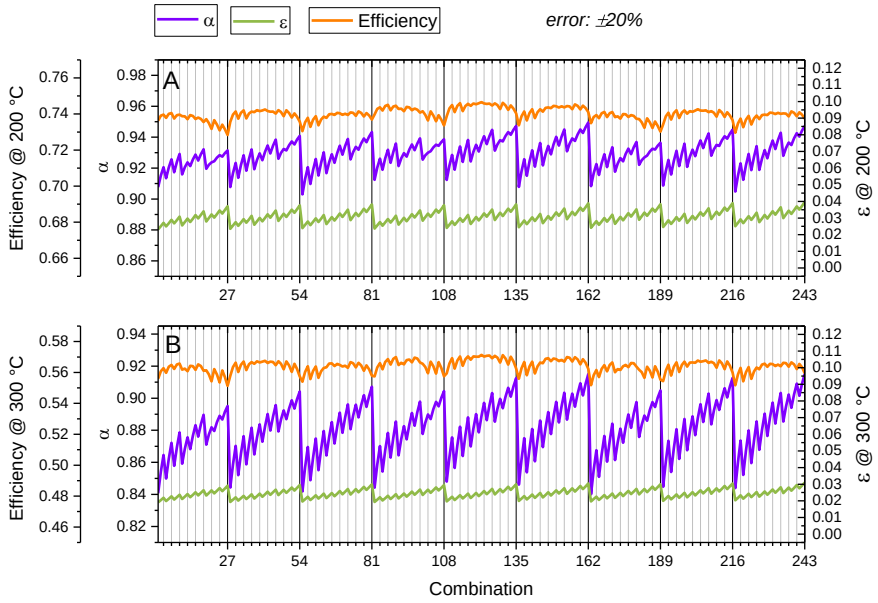

Fig. 5.7. Axis x: each ith combination identifies a different multilayer stack in terms of thickness, obtained by varying the thickness of each layer around its optimal value, in the case of three possible values for each layer and error = ± 20%. Axis y: solar absorptance α_S (left y axis, purple), efficiency (left y axis, orange) and thermal emittance ε(T) (right y axis) for the ith combination at the target optimization temperature, for the coatings OPT_200 and OPT_300 (panel A and B respectively).

5.1.5.2 Experimental results

To validate the numerical simulations and the optimization process, coatings OPT_200, and OPT_300 were experimentally realized via sputtering deposition. After the deposition, the multilayer thickness was measured with a profilometer (KLA Tencor P-15) determining that the thickness of the multilayer agreed with the sum of the expected single-layer thicknesses.

Figures 5.8 a and b show the measured reflectance spectrum and the related thermal emittance of the deposited samples in comparison with the simulated reflection spectra.

Solar absorptance values α and thermal emittance at different temperatures in comparison with the numerical counterparts for the two coatings are listed in table (5.3). Measured samples almost perfectly match the simulated results. These results confirm the correct evaluation of the experimental refractive indices used for the optimization.

The presented data have been calculated for normal incident radiation; when including the angular dependence, the absorptance and emittance could be different. However, the absorptance reported in table 5.3 was measured using an integrating sphere and results are only slightly different from the normal incident value indicating a small angular dependence. The emittance values were measured using a FTIR specular reflectance accessory and the hemispherical emittance could be

slightly higher than the reported value and it will subject to further investigation. Table (5.4) lists the coating efficiency (Eq. (5.3)) at the target optimization temperature for the three proposed selective absorbers, together with the related percentage deviation and the difference $\Delta\eta_{coat}$. Despite the variations in α_S and $\varepsilon(T)$ $|\Delta\eta_{coat}|\leq 0.02$ is still guaranteed, in accordance with the constraints imposed in optimization process.

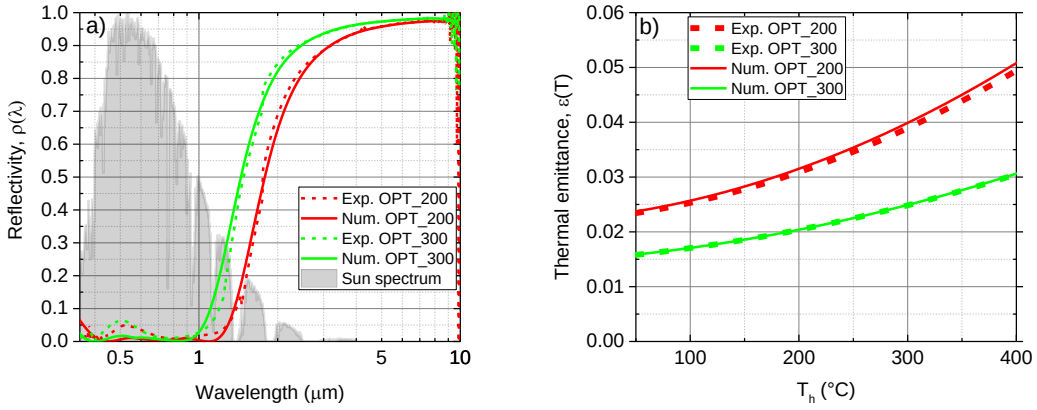

Fig. 5.8. a) Measured reflectance spectrum of the deposited samples OPT_200, OPT_300 (red, green dash lines) in comparison with the simulated reflection spectra (red, green solid lines). Normalized sun spectrum, grey filled area. b) Thermal emittance of the deposited samples OPT_200, OPT_300 (red, green dash lines) in comparison with the simulated thermal emittance (red, green solid lines).

Table 5.3. Solar absorptance values α and thermal emittance at different temperatures in comparison with the numerical counterparts for the two coatings

Sample	T opt. (°C)	α Num.	α Exp.	ε Num. (100 °C)	ε Exp. (100 °C)	ε Num. (200 °C)	ε Exp. (200 °C)	ε Num. (300 °C)	ε Exp. (300 °C)
OPT_200	200	0.936	0.925	0.026	0.025	0.031	0.031	0.040	0.039
OPT_300	300	0.889	0.890	0.017	0.017	0.020	0.020	0.025	0.025

Table 5.4. Coating efficiency η_{coat} at the target optimisation temperature for the two proposed selective absorbers, related percentage deviation and the difference $\Delta\eta_{coat}$

Sample	T opt. (°C)	$\eta_{coat\ Num.}$	$\eta_{coat\ Exp.}$	Deviation %	$\Delta\eta_{coat.}$
OPT_200	**200**	0.866	0.847	2.2	0.02
OPT_300	**300**	0.753	0.746	1.0	0.01

Using the optical measurements of the fabricated samples, along with Eqs. (5.3), the performance of the experimental coating was estimated. The coating efficiency calculated at 1000 W/m^2 using the experimental emissivity curves are shown in Fig. 5.9 and compared with the efficiency calculated under the same conditions using the emissivity curve from the optical simulations. The figure shows a remarkable match between the experimentally realised coatings and their simulated counterparts, confirming the feasibility of the coatings and their applicability in the medium-

temperature range. Moreover, the comparison between the optimized coatings efficiency and the commercial coating shows an improvement of 7.4% at 200 °C for both coatings and of 21.6% and 26.3% at 300 °C for the OPT_200 and OPT_300 respectively.

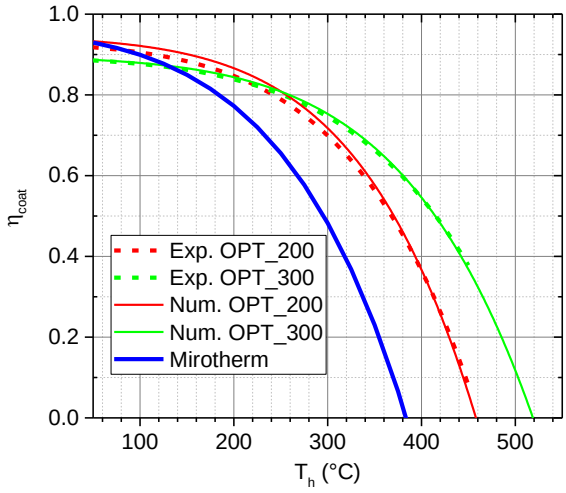

Fig. 5.9. Coating efficiency of the experimental samples OPT_200, OPT_300 (red, green dash lines) in comparison with the optical simulations (red, green solid lines) and of the commercial coating (blue line).

5.2 Substrate thermal radiative losses reduction

As discussed, the performances of a solar absorber for high vacuum insulated flat collectors would benefit from a substrate thermal emittance reduction, that could be obtained with a better finishing of the back side of the substrate or using a substrate with a low thermal emittance (such as copper or silver). To better understand how the thermal emittance affects the performance of a solar absorber let us recall Equation 3.13, which defines the overall efficiency of a selective coating. The negative terms in the equation are defined as the radiation losses and they are responsible for the system efficiency reduction at medium-high temperatures. By reducing the thermal emittance term $\varepsilon(T)$ of the SSA its performance will be significantly increased. For relatively high emissive substrates (section 3.5), a simple and relatively cheap way to significantly reduce the emissivity of both the selective coating side and the substrate side of a solar absorber could be a low emissive thin film coating could be used increasing the performances.

For example, Mirotherm® from Alanod [98], which currently powers TVP Solar collectors, uses aluminum as a substrate. Russo et al. [65,91] showed how $\varepsilon_{Sub} = 0.045$ is the value for the thermal emittance of the aluminum that best fits the experimental results for Mirotherm® commercial coating. A simple yet effective way to enhance the performances of this solar absorber could be to deposit a low emissivity coating such as a copper or silver coating (thermal emittance ≈ 0.02) on the back side of the absorber, on the aluminum surface, as shown in Figure 5.10.

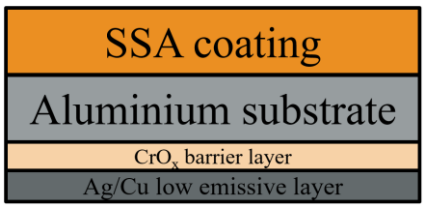

Figure 5.10. Solar absorber with a low emissivity coating on the back side of the aluminum substrate. A titanium bonding layer is used to guarantee the adhesion of the coating.

5.2.1 Materials and architectures

To study the effect of a low emissivity coating (LEC), several architectures were realized (fig. 5.11), titanium layer (10 nm) was used as bonding layer for all the architecture but is omitted in fig. 5.11. Silver (Ag) and copper (Cu) were chosen as low emissive materials, they were deposited using e-beam vapor deposition on an aluminum bulk substrate. The LEC was deposited on one side (architecture 1 and 2) or on both sides (architecture 3 - 4 - 5) of the aluminum substrate, the thickness of each LEC is 200 nm. Moreover, on architecture 5 also a Cr_2O_3 layer was deposited between the substrate and LEC, this layer acts as diffusion barrier (DB) layer, to prevent degradation due to high temperature.

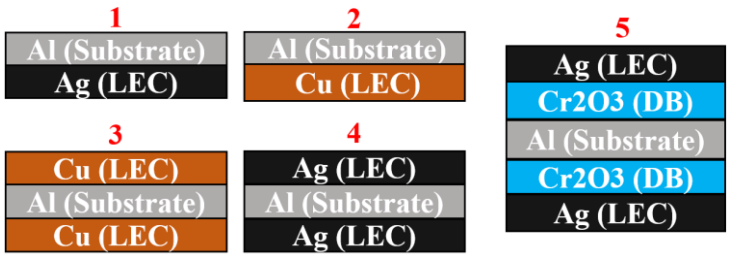

Figure 5.11. Low emissive coating architectures: 1-2) one side LEC Ag and Cu respectively, 3-4) both sides LEC Cu and Ag respectively, 5) both sides Ag LEC with Cr_2O_3 diffusion barrier.

Additionally, to prove the LEC thermal stability a 200 nm-thick layer of Ag was electron-beam deposited on the backside of a 15x15 cm^2 commercial SSA (Mirotherm®), with and without the presence of a Cr_2O_3 DB layer (fig. 5.12). The two samples were thermal stressed for 24 hours at 360 °C in the MTB apparatus, and the thermal emittance measurements before and after the treatment were performed.

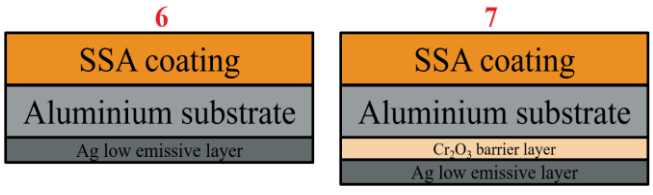

Figure 5.12. Silver LEC on the back side of a commercial Selective Solar Absorber without (6) and with (7) a Cr_2O_3 diffusion barrier layer.

5.2.2 Samples preparation and deposition techniques

The electron-beam vapor deposition technique was employed for the fabrication of samples in fig. 5.11. The evaporation of Ag, Cu and Cr_2O_3 was performed at a vacuum pressure of $4 \cdot 10^{-5}$ Pa and with a deposition rate of 1.5 $Å s^{-1}$ on the aluminum substrates cleaned with acetone and isopropyl alcohol. The uniformity of the layers deposited on the substrates was guaranteed by placing the samples on a rotating planetary. The deposition rate is controlled by a Quartz Crystal Microbalance (QCM) [113] accurately settled with density and Z-ratio of Ag, Cu and Cr_2O_3. The QCM deposition rate reading was adjusted to the deposition rate on the samples thanks to a carefully calibration of the tooling factor. The tooling factor was experimentally adjusted by depositing single layers of Ag, Cu and Cr_2O_3 and measuring their thicknesses through a profilometer (KLA Tencor P-15).

5.2.3 Experimental results

The actual thermal emittance from low temperatures up to stagnation temperature are measured using a calorimetric instrument well described in [88] (see also section 4.3), based on the power balance equation defined in the following equation:

$$m\, c_p \frac{dT_a}{dt} = \alpha\, A\, P_{in} - radiation\ losses \qquad (5.3)$$

being m, c_p, T_a, α and A the mass, specific heat, temperature, spectrally averaged absorptivity, and area of the absorber, and P_{in} the incident power density. Figure 5.13 shows the aluminum bulk substrate before and after being copper coated.

Thermal emittance reduction with LECs

Figure 5.14 shows the results of the calorimetric measurements for a bulk aluminum substrate and for the 5 different architectures of fig. 5.11.

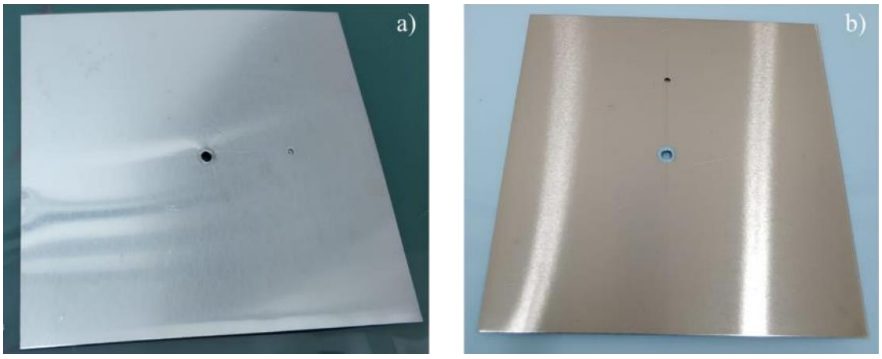

Figure 5.13. Aluminum bulk substrate before (a) and after (b) copper coating via e-beam PVD.

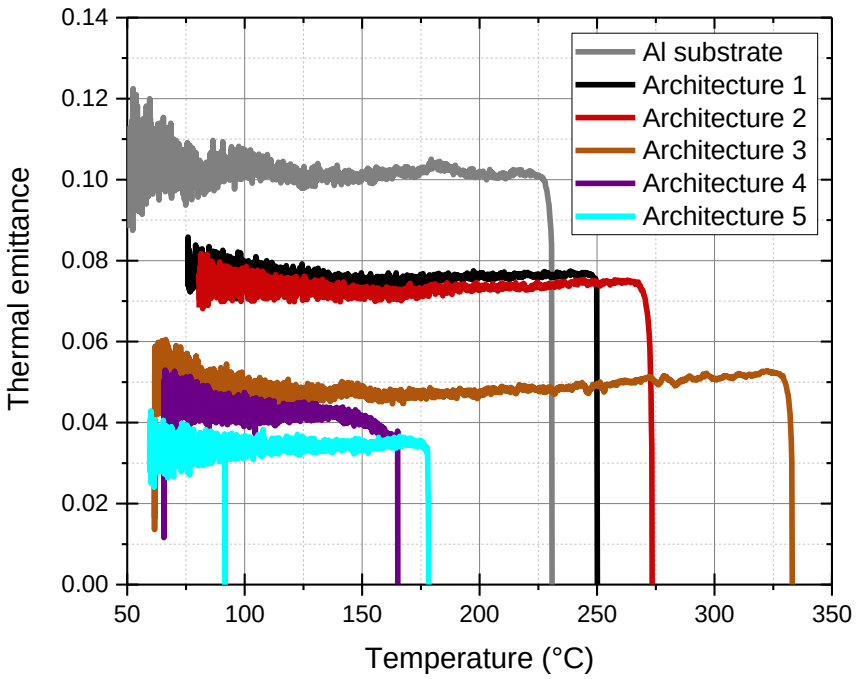

Figure 5.14. Thermal emittance calorimetric measurements of aluminum bulk substrate (grey line) and architectures 1 - 2 - 3 - 4 – 5 (black, red, brown, violet, and cyan respectively).

Figure 5.14 shows the thermal emittance ($\varepsilon_{sample}(T_a)$) results obtained during the cooling down phase of a colorimetric measurement as described in section 4.3. The $\varepsilon_{sample}(T_a)$ refers to the sum of the thermal emittance of both side of the measured sample, in the case of bulk aluminum (grey line) we have an almost constant value (0.10) on all the measured temperature range. This value is exactly doubled the aluminum thermal emittance literature data [78] (table 3.1, section 3.5). A 25% thermal emittance reduction can be observed for the one side coated samples (architecture 1 and 2), while a 50% reduction can be observed for the double side Cu coated sample (architecture 3). The best result is obtained with the double side Ag coated samples (architectures 4 – 5), with a thermal emittance reduction of 60-65%.

LECs thermal stability

Figure 5.15 demonstrate the impact of the Ag LEC on the thermal emittance of a commercial SSA and the role of the Cr_2O_3 diffusion barrier (DB) layer on the thermal stability of LECs. The thermal emittance of the commercial SSA (as produced), the architecture 6 (fig. 5.12) and the architecture 7 (fig. 5.12) (black, blue, and green line respectively) are shown. Both sample with the LEC exhibit an 11% reduction in thermal emittance at 200 °C compared with the commercial SSA as produced.

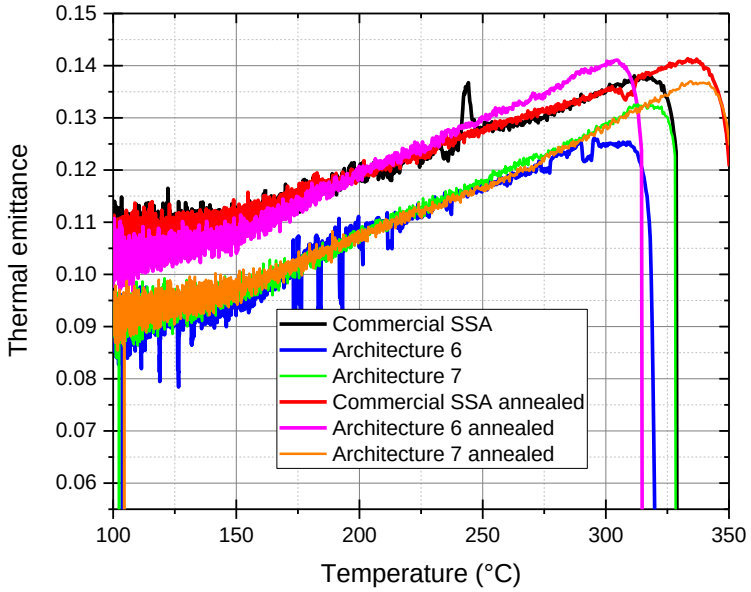

Figure 5.15. Thermal emittance calorimetric measurements of commercial SSA, architecture 6 and 7 before (black, blue, and green line respectively) and after (red, magenta, and orange respectively) thermal treatment.

To demonstrate the thermal stability of the LECs, these samples were thermally stressed for 24 hours at 360 °C in vacuum environment. The thermal emittance after the annealing process is shown in fig. 5.15. The commercial SSA (as produced) is thermally stable, because the thermal emittance after the thermal treatment (red line) is the same compared to the untested commercial SSA. The architecture 6 showed an increase in thermal emittance after the thermal stress compared to the untested architecture 6, this emittance reaches the same value of the commercial SSA, losing all the advantages due to the LEC. Instead, the architecture 7 after the thermal treatment exhibited the same thermal emittance of the untested architecture 7, demonstrating the necessary to have a diffusion barrier to preserve the benefits of the LECs.

HVFPCs performance improvement analyze

The substrate thermal emittance ($\varepsilon_{sub}\ (T)$) reduction strongly affect the overall efficiency of a selective coating for HVFPCs as defined from equation 3.13, here reported:

$$\eta_{panel} = \alpha_s - \frac{\varepsilon_{abs}\ (T)\ \sigma_{SB}(T_{abs}^4 - T_{amb}^4)}{C \cdot G_{Sun}} - \frac{\varepsilon_{sub}\ (T)\ \sigma_{SB}(T_{abs}^4 - T_{amb}^4)}{C \cdot G_{Sun}} \qquad (5.4)$$

The effects of a LEC on the η_{panel} are reported in figure 5.16. The overall efficiency of an optimized selective coating on aluminum substrate without (black line) and with diffusion barrier and low emissive coating (red line) are reported. The figure shows how at 200 °C efficiency of the absorber increases from 0.64 up to 0.72, with 13% enhancement in performances, and the stagnation

temperature increases of about 30 °C. It is worth to note that the advantages of the low emissive coating increase with increasing temperature, in fact at 300 °C the overall efficiency increase from 0.19 to 0.37, having an almost doubled enhancement in performances.

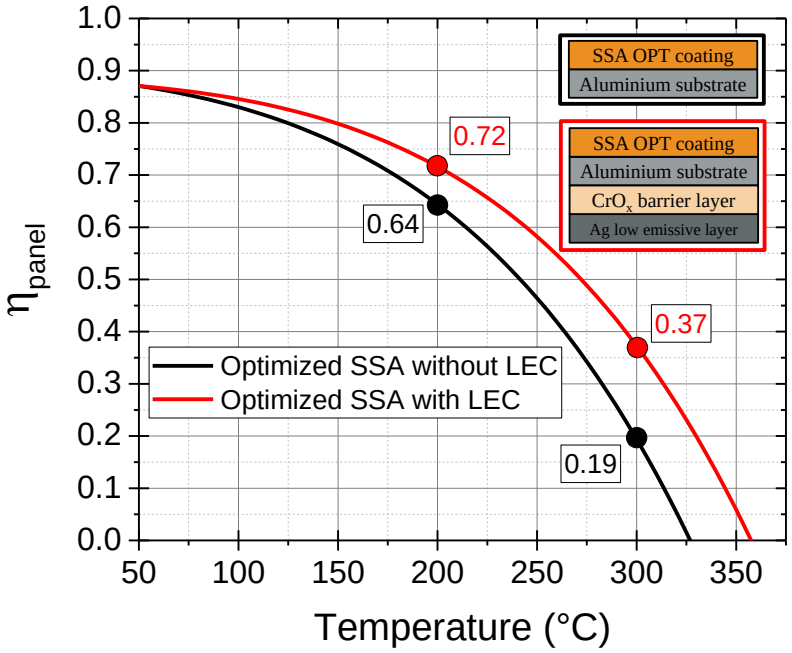

Figure 5.16. The overall efficiency of an optimized selective coating on aluminum substrate without (black line) and with diffusion barrier and low emissive coating (red line).

As discussed before (section 3.4), for multilayer coatings, the spectrally averaged emissivity is mainly due to the low-emissive metal substrate, so it makes sense to use a low emissive coating for the coating side of the absorber, too. This solution would allow to use cheap materials as a substrate as aluminum, while guaranteeing excellent optical properties of the absorber, using coatings of low emissive but more expensive materials at a negligible cost (see Table 3.1). At high temperatures however, interdiffusion between the low emissive thin film and the aluminum substrate may cause adhesion issues and a deterioration of the optical properties, so an interdiffusion barrier should be used to limit the diffusion phenomena.

6. High-Efficient Selective Emitter for Solar Thermophotovoltaic application

This chapter intends to provide a general overview of thermo-photovoltaic (TPV) systems, highlighting the key role of both high-vacuum insulation and selective emitters in the control of the thermal emissions and of the systems efficiency. The chapter is organized as follows: section 6.1 introduces the PhotoVoltaic (PV) cells operation, as it is the main component of a TPV system. The working principle of TPVs is described in detail in section 6.2. Section 6.3 presents the state of the art of the development of selective emitters, while section 6.4 reports the results of our approach in designing selective emitters.

6.1 PV cell operation

A photovoltaic (PV) cell, whose working principle is schematically shown in Fig. 6.1, is basically configured as a large-area p-n junction, i.e. n-type and p-type semiconductors put directly adjacent to each other to create a stronger carrier diffusion gradient. The mechanism that allows to convert solar energy into electricity is the photovoltaic effect: when the photons hit the cell, their energy is transferred to the electrons of an atom of the semiconducting material in the p-n junction, causing it to jump to a higher energy state (conduction band) and creating an electron-hole pair. Hence, these electrons are free to move through the material, and their motion towards the n-side of the junction creates an electric current in the cell, which is the key point of a working cell [114].

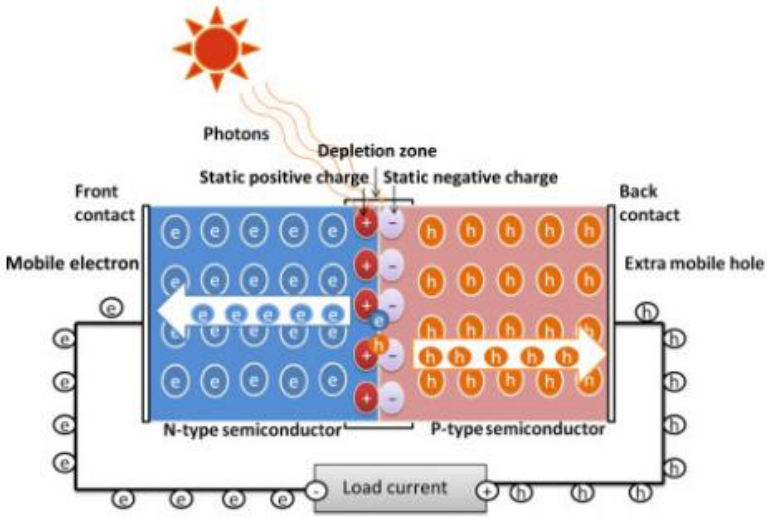

Figure 6.1. Working Principle of a PV Device. Image available in [115].

However, only photons with appropriate energy (equal to the bandgap energy, E_{bg}, of the semiconductor) participate to the process: photons with $E < E_{bg}$ are not able to create the electron-hole pair; photons with $E > E_{bg}$ can only create one electron-hole pair and their excess energy is dissipated as heat. Therefore, in both cases there is a loss of energy which limits the conversion

efficiency of the PV cell, determined as the fraction of incident power which is converted to electricity and is defined as:

$$\eta_{PV} = \frac{P_{el}}{P_{in}} \tag{6.1}$$

Hence, only a small part of the solar spectrum is useful for the conversion: for example, Fig. 6.2 shows that the available portion of the solar spectrum is reduced to the 33% in the case of a silicon solar cell, with E_{bg} = 1.1 eV.

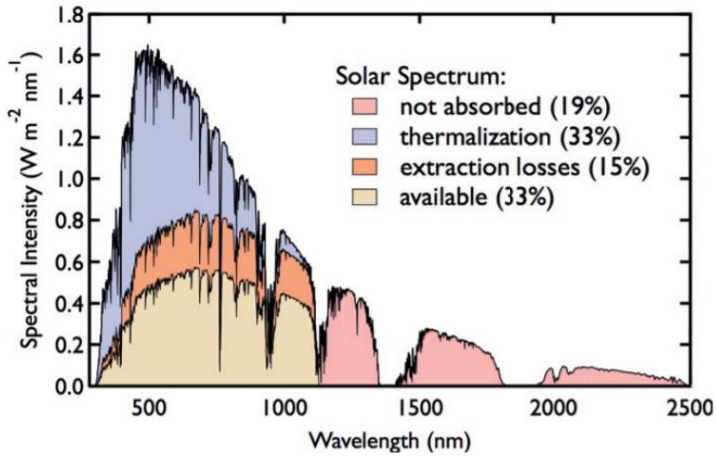

Figure 6.2. Spectral analysis of the minimum losses for a silicon solar cell (bandgap = 1.1 eV): thermalization represents the largest loss in this analysis, and it increases for the higher energy portions of the solar spectrum [116].

Besides silicon, other semiconductors can be used in solar technologies: the most diffuse are listed in table 6.1, where their bandgap energy and wavelength (E_{bg}, λ_{bg}) are reported. PV cells can be classified into four generations, depending on the materials which are used for their fabrication. They are illustrated in Fig. 6.3 [115]:

• **first-generation cells**, which include single- and multi-crystalline silicon;

• **second-generation cells**, which are based on thin films (the maximum film thickness was brought down to a few nanometers to tens of micrometers to reduce the high material usage and cost of the previous generation);

• **third-generation cells**, which include organic solar cells with nano-crystalline films;

• **fourth-generation cells**, which combine the low cost/flexibility of polymer thin films with inorganic nanostructures.

Table 6.1. Band-gap energy and wavelength of the semiconductors most used for PV cells. Note that the term perovskite indicates a class of compounds which have the same type of crystal structure as $CaTiO_3$, and the range of bandgap energies indicated in the table can be further extended. CIGS stands for Copper Indium Gallium Selenide.

Material	E_{bg} (eV)	λ_{bg} (μm)
GaInAsSb	0.53	2.34
Ge	0.66	1.88
GaSb	0.72	1.72
Si	1.12	1.11
GaAs	1.42	0.87
InGaSb	1.42 to 0.36	0.87 to 3.44
CdTe	1.45	0.86
CIGS	1.01 to 1.68	0.74 to 1.23
Perovskites	1.30 to 2.30	0.54 to 0.95
InGaP	1.90	0.65

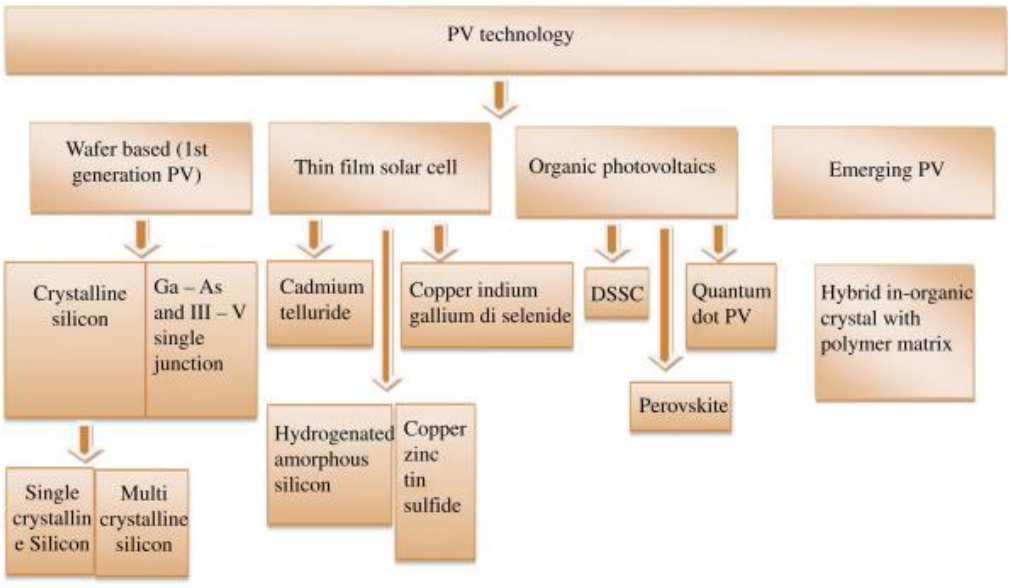

Figure 6.3. Schematic of the various generations of solar cells [115].

However, the most common solar cells available in the market are the first-generation solar cells: **Monocrystalline silicon solar cells** which are made up of crystals grown along one plane from cylindrical shaped ingots which are sliced into small wafers. Impurity atoms are added to dope the silicon either to make it p-type or n-type. The high purity determines high costs but high efficiency (26.7% [117]).

Polycrystalline silicon solar cells which are made from raw silicon, melted and poured into a square mold, further cooled and cut into perfectly square wafers. Therefore, the low purity and nonuniformity of the wafers determines a lower efficiency, which reach its maximum around the 24.4% [117].

6.2 The interest in TPV technologies

The recent growth of photovoltaic solar energy capacity worldwide, as well as the relatively high collection efficiency of solar thermal collectors, have brought the attention of many on the development of thermo-photovoltaic systems. A TPV system employs a PV module and a thermal collector and allows the direct conversion from the thermal radiation emitted from an object heated at temperatures typically higher than 1000 K to electricity.

As a result of the PV cell operation (described in the prior section), it is crucial that the radiation incident on the PV cell matches its bandgap. Hence, the key role of the thermal emitter, a device which emits thermal radiation and for which selectivity is required: it must emit only the photons with energy included in the range of interest to make the PV cell work properly. Alternatively, a filter can be added in front of the PV cell to transmit only the photons with $E = \hbar\,\omega \simeq E_{bg}$, while the remaining photons with energy outside the range of energies admitted by the PV cell are reflected back and reabsorbed by the emitter. The filters are particularly useful when working with black body emitters or emitters not perfectly selective, but they mostly reflect a small percentage of light in the desired wavelengths range. Then, all the light that is not redirected to the emitter or to the PV cell is lost.

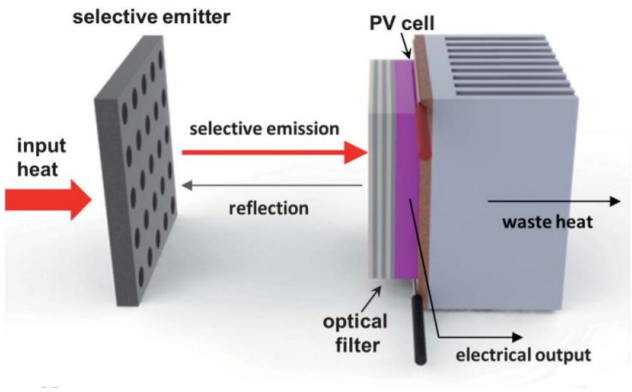

Figure 6.4. Schematic of TVP operation. Image available in [118].

The working principle of a TPV device is schematically illustrated in Fig. 6.4 and could be summarized as follows [23]: the thermal energy coming from any source heats up an emitter, which emits photons preferably with energy above the bandgap of the PV cell. At this point, the radiation emitted hits the PV cell and is converted into electricity.

Despite their design is complex, TPV systems have several advantages besides directly converting heat radiation into electricity: they are modular and lightweight, which means that existing systems can be expanded or adapted to the needs; their average lifetime is of 25 years; they require little maintenance, are silent and emission free [114]. The main advantage of TPV with respect to direct conversion by solar cells is that their spectral distribution can be tailored according to their sensitivity, thanks to the either the selectivity of the emitter and the filter. It also has a potentially higher efficiency and higher power densities (5-60 W/cm^2 compared with 0.1 W/cm^2 for solar cells), as the heat source and the PV cell are much closer in TPV compared to the distance from the Sun (1-10 cm Vs $\simeq 1.5 \cdot 10^{10}$ m). However, the definition of efficiency in TPV systems is complex and strongly depends on the boundary conditions: the total input can be defined in different ways depending on the heat source, and the output could be either considered as exclusively electrical or electrical and thermal - in the case of Combined Heat and Power (CHP) systems. Fig. 6.5 illustrates a schematic of the energy flow of a general TPV system.

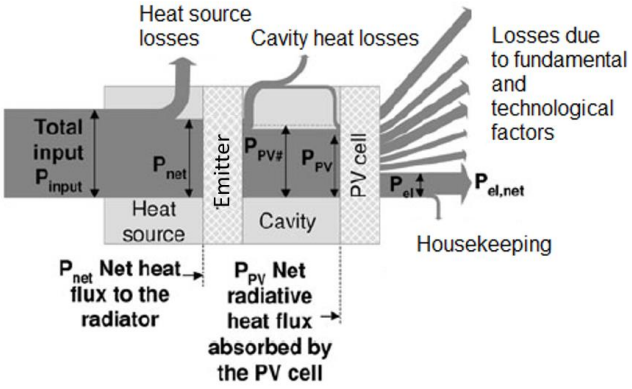

Figure 6.5. Energy flow of a TPV system (adapted from [23]*).*

Therefore, the overall efficiency of a TPV system, η_{TPV}, depends on the product of all partial efficiencies of the various part of the system [23], namely:

• η_{PV} is the PV cell efficiency, defined in Eq. 6.1;

• η_{source} is the heat source efficiency, defined as the ratio of emitter net heat transfer to the total input:

$$\eta_{source} = \frac{P_{net}}{P_{in}} \tag{6.2}$$

• η_{cavity} is the cavity efficiency, which in steady state is defined as ratio of the power incident on the PV cell to the net radiative heat flow:

$$\eta_{cavity} = \frac{P_{PV}}{P_{net}} \tag{6.3}$$

The current estimate of the capital costs for PVT systems shows that it is approximately 30% higher than the cost of a PV and solar thermal system installed side by side, and the PVT collectors account for approximately the 60% of the total cost [119,120]. But, as the cost of solar thermal systems is decreasing with a learning curve of 20% in Europe, similar to the decreasing production cost of crystalline silicon (c-Si) PV modules [121,122], it would be not too risky to assume that a reduction of costs will also invest the TPV market. A first step in that direction certainly could be the development of innovative designs which increase the thermal efficiency and improve the cost-competitiveness of the system. About this, a recent work [123] has proposed new high efficiency designs which reduced the emissivity of the solar cells in flat plate and evacuated TPVs. Those employs an evacuated glazing cavity combined with a low emissive coating (with and emissivity of $\varepsilon = 0.15$). Compared to present commercial TPVs, this collector is projected to have double the thermal efficiency, and to provide 1.5 and 2 times the revenue or carbon savings of PV modules and solar thermal collectors, respectively [123]. Hence, the need to exploit the advantages of high vacuum insulation, already illustrated in the section 2.4 (Fig. 2.12). Potentially, TPV systems can convert heat into electricity with Carnot efficiency. Hovewer, at the current stage of research, the highest estimation of efficiency for TPV systems working at 1300 K reaches the 70% of the Carnot's limit [124] if a selective emitter built from refractory metals is employed. It is therefore obvious that in such systems the control of thermal radiation through selective emitters becomes fundamental to reduce the amount of wasted heat. In the next two sections we present the state of the art and propose new and easier designs of selective emitters.

6.3 Selective emitters: state of the art

We have learned that the interest in the control of thermal emissions in the IR range represents a crucial factor in reaching higher efficiency in various energy systems (as well as in other fields, involving applications like thermography [125], radiative cooling [126,127], IR spectroscopy [128,129], etc.). Emitters and their properties play a crucial role in that issue.

The ideal thermal emitter is a selective emitter (SE), characterized by a sharp transition from high- to low-emissivity. Considering the TPV systems operation, the transition has to happen in the position of the spectrum corresponding to a photon energy approximately equal to the bandgap energy of the associated PV cell. Depending on their characteristics, they can be classified in broadband emitters and narrow-band emitters. Broadband emitters are characterized by an emissivity curve which is spectrally close to 1, leading to emission of photons across wide range of wavelengths. Silicon carbide (SiC) is for example one of the most used materials for this application, as it determines an emissivity of approximately 0.9 over a large region of the spectrum. Their main advantages are the simplicity of fabrication and high durability [130], however their broad emission spectrum causes existing systems to have low efficiencies when applied to TPV

systems, since the wavelength range of PV cells conversion is very small compared to the emitter spectral range. Therefore, to prevent unnecessary absorption of above-band gap photons and avoid losses, it is crucial to work on the properties of the emitter to obtain narrow-band emitters. In this case, the emitted photons should have energies slightly above the PV cell bandgap. Typically, broadband emitters yield higher output electrical power density while narrow-band emitters can increase the TPV conversion efficiency. The ideal spectral control of both broadband and narrow-band emitters is shown in Fig. 6.6 a), while Fig. 6.6 b) highlights the fraction of high-energy photons convertible into electricity in a GaInAsSb cell.

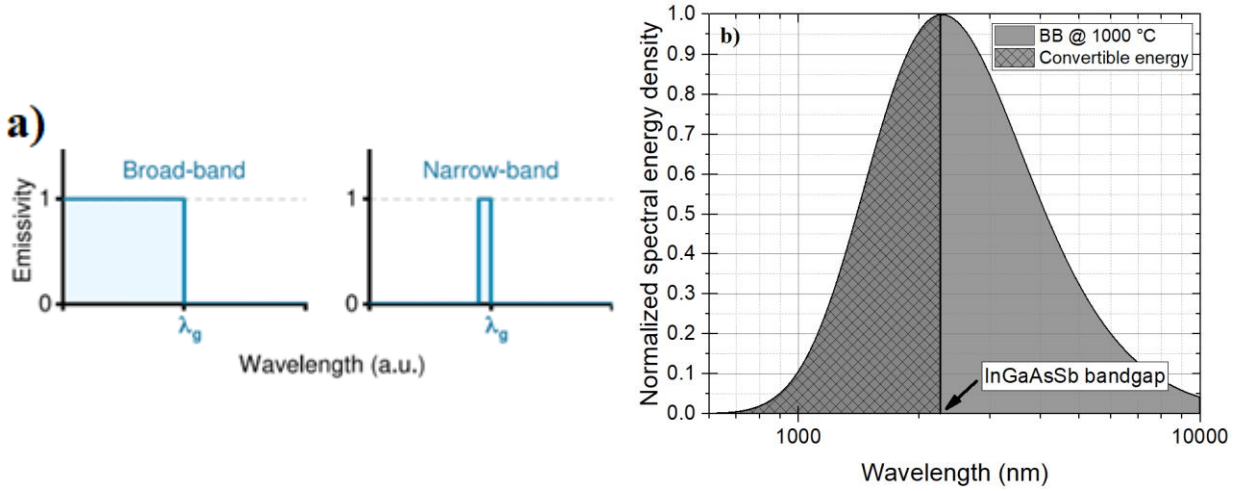

Figure 6.6: a) Ideal spectral control of a broadband thermal emitter, where any in-band photons are preferentially emitted, and of a narrow-band emitter, where only photons with energy slightly above the bandgap are emitted. b) Blackbody emission at 1000 °C, where the fraction of high-energy photons convertible into electricity in a GaInAsSb cell is highlighted (grey area with pattern). Adapted from [131].

Several solutions of SE have been already developed in the past. They are based on different designs, each having advantages and disadvantages:

• **bulk emitters**, which can be either graybody emitters [27] such as Si, SiC, or metals with [28] or without AR coatings [29]. Both are typically inexpensive and easy to fabricate in large areas.

• **naturally selective emitters** [30], made from rare earth metals like erbium and ytterbium. They are easy to fabricate and thermally stable at high temperatures, but their emission is not tunable.

• **metamaterials** [31], they consist in engineered material made of periodic patterns that are smaller than the wavelength of interest and can produce or behave with characteristics that are not found in nature.

• **1D photonic crystals** [32,132,133], which consists of alternating layers of high and low-index materials. They can cause high emissions outside the region of interest.

• **2D photonic crystals** [33], they consist of 2D array of features on top of or in a substrate: whether an emitter can be fabricated inexpensively with large area depends on the substrate.

Nevertheless, although some have very favorable characteristics, they all have in common two main disadvantages: high cost and complexity of fabrication, especially when considering that they need to be industrialized. Therefore, in the next section we propose simpler structures based on easy-to-fabricate multilayers which can be extended to an industrial manufacturing. Multilayers basically consist of alternating metal and dielectric layers of varying thicknesses. The layer thicknesses can be optimized to enable broadband or tight emissions. The main advantages are the good performance, the low fabrication cost, and the ability to fabricate in large scale. The only drawback could be that, in the long run, the materials at the interfaces may intermix. Therefore, the materials must be chosen carefully and the absence of interdiffusion experimentally verified.

6.4 Design and realization of multilayer-based selective emitter

In this section we define the steps towards the complete design and realization of nearly ideal selective emitter (SE) based on multilayer design. The emitter (figure 6.7) was realized on Tungsten (W) Polycrystalline Substrate, 25.4 x 25.4 x 0.5 mm two sides polished, provided by MTI Corporation. The chose structure results to be very simple (three layer) and without the presence of metallic layers, in order to reduce the oxidation issues that could occur during high temperature applications [134]. The selected materials are: SiN_x, SiO_2 and TiO_2. These materials were chosen because of their high melting point (higher than 1700 °C), their similar thermal expansion coefficient [135–138] and their common usage for emitter applications.

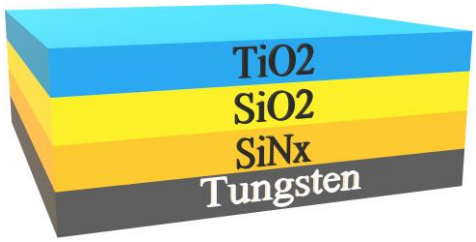

Figure 6.7. Architecture of the Selective Emitter

A way to evaluate the efficient behavior of a SE is to calculate the emitter efficiency (η_{emi}) hypothesizing that all emitted photons with energies above the bandgap of the PV cell are absorbed and provide electric energy equal to the bandgap energy (called 'ultimate efficiency' in [139]). In this case the PV cell generated electric power ($P_{out\ ideal}$) is defined as:

$$P_{out\ ideal} = \int_0^{\lambda_g} \frac{\lambda}{\lambda_g}\, \varepsilon(\lambda)\, I_{BB}(\lambda, T_{emitter})\, d\lambda \qquad (6.4)$$

where λ are the wavelength, λ_g is the bandgap wavelength, $\varepsilon(\lambda)$ is the spectral emissivity of the SE, $I_{BB}(\lambda, T_{emitter})$ is the blackbody spectral power density at the emitter temperature. The ratio of the generated electric power to the emitter emitted power is the η_{emi}:

$$\eta_{emi} = \frac{P_{out\ ideal}}{P_{emi}} \tag{6.5}$$

where P_{emi} is the emitter emitted power defined as:

$$P_{emi} = \int_0^\infty P_{emi}(\lambda)d\lambda$$

$$P_{emi}(\lambda) = \varepsilon(\lambda) I_{BB}(\lambda, T_{emitter}) \tag{6.6}$$

The thickness of each layer was obtained thanks to a Genetic Algorithm developed on MATLAB®. This algorithm can automatically change the thickness of each layer and calculate the reflectivity ρ(λ) of the stack at each wavelength (section 5.1.4). The reflectivity is computed according to the transfer matrix method [110] utilizing the experimental refractive indices at room temperature (section 6.4.3.1). The algorithm also considers the angle of incidence dependence (0-10-20-30-40°) of the reflectivity. With this information it is possible to calculate the η_{emi} for each angle of incidence and the averaged η_{emi} was used as fitness function (maximization). To optimize the multilayer structure the algorithm also needs to know the PV cells bandgap and the emitter working temperature. The temperature chosen is the upper limit of the heating stage used for ellipsometric measurements (1000 °C), while for the bandgap was chosen a variable range (0.55 - 0.72 eV) in order to obtain a structure able to work with the III-V semiconductors region, mainly used as PV cells for STPV systems. The obtained thickness are 77 nm, 324 nm and 247 nm for SiN_x, SiO_2 and TiO_2 respectively.

6.4.1 Deposition techniques

The multilayer stack was deposited through PVD Sputtering System - Metal/Dielectric Sources, the targets have a circular shape with a diameter of 5.08 cm and the distance between the sample and target is 10 cm. The system is equipped with four different targets and a rotating sample holder, in order to improve the uniformity of the deposition on the substrates. The RF magnetron sputtering (RFMS) and RF reactive magnetron sputtering (RFRMS) technique were used, regulating the output power. High purity Si, SiO_2 and TiO_2 targets (99.99%) have been utilized for the deposition of the thin films. Argon was employed as a sputtering gas and Nitrogen as a reactive gas. The deposition parameters are listed in Table 6.2.

Table 6.2. PVD Sputtering System deposition parameters

Layer	Target	PVD	Base pressure (Pa)	Argon flow (sccm)	Nitrogen flow (sccm)	Power (W)	Deposition rate (nm/min)
SiN_x	Si	RFRMS	$6.67x10^{-5}$	14.5	0.5	100	3.07
SiO_2	SiO_2	RFMS	$6.67x10^{-5}$	15.0	0.0	100	1.65
TiO_2	TiO_2	RFMS	$6.67x10^{-5}$	15.0	0.0	100	1.35

The deposition rates were obtained performing single layer deposition for each material on photo-resist material at the same deposition conditions listed above. The thickness was measured with KLA-Tencor P-10 Profilometer from several step height measurements averaged.

6.4.2 Optical characterization

The spectral reflectivity of the experimental sample was measured through a traditional dual-beam spectrophotometer equipped with integrating sphere (PerkinElmer Lambda950) in the range 300-2000 nm. Spectralon® WS-1-SL diffuse reflectance standard from Labsphere (99% reflectivity in the range 400-1500 nm; > 96% in the range 250-2000 nm) was used as reference reflectance standard.

Thermo Fisher Nicolet 670 was utilized for NIR to FIR reflectivity measurements (1700-10000 nm), with gold mirror used as reference reflectance standard.

J.A. Woollam RC2 Spectroscopic Ellipsometer was employed to evaluate the refractive indices of the material composing the multilayer in the range 500-2500 nm. The same tool equipped with Linkam TSEL 1000 Vertical Heat Cell was used for in temperature ellipsometric measurements.

6.4.3 Experimental results

6.4.3.1 Refractive indices: room temperature

The refractive indices used for the optimization of the multilayer have been experimentally determined via ellipsometric analysis at room temperature for SiN_x, SiO_2 and TiO_2 layer. The ellipsometric measurements were also performed on the plain Tungsten Polycrystalline Substrate, in order to include this material as an optical infinite layer in the optimization. Tauc-Lorents model was used to fit experimental data for SiN_x and TiO_2, while Cauchy transparent model was adopted for SiO_2, the W was modelled with 6 Lorentz oscillators. The refractive indices obtained are reported in figure 6.8 (solid lines) compared with literature data (dashed lines) [106,140–142].

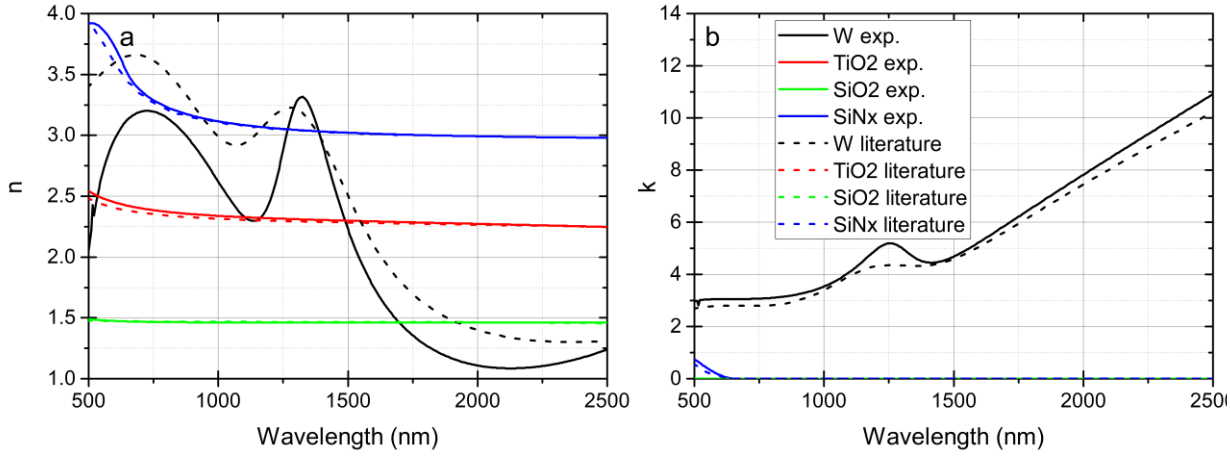

Figure 6.8. Experimental (solid lines) and literature (dashed lines) refractive indices (a) and extinction coefficient (b) for W (black lines), TiO_2 (red lines), SiO_2 (green lines) and SiN_x (blue lines).

The comparison shows an agreement between experimental and literature data for all the materials. The thicknesses, ellipsometric measured, are within 4% of the expected from deposition rates. The refractive indices data for higher wavelength (from 2500 to 10000 nm) were extrapolated according to the trend of the literature data.

6.4.3.2 Experimental verification

The emitter was fabricated on a polished W substrate (0.5 mm thickness) and the emissivity (ε(λ)) measured values (reported in figure 6.9) were obtained from reflectivity measurements as: $\alpha(\lambda) = 1 - \rho(\lambda) - \tau(\lambda)$, where α(λ), ρ(λ) and τ (λ) are the spectral absorptivity, reflectivity and transmissivity of the multilayer structure respectively, and τ (λ) is 0 because of opaque surface. Moreover, according to Kirchhoff 's law of thermal radiation [111,112] the emissivity (ε(λ)) of a hot radiating body equals its absorptivity (α(λ)). Therefore, we can evaluate the spectral emissivity by measuring the absorptivity of our multilayer structure. At room temperature, the measured emissivity (ε(λ) as dep., black line) of the deposited SE results to be similar to the simulated optimized emissivity (ε(λ) simulated, red dash-dot line) computed by the optimization algorithm (figure 6.9a).

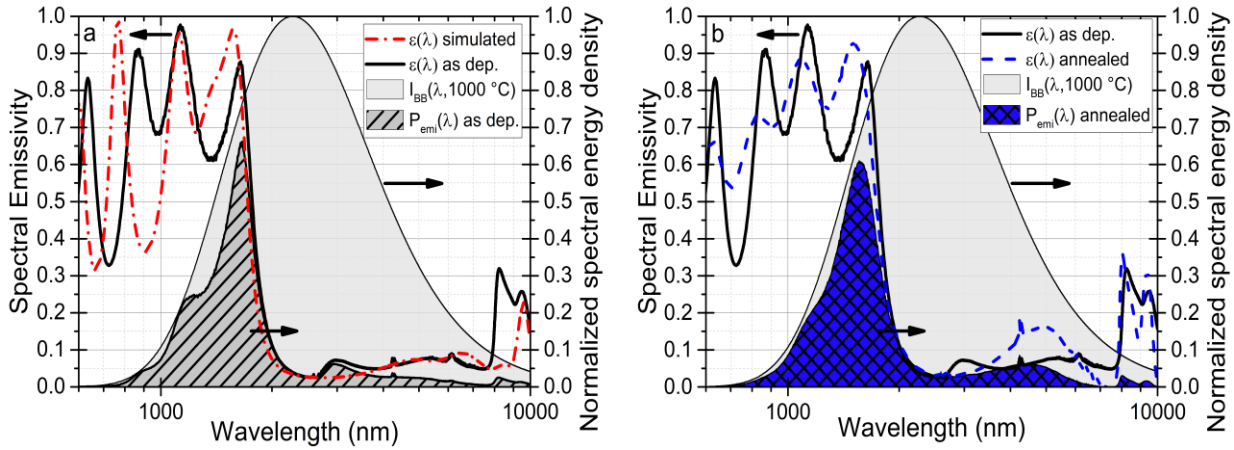

Figure 6.9. a) Left axis: as deposited (black line) and simulated optimized (dash-dotted red line) spectral emissivity of the Selective emitter; Right axis: normalized spectral energy density of blackbody at 1000 °C and of the as deposited emitter (grey area and dark grey area with pattern respectively); b) Left axis: as deposited (black line) and after annealing process (8 hours at 1000 °C) (dash blue line) spectral emissivity of the Selective emitter; Right axis: normalized spectral energy density of blackbody at 1000 °C and of the annealed emitter (grey area and blue area with pattern respectively).

The deposited SE shows high emissivity values mainly after 1000 nm where the normalized spectral energy density of the blackbody at 1000 °C (grey area) exceed 0.1. The two main measured peak values are 0.98 and 0.88 at 1130 nm and 1645 nm respectively, and they are similar to the expected optimized values (0.96 and 0.97 at 1120 nm and 1570 nm respectively). The emissivity values drop down to values lower than 0.1 at 2000 nm and they remain lower than 0.1 till about 8000 nm where the normalized spectral energy density of the blackbody at 1000 °C is lower than

0.1. This emitter behavior aims to have a spectral energy density of the as deposited sample mainly concentrated before the highest PV cell bandgap considered (0.72 eV or 1722 nm), while the $P_{emi}(\lambda)$ emitted after this bandgap is reduced to low values (dark grey area with pattern). The fast transition from high to low emissivity values, guarantee a high emitter efficiency in all the bandgap range considered. To better understand the SE functioning of the optimized and as deposited sample, the emitter efficiency as a function of the PV cell bandgap (E_g) and SE emitter working temperature was plotted in fig. 6.10. The optimized structure (figure 6.10a) shows a high emitter efficiency in all the optimized bandgap range at 1000 °C. The maximum value of 0.54 is reached at 0.66 eV, while 0.50 and 0.51 are the values at the bandgap range limits (0.55 and 0.72 eV respectively). A maximum difference of 4% is obtained all over the bandgap range, demonstrating the possibility of this structure to work with several different PV cells. The correct behavior is also preserved for higher working temperature showing a versatility also with temperature.

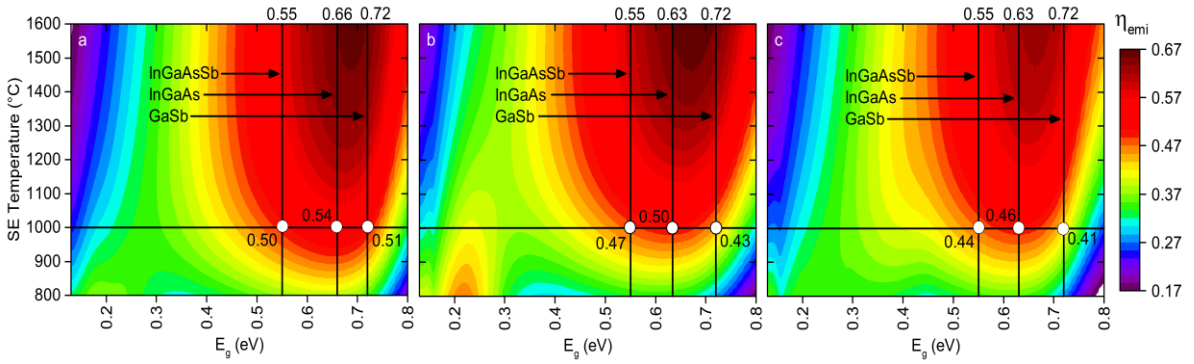

Figure 6.10. Calculated emitter efficiency of the optimized (a), as deposited (b) and annealed (c) selective emitter as a function of temperature versus PV cell bandgap energy.

An emitter efficiency loss is observed for the as deposited sample (figure 6.10b), where the maximum value at 1000 °C of 0.50 is reached at 0.63 eV, while 0.47 and 0.43 are the values at the bandgap range limits. In this case a maximum difference of 7% is noticed all over the bandgap range, but the structure preserves significant emitter efficiency values.
In order to understand if this multilayer structure can actually work at high temperatures, the emissivity measurements were also performed after a long thermal stress (figure 6.9b). The long thermal stress was performed in the high vacuum Centorr Testorr™ furnace at $8x10^{-3}$ Pa, the sample was kept at 1000 °C for 8 hours. The emitter behaviour after thermal treatments, measured at room temperature, shows similar characteristics to the as deposited with even a slight improvement of the spectral characteristics, e.g. an higher emissivity peak value around 1600 nm. The shift from high to low emissivity values occurs always at the same wavelength, confirming that 1000 °C isn't a critical temperature for this structure. The emitter after the annealing process (dashed blue line figure 6.9b) remain relatively stable and the transition from high to low emissivity values is preserved, but an emissivity increase was observed between 4000 and 6000

nm. The emitter behavior doesn't change a lot preserving the spectral energy density of the thermal stressed sample mainly before the highest solar cell bandgap considered (blue area with pattern). Figure 6.10c reports the change in the emitter efficiency for the thermal stressed sample. The maximum value at 1000 °C of 0.46 is reached at 0.63 eV, while 0.44 and 0.41 are the values at the considered bandgap range limits. The difference between the as deposited and thermal stressed emitter efficiency maximum value is of 4%, while 3% and 2% difference is observed for the values at the considered bandgap range limits, demonstrating the capability of this structure to work at 1000 °C preserving his characteristic.

The performance of the proposed SE was compared with four of the most effective SEs present in literature to date: Bhatt et al. [143], Chan et al. [144], Chirumamilla et al. [39] and Shimizu at al. [145]. The η_{SE} was calculated at 1000 and 1400 °C for the as-deposited structure with E_g = 0.55, 0.63, 0.66 and 0.72 eV. The results, reported in table 6.3, clearly show the decreasing trend of η_{SE}, starting from the lowest energy bandgap value for the literature SEs, whereas the SE proposed in this work presents the highest η_{SE} in the middle of the chosen energy bandgap range. This trend suggests that at 0.55 eV two out of four literature SEs [143,144] have an η_{SE} higher than those reported by our design; however, at 0.63 eV and above, our SE design results to be the best solution. Moreover, the η_{SE} of our design exhibits less variation throughout the energy bandgap range, resulting in the most coherent solution in the range considered. It is also interesting to note that the less good performance highlighted at 0.55 eV for our emitter becomes less important when increasing the working temperature, emphasizing a better behavior of our structure increasing the temperature.

Table 6.3. Emitter efficiency: comparison of the proposed design with previous literature

E_g (eV)	**Temperature (°C)**	**Emitter efficiency**				
		This work	**Shimizu et al.**	**Chan et al.**	**Chirumamilla et al.**	**Bhatt et al.**
0.55	1000	0.47	0.46	0.55	0.45	0.51
	1400	0.56	0.54	0.60	0.53	0.57
0.63	1000	0.50	0.40	0.50	0.39	0.40
	1400	0.61	0.52	0.58	0.51	0.51
0.66	1000	0.49	0.37	0.45	0.36	0.35
	1400	0.61	0.50	0.55	0.49	0.47
0.72	1000	0.43	0.30	0.35	0.29	0.26
	1400	0.57	0.44	0.48	0.44	0.39

6.4.3.3 Refractive indices: high temperature

The refractive indices at high temperature were measured on the whole deposited multilayer structure. The Linkam TSEL 1000 Vertical Heat Cell equipped on the J.A. Woollam RC2 Spectroscopic Ellipsometer was fluxed with nitrogen to avoid the oxygen contamination at high temperature. The samples were heated up to 1000°C and the results are shown in figure 6.11 – 6.12 – 6.13. The in temperature refractive indices were used to perform reflectivity simulation of the SE to take in account the reflectivity temperature dependence. The tungsten in temperature refractive indices is shown in figure 6.11.

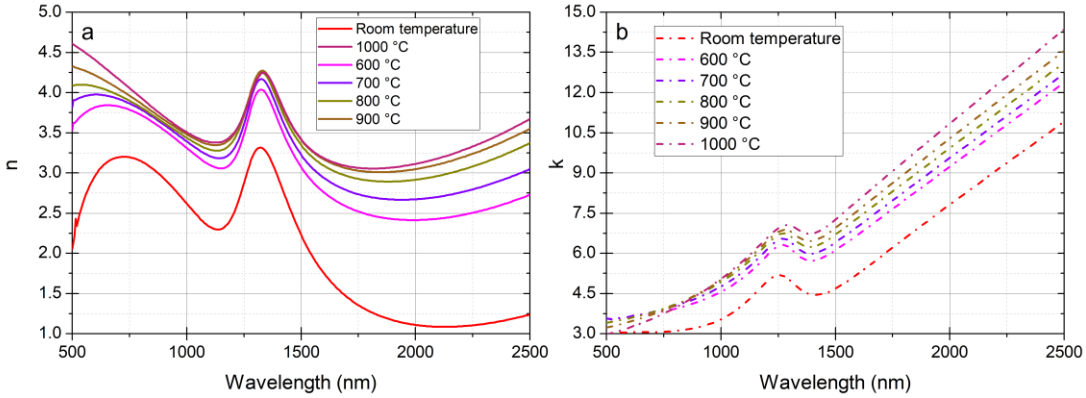

Figure 6.11. Tungsten refractive indices (a) and extinction coefficient (b) from room temperature to 1000°C.

Both refractive indices and extinction coefficient showed an increase with increasing temperature. This trend results to be confirmed also by previous high temperature measurements [146]. The SiN_x exhibit a similar trend with an increase of both refractive indices and extinction coefficient with increasing temperature (figure 6.12). This material behaviour looks to be very similar to the in-temperature silicon tendency [147,148]. This could be reasonable due to the high silicon presence in the sputtered SiN_x.

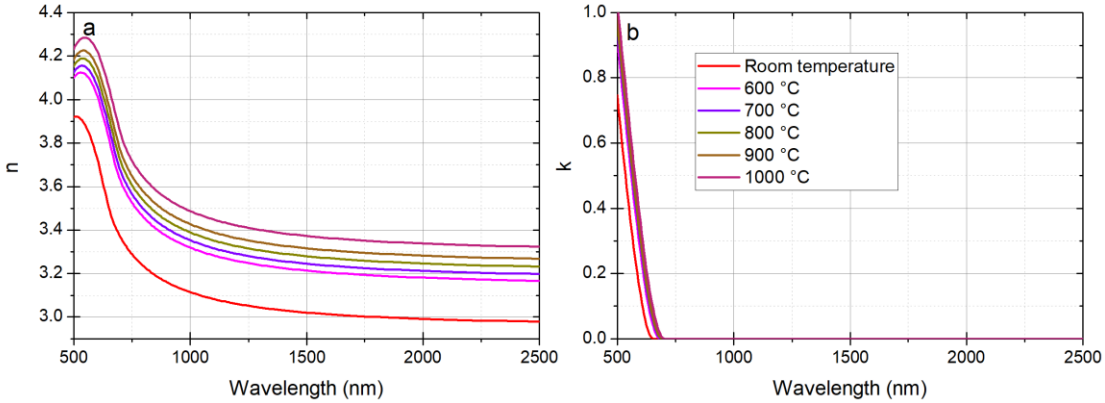

Figure 6.12. SiN_x refractive indices (a) and extinction coefficient (b) from room temperature to 1000°C.

The SiO_2 and TiO_2 refractive indices are reported in figure 6.13, the extinction coefficient of these materials is 0, in this wavelength region, for this reason is not reported. No data for this temperature range was found in literature, but other works [149,150] for lower temperature confirm the small refractive index temperature dependence of these materials.

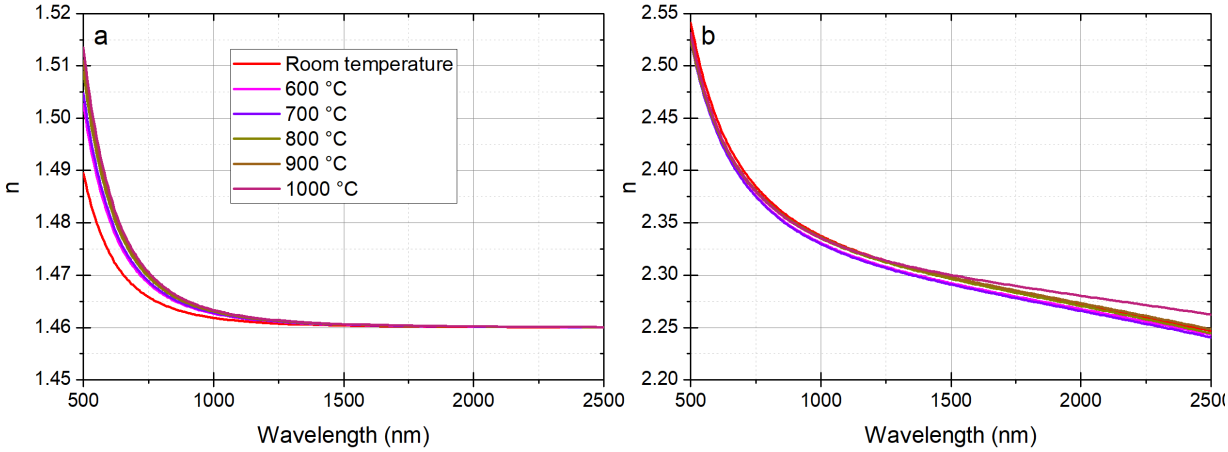

Figure 6.13. SiO_2 (a) and TiO_2 (b) refractive indices from room temperature to 1000°C.

6.4.3.4 In temperature emitter behavior and PV cell simulation

All the results listed in section 6.4.3.2 are refereed to measurements taken at room temperature, they give an idea of the emitter behavior and of his thermal stability but can't describe the real in temperature emitter functioning. To obtain a realistic in temperature emitter response the in temperature refractive indices were used to simulate the emissivity curve. The emissivity is calculated computing the reflectivity according to the transfer matrix method [110] utilizing the experimental in temperature refractive indices (section 6.4.3.3). The thicknesses used for the simulation are 88, 336, 255 nm for SiN_x, SiO_2, TiO_2 respectively. These thicknesses were obtained during 1000 °C ellipsometric measurement, they minimize the mean square error, and they are in agreement with the expected ones from deposition rate. The SiN_x thickness results to have the bigger increase (14%) probably due to his larger thermal expansion coefficient, while for SiO_2 and TiO_2 is observed a small thickness increase (about 3%). Figure 6.14a shows the emitter spectral response simulation at 1000 °C (magenta line).

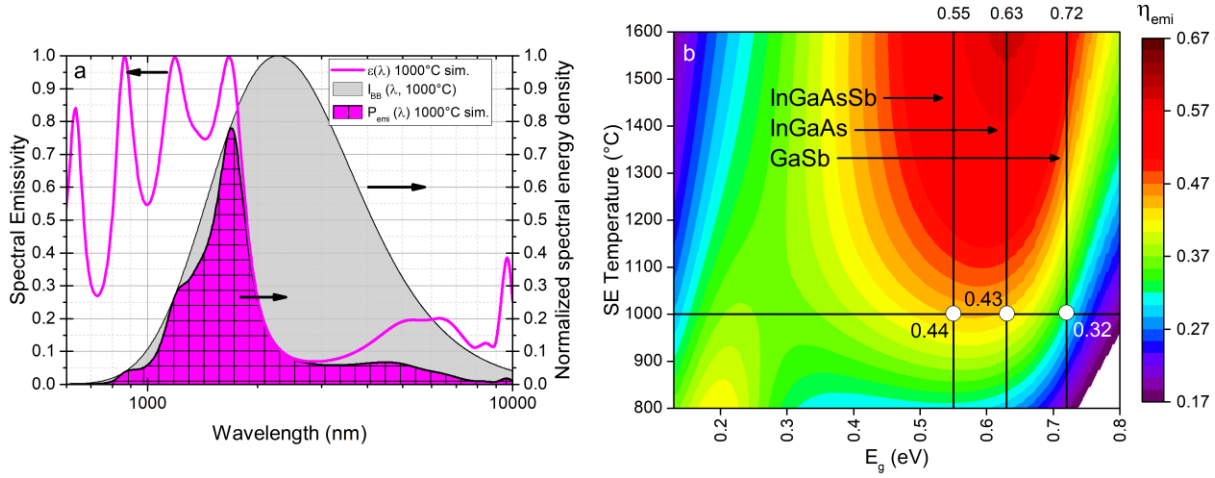

Figure 6.14. a) Left axis: Selective emitter simulation at 1000 °C (magenta line), Right axis: normalized spectral energy density of blackbody at 1000 °C and of simulated emitter at 1000 °C (grey area and magenta area with pattern respectively); b) Calculated emitter efficiency for the Selective emitter at 1000 °C as a function of temperature versus PV cell bandgap energy.

The main differences between the emitter behavior at 1000 °C and at room temperature are the shift of the peaks to higher wavelength and the increase of the emissivity values, both of these differences are due to the increases of the refractive indices with the temperature. A similar emissivity response, between 3000 and 8000 nm, can be observed for the emitter simulation at 1000 °C and the thermal stressed sample measured at room temperature, this is due to the formation of a diffusion layer between tungsten and SiN_x. These variations cause a larger emission in the high wavelength region leading to a worst emitter efficiency for the PV cells with high energy bandgap, but the fast transition from high to low emissivity values still guarantee the same emitter efficiency in a certain energy bandgap range (figure 6.14b). The emitter efficiency maximum value (0.44) for the simulated behavior of the SE at 1000 °C is reached at 0.55 eV and it is almost constant till 0.63 eV, after this energy bandgap the emitter efficiency start to decrease achieving 0.32 at 0.72 eV. A simulation of a real PV cell behavior exposed to the emitter at 1000 °C was used to calculate the PV cell power efficiency ($\eta_{PV\ cell}$), defined as:

$$\eta_{PVcell} = \frac{P_{out}}{P_{emi}} \tag{6.7}$$

where P_{out} is the PV cell electrical output power, and it was calculated starting with the current density (J(V)) as defined in [151]:

$$J(V) = \int_0^\infty \left[\frac{2qc}{\lambda^4}\frac{\varepsilon(\lambda)EQE(\lambda)}{e^{\frac{hc}{\lambda kT}}-1}\right]d\lambda - \left[\frac{q(n^2+1)E_g^2kT_d}{4\pi^2\hbar^3c^2}e^{\frac{E_g}{mkT_d}} + J_{nr}\right]\left(e^{\frac{qV}{mkT_d}}-1\right) \tag{6.8}$$

where q is the elementary charge of a proton, k is Boltzmann's constant, $h = 2\pi\hbar$ is Planck's constant, c is the speed of light, λ is the wavelength, EQE(λ) is the external quantum efficiency of the PV cell (approximately 82% above the bandgap), ε(λ) is the emissivity of the selective emitter,

T is the temperature of the emitter, E_g is the bandgap of the PV cell, m is the PV cell ideality factor, T_d is the cell temperature, n is the refractive index of the PV cell semiconductor region, J_{nr} is the dark current density induced by nonradiative recombination, and V is the applied voltage. The P_{out} is the maximum value obtained multiplying the J(V) by the applied voltage. The $\eta_{PV\ cell}$ was calculated as a function of PV cell energy bandgap and emitter temperature, and as expected the maximum value at 1000 °C (0.15) is reached at 0.55 eV and it is almost constant till 0.63 eV (figure 6.15), following the same behavior of the emitter efficiency.

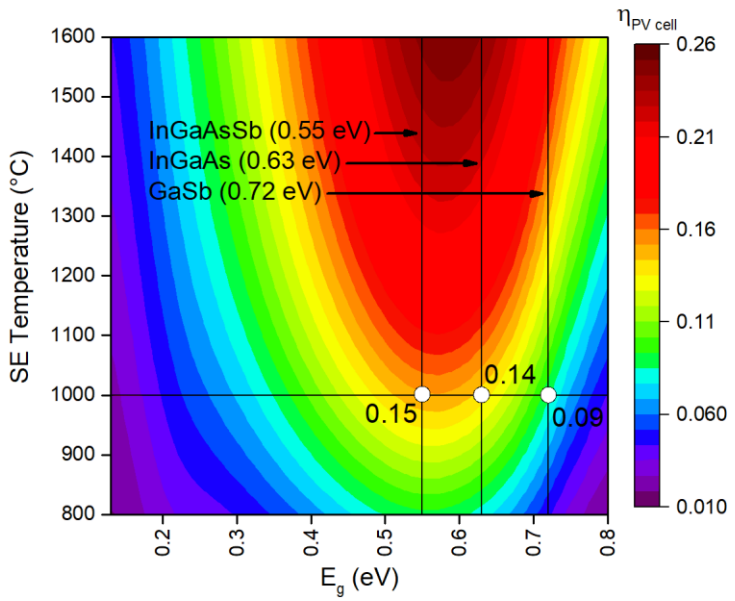

Figure 6.15. Calculated PV cell power efficiency ($\eta_{PV\ cell}$) for the selective emitter at 1000 °C as a function of temperature versus PV cell bandgap energy.

A $\eta_{PV\ cell}$ value of 0.15 at 0.55 eV represents also the SQ limit as reported in [152], demonstrating the high efficiency of the realized emitter. Figure 6.15 shows the possibility (hypothesizing the same emitter behavior) to reach a $\eta_{PV\ cell}$ value of 0.23, 0.24 and 0.25 for 1400, 1500 and 1600 °C emitter working temperature respectively, exceeding the SQ limit, pointing out the importance to reach high temperature to improve the PV cells performance.

In conclusion, we propose a selective emitter (SE) to be easily fabricated via sputtering deposition of SiN_x, SiO_2, and TiO_2 on a W substrate. The SE emissivity spectrum was simulated, by means of the transfer matrix method, starting from experimentally evaluated refractive indices. Through a genetic algorithm, its efficiency is optimized for a chosen operating temperature of 1000 °C and an extended range of bandgap energies, i.e. from 0.55 to 0.72 eV, to ensure proper functioning with most of the commonly used PV cells for STPV systems (semiconductors of the III-V groups). The deposited sample behaves very similarly to what was expected from simulations, reaching a maximum efficiency of 50% at 0.63 eV (at 1000 °C). Its thermal stability was demonstrated after a long thermal stress test carried out in a vacuum furnace at 1000 °C: its efficiency only slightly

decreased, reaching 46%. For a more reliable analysis of the SE properties, the refractive indices of the materials involved in the design were measured at various temperatures, from room temperature up to 1000 °C. Hence, a new simulation was performed and the results showed an efficiency equal to 44%. In addition, the behavior of a realistic PV cell exposed to the fabricated SE was also simulated: the results show a maximum efficiency of 15% at 1000 °C and the possibility of reaching an efficiency of 25% at 1600 °C, exceeding the theoretical limit of Shockley-Quisser. In conclusion, the proposed structure demonstrated high efficiency, thermal stability up to 1000 °C and versatility, as it can efficiently operate in the energy bandgap range of 0.55 to 0.63 eV.

7. Prediction of service lifetime of SSA for HVFPCs

As discussed in section 3.6, the thermal stability is a fundamental parameter for selective solar absorbers because a stable absorber guarantees certain performances along its service lifetime. The thermal efficiency of HVFPCs strictly depends on the radiative properties of the Selective Solar Absorber (SSA), in particular on the solar absorptance and the thermal emittance as defined from equation 3.13, here reported:

$$\eta_{panel} = \alpha_s - \frac{\varepsilon_{abs}(T)\,\sigma_{SB}(T_{abs}^4 - T_{amb}^4)}{C \cdot G_{Sun}} - \frac{\varepsilon_{sub}(T)\,\sigma_{SB}(T_{abs}^4 - T_{amb}^4)}{C \cdot G_{Sun}} \quad (7.1)$$

The optical properties (α_s and $\varepsilon(T)$) may change during the service lifetime of the solar collectors due to high temperature conditions [153], causing a decrease in absorber thermal efficiency and, consequently, in the energy production. For this reason, the evaluation of the optical properties of the absorber at working temperature and the prediction of the aging behaviour of these coatings is necessary.

The International Energy Agency (IEA) formulated an accelerated thermal stability testing and service life predication method for solar absorber coatings [42]. This method is currently the standard named ISO/CD 12592, 2 "Solar Energy – Materials for flat-plate collectors – Qualification test procedures for solar surface durability". Such standard, being developed for standard collector working in air at low temperature, assumes that the degradation is caused by diffusion processes according to the Arrhenius' law:

$$k = D_{Arrh}\, exp\left(-\frac{E_T}{R\,T}\right) \quad (7.2)$$

where k is the chemical reaction rate, D_{Arrh} is the Arrhenius constant, R is the constant of ideal gas, T is the temperature, and E_T is the activation energy per mole of the ageing process according to Arrhenius' law, which is the fundamental coating parameter that determines the ageing resistance at the operating temperature. The exponential temperature dependence of the Arrhenius law allows to perform accelerated aging tests using a temperature higher than the operating temperature and to estimate the failure time (the time at which the absorber efficiency is reduced more than the value defined according to the reported standard). However, the absorber temperature changes during the normal working conditions. Such temperature variations can be summarized by a temperature frequency function $f(T)$ that represents how many hours the absorber is at temperature T during one-year operation. According to the Arrhenius law, it is possible to replace the function $f(T)$ (that have a complex shape) with an effective constant temperature T_{eff} that produces the same aging effect than the real $f(T)$:

$$exp\left(-\frac{E_T}{R}T_{eff}^{-1}\right) = \int_{T_{min}}^{T_{max}} exp\left(-\frac{E_T}{R}T^{-1}\right) f(T)dT \quad (7.3)$$

where T_{max} and T_{min} are the maximum and minimum temperatures of the solar absorber observed over one year operation and $f(T)$ is the temperature frequency function. The standard defines $f(T)$

for Domestic Hot Water (DHW) applications. It is obtained as the averaged measured values from four different flat-plate collectors, exposed for one year in Rapperswil (Switzerland). The panels were kept for 11 months in operation and for 30 days at stagnation (Figure 7.1).

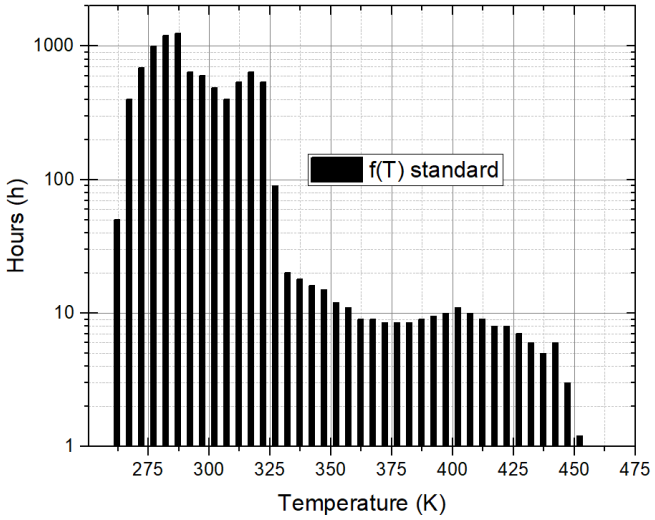

Figure 7.1. Temperature frequency function defined by ISO/CD 12592, 2 [42].

Once the T_{eff} is calculated, and if the activation energy E_T is known, it is possible to calculate a failure time (t_R in years) corresponding to a testing temperature (T_R). For a coating with an expected service lifetime of 25 years the t_R value can be determined by:

$$t_R = 25 \exp\left[-\frac{E_T}{R}\left(\frac{1}{T_{eff}} - \frac{1}{T_R}\right)\right] \quad (7.4)$$

The values of t_R and T_R are a compromise between the requirements of a testing time easily accessible (no more than few weeks), easily measurable with a small relative error (at least one hours), and a testing temperature not too higher than the stagnation temperature, to avoid the activation of other degradation mechanisms (with a different activation energy).

To estimate the activation energy, the standard procedure aims to obtain the same degradation in two tests performed at different temperatures. According to IEA, the degree of aging of a coating can be evaluated through the product of the chemical reaction rate (k) and the time of the chemical reaction (t), called Performance Criterion (PC), it can be also evaluated by measuring the optical characteristics of the absorber:

$$PC = k \cdot t = -\Delta\alpha + 0.5\Delta\bar{\varepsilon} \quad (7.5)$$

where $\Delta\alpha = \alpha_S' - \alpha_S$, $\Delta\bar{\varepsilon} = \bar{\varepsilon}_t' - \bar{\varepsilon}_t$, α_S' ($\bar{\varepsilon}_t'$) represents the absorptance (the thermal emittance) after testing, and α_S ($\bar{\varepsilon}_t$) the absorptance (the thermal emittance) of the virgin sample. The different roles and weights of absorptance and thermal emittance in determine the efficiency in the solar thermal collector for DHW applications define the signs and the factor 0.5 in eq. 7.5.

The PC value is periodically measured during the tests, and the ageing test is stopped when a measurement returns a PC value higher than 0.05, which has been defined as the maximum degradation for a service lifetime of 25 years (Standard ISO/CD 12592, 2). The time when the PC reaches 0.05 during testing is not experimentally accessible and it is usually extrapolated from the different measurements. Such extrapolated time value can be used in eq. 7.4 to evaluate the service lifetime. The procedure flow of the current standard is shown in figure 7.2.

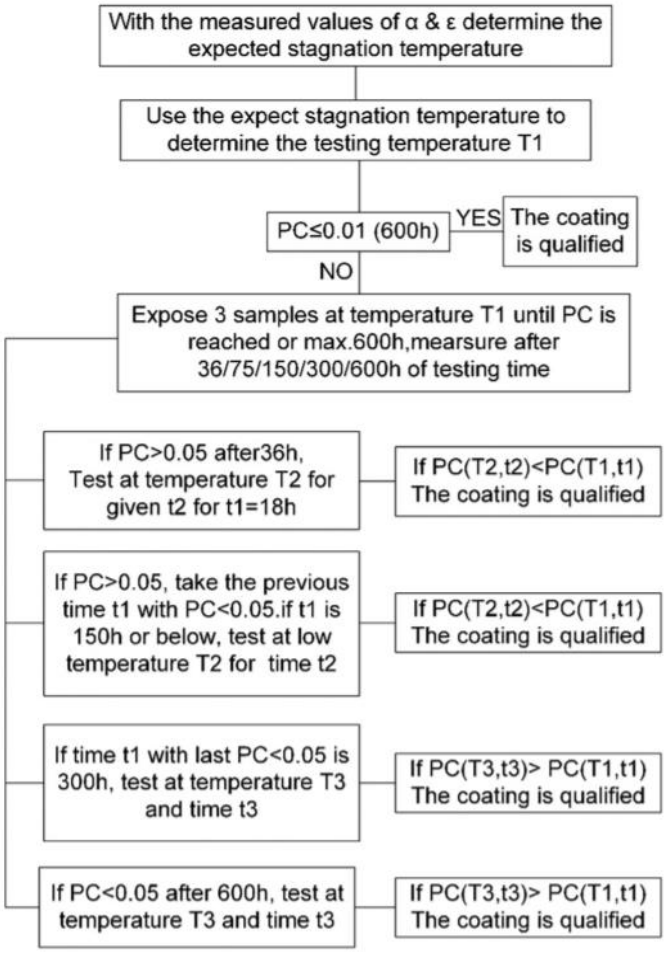

Figure 7.2. Procedure flow of the current standard

Because this method has been developed for collectors working in air at low temperature, it is not adequate to evaluate the service lifetime of solar absorber in HVFPCs. For this reason, a review of the current standard is necessary.

7.1 Novel definition of the Performance Criterion

The activation energy (E_T) is the key parameter to describe an aging process. The E_T is the minimum energy needed to reach a certain degradation through a chemical reaction. To calculate the E_T is necessary to define a performance criterion (PC), this criterion is used to evaluate the

absorber performance degradation during thermal aging test. The current standard define the Performance Criterion (PC) as reported in equation 7.5. The standard PC suggested formula aims to evaluate the change in absorber performance during a thermal aging test. It is important to notice that the standard PC could be also written as the difference of the absorber efficiency (η_{abs}) (section 3.3) before (η'_{abs}) and after (η''_{abs}) a thermal aging test, when the weighting factor (w) (eq. 7.8) assumes a value of 0.5 in equation 7.7:

$$PC = k \cdot t = -\Delta\alpha + 0.5\Delta\bar{\varepsilon} = \Delta\eta_{abs} = \eta'_{abs} - \eta''_{abs} \quad (7.6)$$

$$\eta_{abs} = \alpha - w\varepsilon \quad (7.7)$$

$$w = \frac{\sigma_{SB}(T_{abs}^4 - T_{amb}^4)}{G_{Sun}\, C} \quad (7.8)$$

For flat plate collectors (C = 1), the w assumes a value of 0.5 at about a T_{abs} of 90 °C as reported in Figure 7.3.

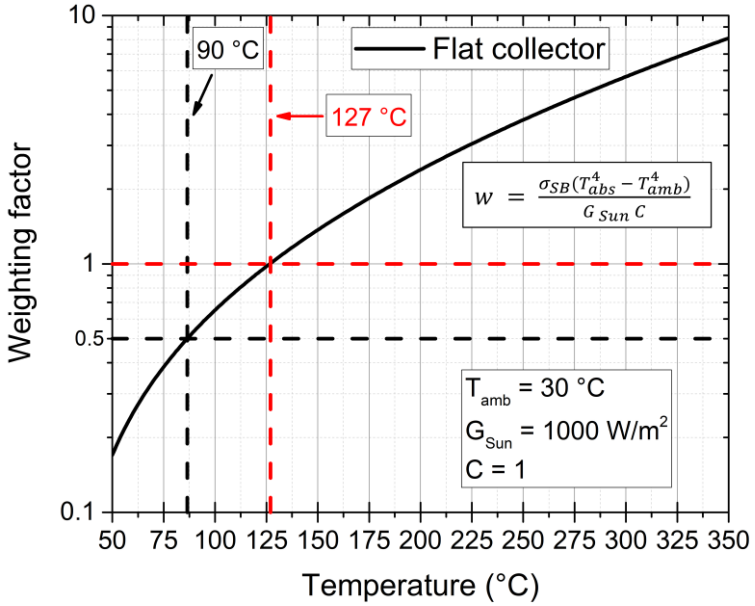

Figure 7.3. Weighting factor for flat plate collectors as a function of absorber temperature.

The weighting factor value, as showed in figure 7.3, increases as the absorber temperature increases, and the fixed weighting factor (0.5), established by the standard, is reasonable for the solar thermal collectors for DHW applications, where the absorber working temperature (T_{abs}) is about 90 °C, but after the temperature of 127 °C , w > 1, meaning that the thermal emittance begin to have more importance than solar absorptance in terms of absorber performance. As previously discussed (section 2.4.6), the HVFPCs aim to reach a working temperature of 200 °C or higher, for this reason the standard PC (with a fixed thermal emittance weight) cannot be used also for the HFPCs. To take in account the relative importance of solar absorptance and thermal emittance a novel Performance Criterion is proposed. As pointed out by Cao [66], the relative weight depends

by the operating temperature and this would result in a temperature dependent PC. The use of the overall efficiency (eq. 7.1) to define a performance criterion solves the problem of the PC temperature dependence and represents a more useful and appropriate criterion for the absorbers. The proposed performance criterion ($PC_\eta(T)$) is defined as:

$$PC_\eta(T) = \Delta\eta_{panel}(T) \tag{7.9}$$

with $\Delta\eta_{panel}(T) = \eta_{panel}(T) - \eta'_{panel}(T)$, where $\eta_{panel}(T)$ is the virgin absorber overall efficiency and $\eta'_{panel}(T)$ is the absorber overall efficiency after thermal aging test.

The proposed performance criterion ($PC_\eta(T)$) results to be a better parameter to describe the change in absorber performance during thermal aging test, because is able to adapt the relative weight of absorptance and thermal emittance, depending on absorber working temperature, and also take in account the influence of the substrate thermal radiation losses. Indeed, the $PC_\eta(T)$ is equally effective to eq. 7.5, if we consider 90 °C as absorber working temperature but enlarge the application also to high absorber working temperature, making the $PC_\eta(T)$ a more precise and versatile criterion.

7.2 Temperature frequency function novel evaluation

One of the most important parameters to calculate the service lifetime of a SSA is the temperature frequency function. The temperature frequency function $f(T)$ represents how many hours the absorber is at temperature T during one-year operation. This function, thanks to the equation 7.3, can be replaced with an effective constant temperature T_{eff} that produces the same aging effect than the real $f(T)$. The T_{eff} is used to calculate the failure time of a thermal aging test through equation 7.4. The current Standard presents the $f(T)$ as the averaged measured values from four different flat-plate collectors, for Domestic Hot Water (DHW) applications, exposed for one year in Rapperswill (Switzerland) and, in this year of observation, the collectors are maintained under working conditions for 11 months and 30 days under stagnation (fig. 7.1). An updated procedure to adapt the standard $f(T)$ for other types of solar collectors is presented in [154] and consists in a re-scaling method that takes account of the difference in stagnation temperature of absorber but assumes that the shape of the temperature curve will not be changed by different absorber optical properties. The shape of the standard $f(T)$ strongly depends on the absorber, mounted in the solar collectors during the measures campaign, and on the location where the collectors were exposed, therefore it could be reasonable only for thermal collectors for DHW applications. For this reason, the standard $f(T)$ cannot be used also for HVFPCs and a procedure to obtain the specific $f(T)$ for absorbers mounted on HVFPCs is presented. This procedure prescribes to use a dynamic simulation to build the absorber temperature history in operating conditions while the temperature trend under stagnant condition is derived from experimental data collected with a Test-Bench. The simulation model is based on TVP Solar HVFPCs parameter, the same model of HVFPC is mounted on the Test-bench for the experimental campaign.

Re-scaled $f(T)$ for absorber stagnation temperature of 300 °C

TVP-Solar HVFPCs reach higher temperature than conventional flat plate solar collectors thanks to the high vacuum insulation and their absorber coating can achieve stagnation temperatures higher than 300 °C. An update procedure to re-scale $f(T)$ for absorbers with different stagnation temperature is presented in [154]. The Standard and the re-scaled absorber temperature frequency function for collectors with stagnation temperature of 300 °C, are reported in Fig. 7.4 in black and red respectively. Setting a hypothetical value of the activation energy (E_T) of 100 kJ/mol, the T_{eff} obtained from the re-scaled histogram, using (7.3) is equal to 190 °C.

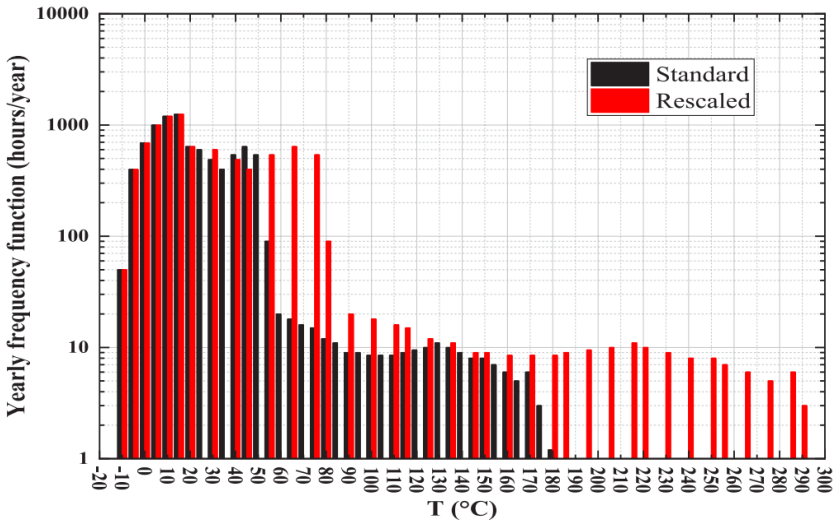

Figure 7.4. Curve in black [155]*: Reference absorber temperature frequency function valid for absorber with stagnation temperature of 180 °C (standard $f(T)$). Curve in red* [154]*: Re-scaled absorber temperature frequency function valid for absorbers with stagnation temperature of 300 °C.*

Methodology for $f(T)$ calculation

The procedure for $f(T)$ calculation prescribes to use a dynamic simulation implemented in Simulink to build the absorber temperature history in operating conditions while the temperature trend under stagnant conditions is derived through experimental data collected with a Test-Bench.

Simulation model description

In order to evaluate the TVP-Solar HVFPC's absorber temperature frequency function, in operating conditions, a simulation model was developed using Simulink software [156]. In Fig. 7.5 a simple scheme of the model is shown. It includes a tank where the heat transfer fluid (HTF) is stored at constant pressurization (1 MPa), a centrifugal circulation pump whose rotation frequency regulates the flow rate of the HTF circulating inside the HVFPC, modeled with the characteristics of TVP Solar panels, a three-way valve that has the function to direct the fluid through a radiator when the tank temperature overcomes an imposed limit.

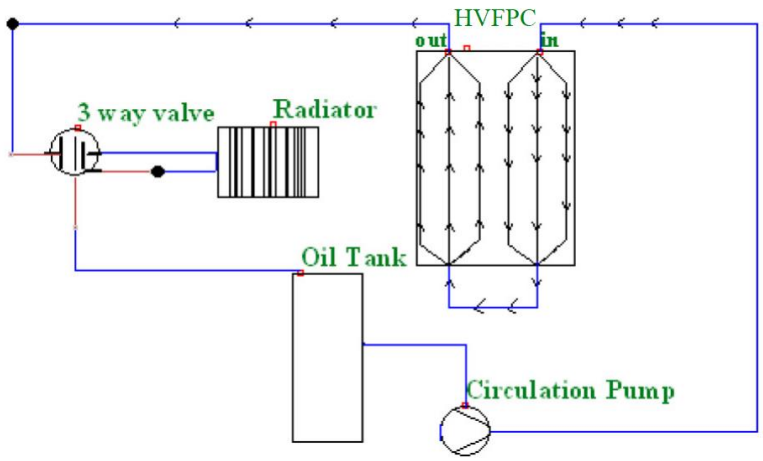

Figure 7.5. Simplified scheme of the Test Bench modeled in Simulink.

To model this system, blocks of Simscape fluids library have been used. Once built the elements of the model, the simulation works giving as inputs the properties of the HTF, the mass flow rate during functioning and the weather data for the specified location and time of observation (Ambient Temperature (°C), Solar irradiation components (W/m^2) considering that the orientation angles of the HVFPC are settled to the optimal values (Slope β = 30°, Azimuth = 0°)). Regarding the computation of $f(T)$, it is assumed that the instantaneous temperature of the HTF and the collector absorber temperature are the same and that the absorber optical properties remain constant during a year of functioning. The simulation, carried out in transient, at every time step provides as output the instant working fluid medium temperature $T_{mf}(t)$, the necessary parameter for the $f(T)$ construction. The rise in temperature of the HTF that passes through a solar collector depends on the thermal power converted, as expressed by the principle of calorimetry:

$$Q = \dot{m}\, c_p\, (T_o - T_i) \tag{7.10}$$

Where Q is the thermal power (W), $\dot{m}$ is mass flow rate (kg/s), c_p is the specific heat at constant pressure (kJ/ (kg °C)), T_o is outlet fluid temperature (°C) and T_i is the inlet fluid temperature (°C). The thermal power converted is equal to the portion of solar irradiation (G) converted multiplied for the collector surface (A_c):

$$Q = \eta \cdot G \cdot A_c \tag{7.11}$$

where η is the collector thermal efficiency that, for flat plate solar collectors, can be expressed following the standard formula (eq. 7.12) that models the heat losses of the collector as a second-degree function of the difference between ambient e fluid Temperature ($T_{mf} - T_a$) [157]:

$$\eta_{st} = \eta_0\, IAM_\theta - \left[\frac{c_1(T_{mf} - T_a)}{G} - \frac{c_2(T_{mf} - T_a)^2}{G}\right] \tag{7.12}$$

where η_0 is the fraction of perpendicular irradiance converted into useful heat when the fluid temperature is identical to the ambient temperature T_a. It can be calculated multiplying a correction factor between the average absorber plate temperature and the inlet fluid temperature, named collector heat removal factor F_R, and the transmittance – absorptance product at normal irradiance. The factor c_1 and c_2 in (eq.7.12) are the first and second order collector heat loss coefficients respectively. The incidence angle modifier (IAM) function describes the optical efficiency for a certain radiation incidence angle θ (off normal) normalized by optical efficiency when solar irradiation is perpendicular to the collector surface [158]. The different irradiation components G_b, G_s, G_r are weighted by individual Incidence Angle Modifiers (IAM) K_b, K_s, K_r to take into account the changes in the conversion factor due to non-perpendicular irradiance of these radiation components [159]. For dynamic collector tests K_s, K_r are summarized in one single IAM K_d for diffuse irradiance from the overall collector hemisphere G_d. This K_d is a constant collector parameter determined for isotropic diffuse irradiance and it is provided in collector test reports [160]. Therefore, K_b is usually approximated according to [161]:

$$K_b\,(\theta_L, \theta_T) \;=\; K_b\,(\theta_L, 0)\;\cdot\; K_b\,(0, \theta_T) \qquad (7.13)$$

where θ_L and θ_T are the projection of θ (angle between solar beam and the collector surface normal) into the longitudinal and transversal collector planes. The TVP-Solar Panels efficiency coefficients are reported in Tables 7.1 and 7.2 in which the zero-loss efficiency η_0, the first order heat loss coefficient c_1, the second order heat loss coefficient c_2, and Incident Angle Modifier coefficients are obtained through a standard test effected according to EN ISO:9806 2013 & ICC 901/SRCC 100-2015 carried out by: Solar and Heat Technology Stuttgatt (SWT). During the simulation the medium fluid temperature is evaluated every time step.

Table 7.1. TVP Solar panels efficiency coefficients.

Coefficients	Value
η_0	0.737
c_1	0.5
c_2	0.006
K_d	0.95

Expressing the IAM coefficients, the standard efficiency in (eq. 7.12) becomes:

$$\eta_{st} \;=\; \left[\eta_0\;\frac{K_b\,(\theta)\,G_b + K_d\,G_d}{G}\right] \;-\; \left[\frac{c_1(T_{mf} - T_a)}{G} \;+\; \frac{c_2(T_{mf} - T_a)^2}{G}\right] \qquad (7.14)$$

Multiplying equation 7.14 for the collector gross area A_c at incident solar irradiation G, the instantaneous power given to the HTF can be obtained as equation 7.15. The inputs of the simulation model are the HTF characteristics, the HTF mass flow rate (kg/s) and the weather data

(hourly ambient temperature (°C) and Solar Irradiation (W/m^2) components on a tilted surface (tilt = 30°)).

$$Q(t) = \left\{[\eta_0(K_b(\theta)\, G_b(t) + K_d\, G_d(t))] - \left[c_1\left(T_{mf}(t) - T_a(t)\right) + c_2\left(T_{mf}(t) - T_a(t)\right)^2\right]\right\} \quad (7.15)$$

With the imposition of the weather data, assuming a value of an initial fluid inlet temperature ($T_i(1) = T_a(1)$), the software computes iteratively the instantaneous average fluid temperature from a thermal balance (eq. 7.16):

$$T_o(t) = \frac{\left\{[\eta_0(K_b(\theta)\, G_b(t) + K_d\, G_d(t))] - \left[c_1\left(T_{mf}(t) - T_a(t)\right) + c_2\left(T_{mf}(t) - T_a(t)\right)^2\right]\right\}}{\dot{m}\, c_p} + T_i\,(t) \quad (7.16)$$

$$T_{mf}\,(t) = \frac{T_o(t) + T_i\,(t)}{2} \quad (7.17)$$

Once obtained the HTF average temperature distribution over the simulated time, that is considered equal to the absorber average temperature distribution, it is possible to derive the simulated temperature frequency function $f(T)$ for the operating conditions.

Absorber temperature trend in stagnant conditions

The coefficients reported in Tables 7.1 and 7.2 are obtained from experimental data collected with a standard test conducted for a maximum temperature of 180 °C and, for this reason, the mathematical model presented above is not valid for higher collector temperature. For the stagnant conditions, the temperature profile of a highly selective absorber was measured in a TVP-Solar HVFPC installed in Avellino/Italy, facing south with a tilt angle of 30° (see Fig. 7.6a). The profile was recorded on 28th of September 2018 with a maximum global radiation of about 1000 W/m^2 (Fig. 7.6b) measured on the collector plane. The stagnation temperature was 300 °C. The corresponding daily absorber temperature frequency function $f(T)$ represents the sample daily $f(T)$ for HVFPCs in stagnant conditions. Multiplying the daily $f(T)$ for 30, it is possible to derive the stagnation month $f(T)$ (see Fig. 7.7a).

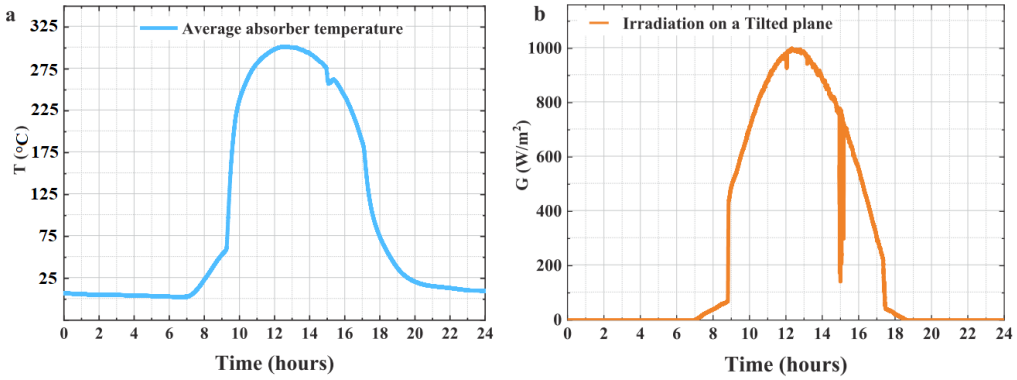

Figure 7.6. (a) Measured temperature of a selective absorber in a High Vacuum Flat Plate Collector during stagnation; (b) Measured solar Irradiation on collector plane.

Temperature frequency function evaluation with dynamic simulation

A new $f(T)$ suitable for HVFPCs is provided in order to get more reliable results than that obtained with the re-scaled $f(T)$ (histogram in red in Fig. 7.4). The histograms relative to HVFPCs considering 4 different Operating Temperatures (O.T. = 60 °C, 90 °C, 120 °C, 180 °C), obtained through dynamic simulations and experimental data, are represented. The minimum O.T. is characteristic of DHW applications, while the maximum O.T. is a reference value for medium temperature applications. The dynamic simulation gives as result the temperature trend of the collector over the simulated time that is subsequently summarized as a histogram. To obtain a direct comparison, as inputs of the dynamic simulations, meteorological data of the standard test location (Rapperswill) were imposed. The hourly meteorological data were downloaded from the Solar radiation tool of the Joint Research Centre (JRC) website [162] (setting the desired year, location coordinates, collector orientation angles). The simulation model also needs in input the HTF characteristic and, in these cases the XCELTHERM®500 (-60 – 260 °C) has been chosen with a mass flow rate circulation during daylight hours, settled equal to the nominal value for oil $\dot{m}$ = 516 (kg/h) (reported on TVP-Solar panel certification). The TVP-Solar HVFPC absorber temperature frequency functions $f(T)$ obtained from simulations at different O.T.s are reported in the following Fig. 7.7b.

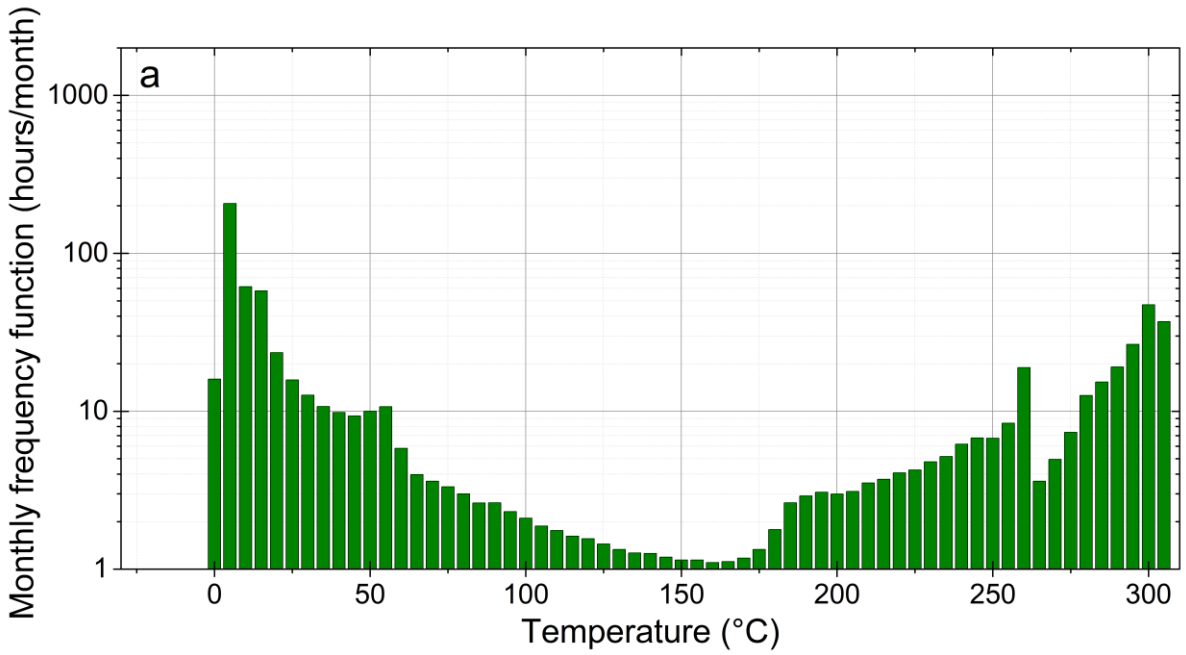

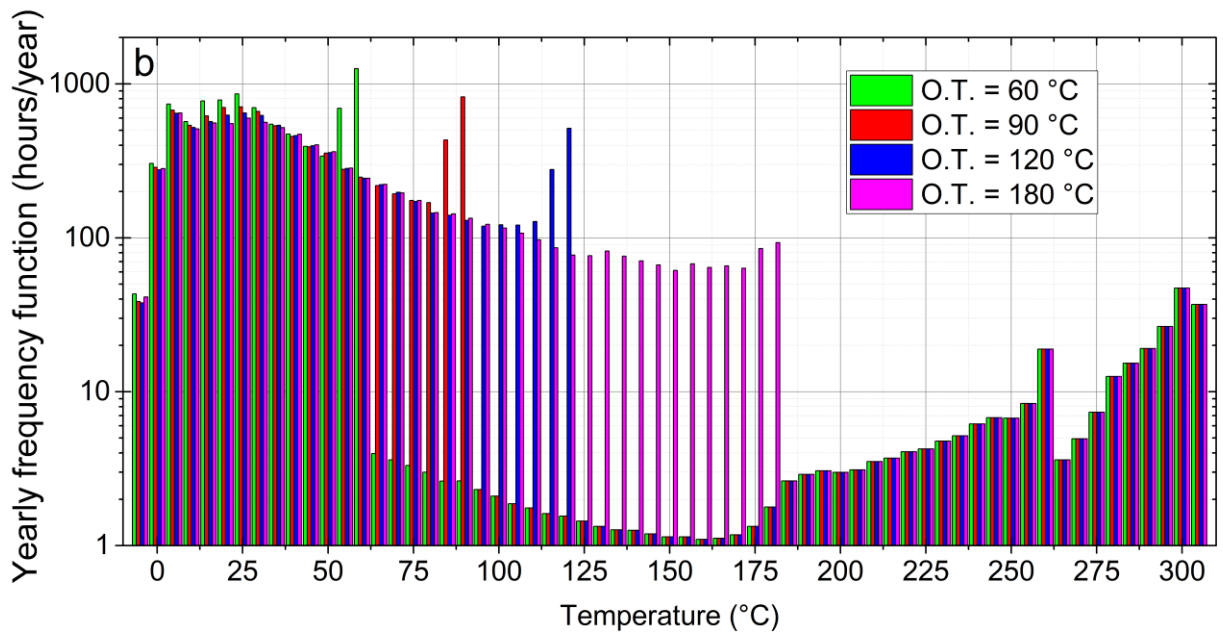

Figure 7.7. (a) HVFPC $f(T)$ relatives to 30 days of stagnation (b) Absorber temperature frequency functions relative to 11 months of operation and 30 days of stagnation valid for HVFPCs considering 4 different operating temperatures (O.T. = 60 °C, 90 °C, 120 °C, 180 °C).

The temperature range of analysis from -20 to 305 °C is divided in intervals of 5 °C. In Fig. 7.7b (logarithmic scale), the number of hours in which the collector absorber works under each interval can be seen. The temperature data of period in stagnation are obtained from histogram in fig. 7.7a. Unlike the re-scaled $f(T)$ (Fig. 7.4), is notable, in Fig. 7.7b, that the collector O.T.s are easily distinguishable (temperature which the absorber reaches for the major number of hours). Analyzing the case of O.T. equal to 180 °C is evident that the shape of the $f(T)$ is different from the other cases, clear indication that the HVFPC is not able to operate at that temperature for a desirable number of hours under the meteorological conditions of Rapperswill. Utilizing the histograms reported in Fig. 7.7b to compute the T_{eff} (E_T assumed equal to 100 kJ/mol), these results equal to 242 °C for every considered case (for every O.T.) instead of the 190 °C, which is the result obtained with respect to re-scaled $f(T)$. The difference between the analyzed cases is negligible because, for the strong non-linearity of the Arrhenius-type kinetics (see eq. 7.3), the temperature load under operating conditions affects much less the calculation than that under stagnation, that does not depend on O.T. Established that the main role in the calculation of T_{eff} is played by the stagnation period, is observable that the assumption of 30 days of stagnation in one year made by the Standard, is realistic for conventional flat-plate collectors used to produce DHW, but when looking at HVFPC, for industrial applications, 30 days of unproductivity cause unacceptable energy loss. The T_{eff} computed for every considered collector operating temperature (O.T. = 60 °C, 90 °C, 120 °C, 180 °C) by varying the stagnation period length (1, 2, 3, 4, 5, 10, 15, 20, 25, 30 days), are reported in Fig. 7.8 that shows a logarithmic trend of T_{eff} with the rise of

stagnation period length. On the same graph is also represented the T_{eff} computed using the re-scaled $f(T)$ (30 days of stagnation). As the days under stagnation increase, the influence on T_{eff} of the different working temperatures becomes less valuable. In the case of absence of stagnation (stagnation period length = 0), the T_{eff} for each O.T. is almost equal to the collector O.T. considered. The difference in terms of T_{eff} obtained at the different operating temperatures of 60 °C, 90 °C, 120 °C is negligible already from the first day of stagnation. After 10 days into stagnation, all the considered operating temperatures became equivalent with respect to T_{eff} calculation. It follows that it is important to predict a realistic fallowing period for the industrial solar plant to calculate a reliable effective temperature of solar collectors.

The results show clearly that there is a difference in the evaluation of the $f(T)$ following the current standard and using the simulation model with any operating temperature considered. This difference leads to a different T_{eff} calculated value, and consequently to a different failure time. For this reason, the use of the simulation model to predict the $f(T)$ for HVFPCs is more reasonable. Thanks to the simulation model, the $f(T)$ trend in different location and for different operating temperature can be investigated. To take in account a high stressful $f(T)$ to be used during service lifetime calculation (section 7.4), Dubai was chosen as location, an operating temperature of 100 (a) and 200 °C (b) was established, and 0-10-20-30 stagnation days was considered, the results are reported in figure 7.9.

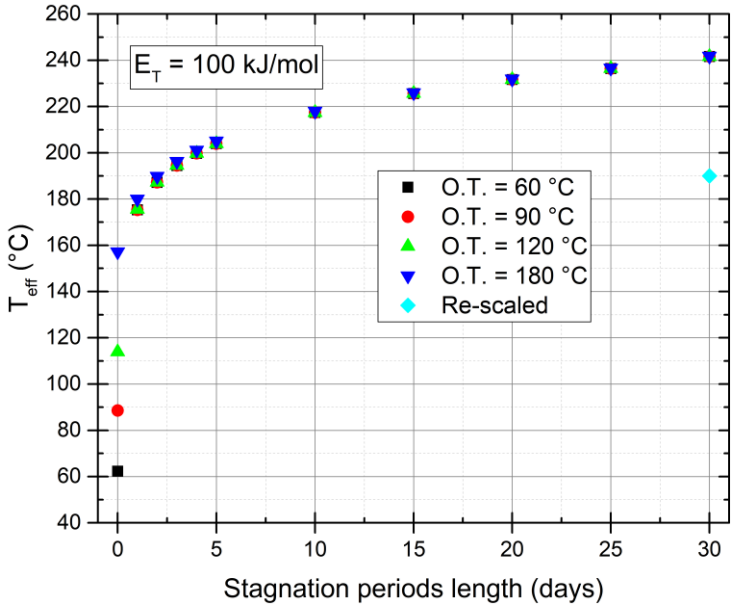

Figure 7.8. Variation of T_{eff} with stagnation periods length for 4 operating temperatures (O.T. = 60 °C, 90 °C, 120 °C, 180 °C).

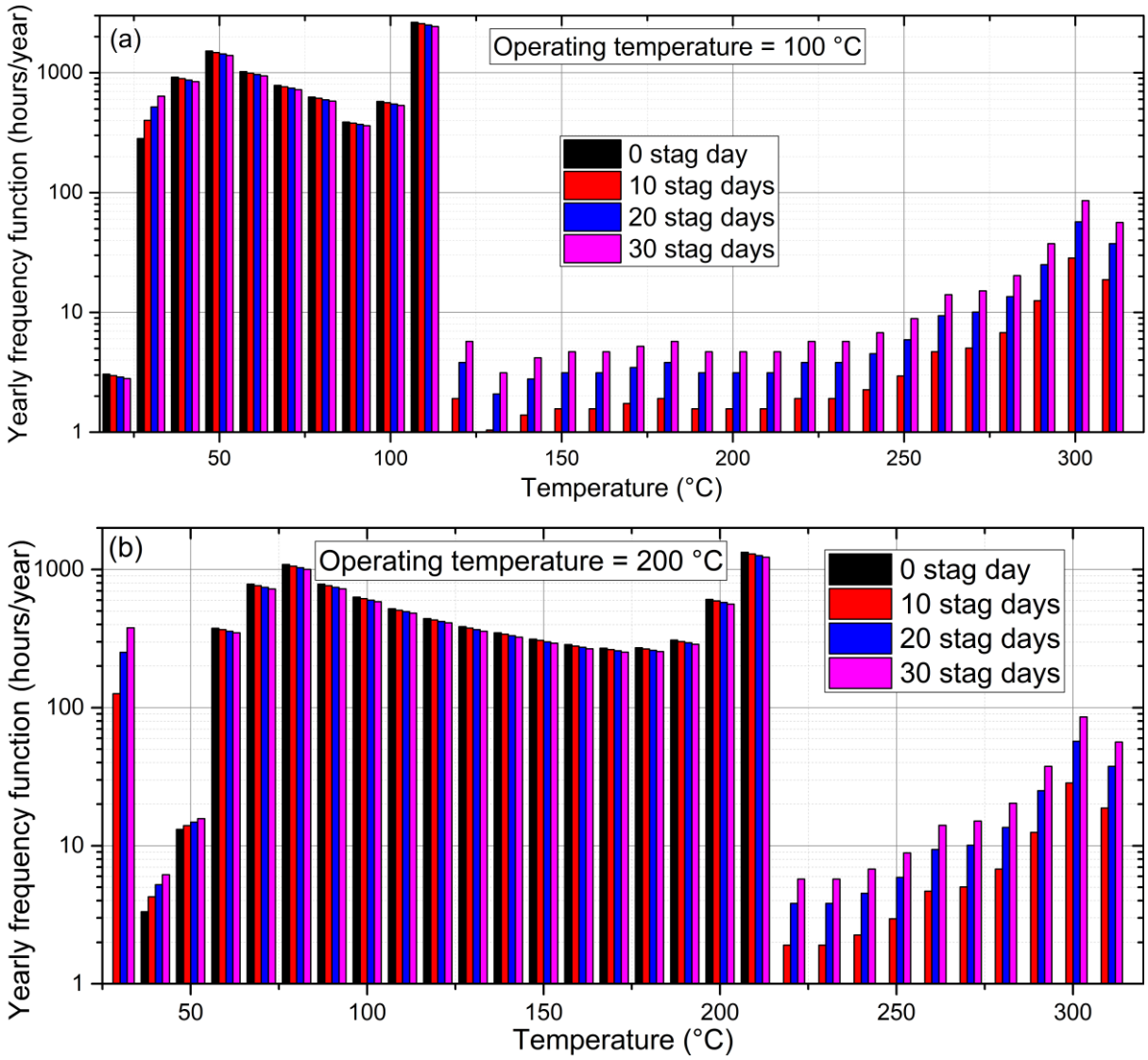

Figure 7.9. Dubai temperature frequency function evaluation for an operating temperature of 100 (a) and 200 °C (b), with 0-10-20-30 days of stagnation period length (black, red, blue and magenta column respectively).

7.3 Thermal aging tests of commercial SSA for HVFPCs

To predict the service lifetime of an SSA, the calculation of the activation energy (E_T) is mandatory. As described in section 7.1, it is possible to obtain the E_T thanks to the evaluation of the performance criterion (PC) trend during thermal aging tests. For this reason, 7 different thermal aging tests were performed on a commercial SSA (Mirotherm®) and consequently the E_T was calculated.

The tests were performed with the vacuum oven (section 4.4), thanks to this apparatus we are able to execute 3 tests with different temperatures at the same time, strongly reducing the total thermal aging test time. The tested temperatures were: 360, 370, 380, 390, 400, and 420 °C, the 400 °C test was repeated in order to check the reliability of the tests. The samples were tested for a certain time-step (t_i) and the solar absorptance and thermal emittance were measured at each t_i. The solar absorptance was computed with optical measurements performed with an OSA equipped with an integrating sphere (section 4.6), while the thermal emittance was calculated thanks to calorimetric measurements executed with the Mini Test Box (section 4.3). The thermal emittance was evaluated at 3 temperatures (100, 200 and 300 °C), representative of the absorber behavior for low, mid and mid-high temperature applications respectively, while for solar absorptance the temperature dependence was neglected. Both the standard PC and the novel proposed PC_η (section 7.1) were calculated during the tests at each t_i.

The trends of the solar absorptance and thermal emittance for each test are reported in fig. 7.10. The solar absorptance behavior is similar for each test, showing a considerable decrease after the first time-step and then manifesting an almost linear decreasing response. The thermal emittance exhibits a slightly increase for all the tests and for all the evaluated temperatures (100, 200 and 300 °C), with a maximum change of 0.01 all over the testing time. The test 1 and 4, tested at 400 °C, show similar value and similar trend for both solar absorptance and thermal emittance, confirming the reliability of these measurements.

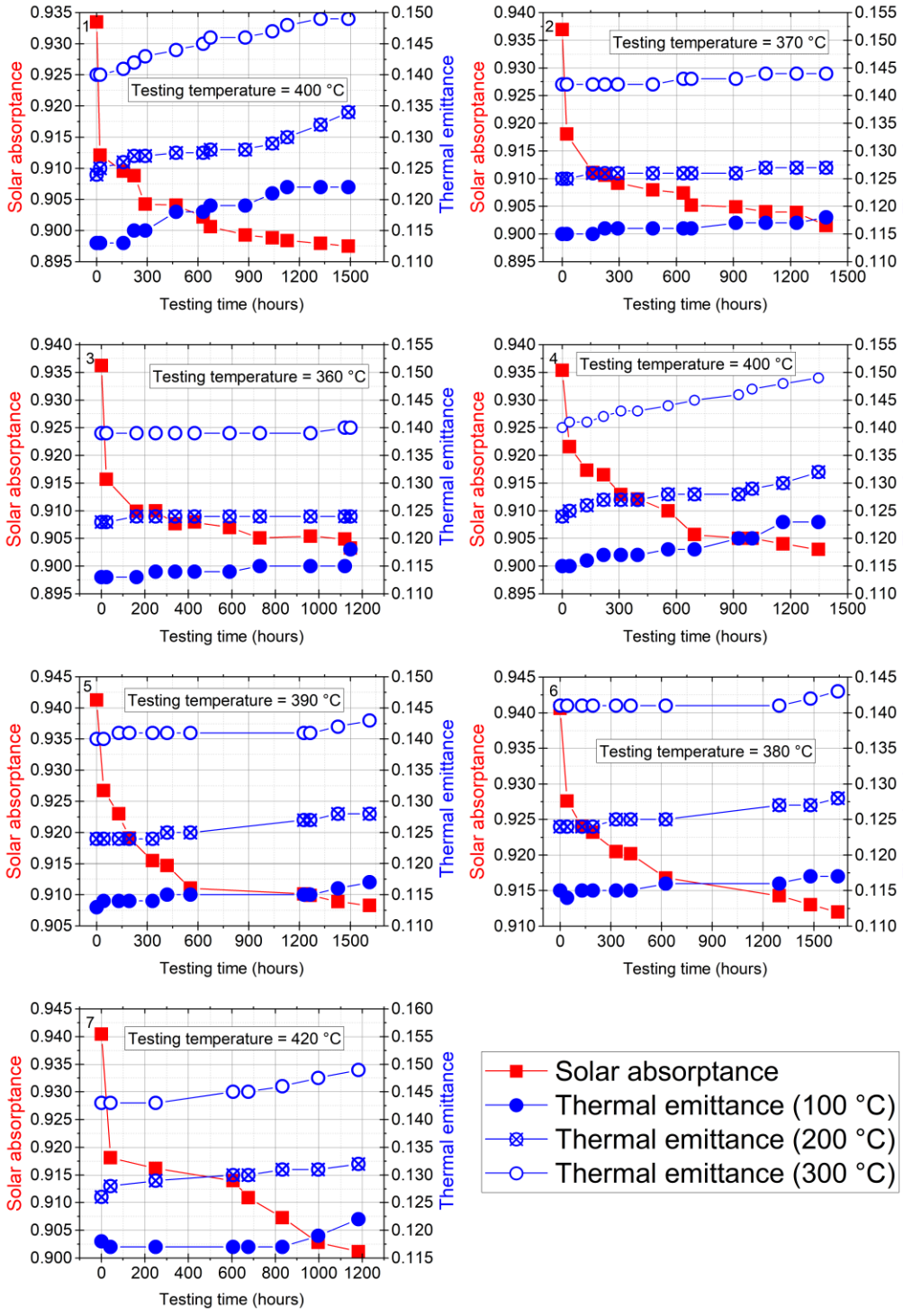

Figure 7.10. Left axis: Solar absorptance (red square) trend during the 7 thermal aging tests; Right axis: Thermal emittance at 100, 200 and 300 °C variations (solid, x centered and open blue circle respectively) during the 7 thermal aging tests.

According to Arrhenius' law multiplying the equation 7.2 for each temperatures testing time-step (t_i), we obtain:

$$k\ t_i = t_i\ D_{Arrh}\ exp\left(-\frac{E_T}{R\ T_j}\right) \tag{7.18}$$

Where the first term k t_i, is the PC_i at t_i time-step, as described in equation 7.5, D_{Arrh} is the Arrhenius constant, R is the gas constant and T_j is the testing temperature of the j-th test. In this equation the PC can be evaluated (using the standard formula (eq. 7.5) or the proposed one (eq. 7.9)), the t_i can be accurately measured, and T_j and R are known, consequentially D_{Arrh} and E_T are the only unknown. Accordingly, combining two tests at two different temperatures we obtain 2 different equations from equation 7.18 (one for each testing temperature) and we are able to evaluate the E_T. The E_T calculated, following the Arrhenius' theory, is able to describe how the considered PC changes during the time and consequently to provide the absorber behavior along the service lifetime. For this reason, the E_T evaluated with this procedure is strictly dependent on the PC considered. To obtain a more reliable value of the E_T, 7 different tests at 6 different temperatures were performed, in order to have 20 different combinations to calculate the E_T.

The standard (PC st.) and proposed (PC_η) performance criterions were calculated for all the tests at each time-step (fig. 7.11) according to equations 7.5 and 7.9. The PCs describe the absorber performance degradation during thermal aging test, and they were evaluated at the 3 considered operating temperatures, in order to predict the absorber behavior at these temperatures.

It is important to notice how the variation in thermal emittance is not constant varying the considered operating temperature, leading to a different absorber performance degradation for the different operating temperatures. This difference is less evident for the PC st. because the weight of thermal emittance, in terms of performance, is fixed to 0.5 (eq. 7.5), leading to have an almost equal PC st. for all the considered operating temperature (circles with dashed lines). The relative weight of thermal emittance, in terms of performance, is taken in account from PC_η (section 7.1), leading to have a more distinguishable absorber performance degradation behavior for the considered operating temperatures (squares with solid lines).

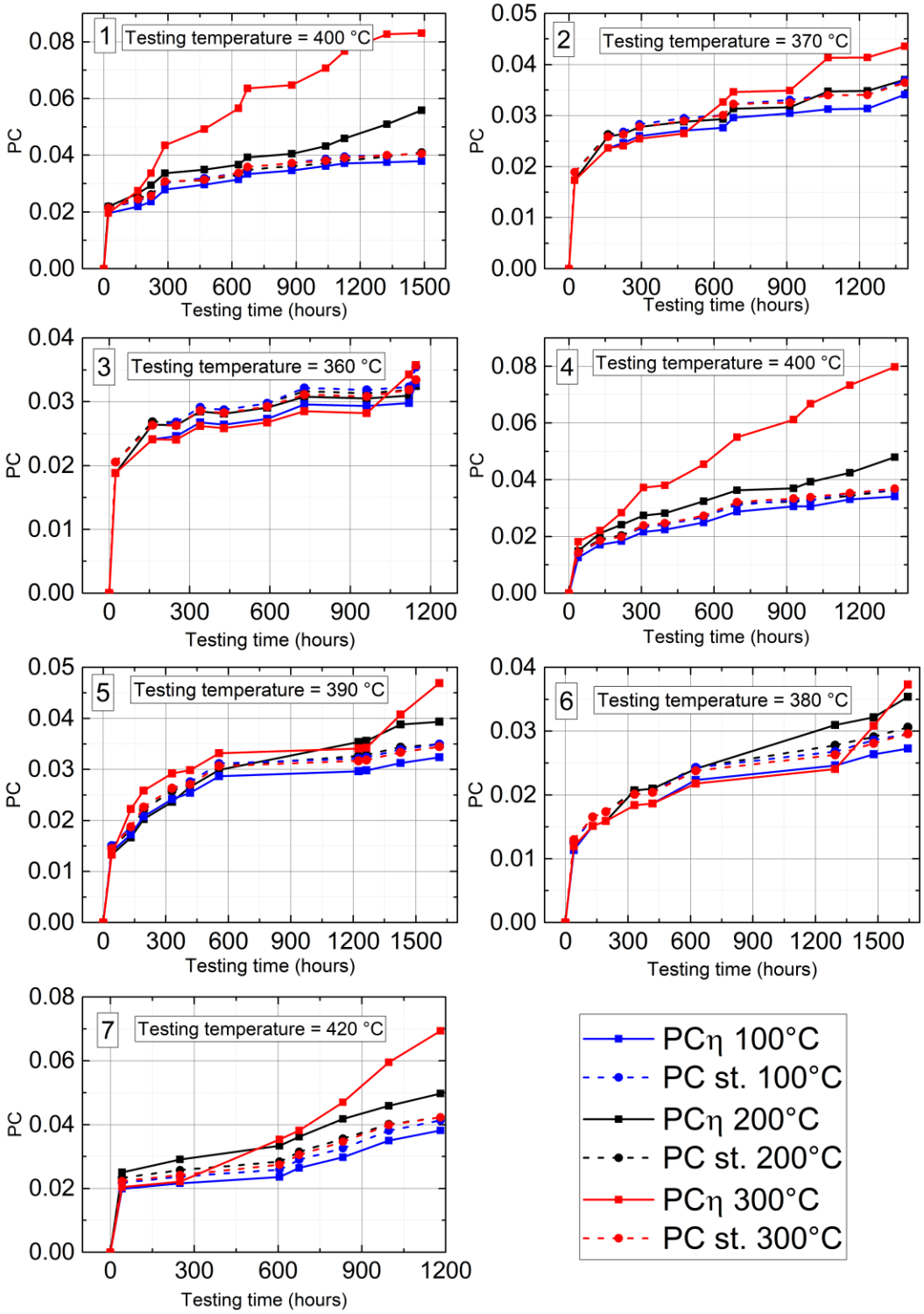

Figure 7.11. Standard (PC st.) (circles) and proposed (PC_η) (squares) performance criterion at 100, 200 and 300°C (blue, black and red respectively) for the 7 thermal aging tests.

Thanks to these data we are able to calculate the activation energy for the Mirotherm® that describe the aging process in vacuum environment for 3 different operating temperatures. The E_T calculation strictly depends on the considered performance criterion as described from eq. 7.18, for this reason we obtain different energy activation for the PC st. and PC_η. The evaluated E_T considering PC st. (E_T-st.) and PC_η (E_T-η) for the 3 different operating temperatures are reported in table 7.2 and fig. 7.12.

Table 7.2. Activation energy with PC st. and PC_η for 100, 200 and 300°C operating temperature.

Operating Temperature (°C)	E_T-st. (kJ/mol)	E_T-η (kJ/mol)
100	57	55
200	59	77
300	65	120

The E_T showed is the average of the 20 combinations obtained matching 2-by-2 the equation 7.18 for the 7 different tests, as explained above. The figure 7.12 clearly shows the light dependence from the operating temperature of the E_T-st., this happen because PC st. is almost equal for the 3 considered operating temperatures. The E_T-st. temperature dependence is due to smaller variation of the thermal emittance as the operating temperature increases. Indeed, the E_T-η presents a larger temperature dependence, mainly due to the relative weight given to the absorptance and thermal emittance. For the Mirotherm®, as reported in figure 7.10, the absorptance is the most critical factor, because the thermal emittance observes small variations. The weight of absorptance is lower and consequently the E_T-η increase, increasing the operating temperature. The E_T-η points out that the changes in absorber performance are temperature dependent and for this reason the aging process have to be described with different activation energy for different operating temperatures.

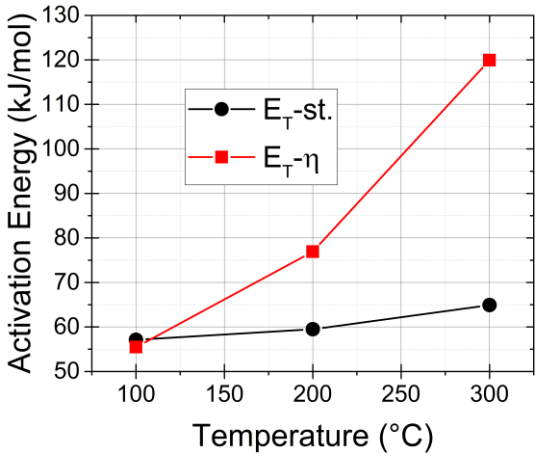

Figure 7.12. E_T-st. (black circles) and E_T-η (red squares) for 100, 200 and 300°C operating temperature.

Moreover, as described in section 7.1, the PC_η is equally effective to PC st., if we consider 90 °C as absorber working temperature, and this is confirmed by the almost equal E_T at 100°C. In conclusion, the E_T-η results to be a more realist way to predict the absorber behavior, because is able to consider the performance absorber changes for the different operating temperatures, giving the exact relative weight to the absorptance and thermal emittance.

7.4 Service lifetime calculation with standard and novel procedure

The large difference in the E_T (fig. 7.12) can strongly affect the service lifetime calculation for an absorber working at operating temperatures higher than 100 °C. Multiplying the equation 7.2 by the service lifetime (t_{LT}) we obtain:

$$k\, t_{LT} = t_{LT}\, D_{Arrh}\, exp\left(-\frac{E_T}{R\,T}\right) \tag{7.19}$$

Where $k\, t_{LT}$ is the performance criterion limit (PC_{LIM}), that represents the maximum acceptable degradation in terms of performance that can occur during the absorber lifetime, in other words it represents how much the chosen PC can change. The current standard establishes a value for PC_{LIM} of 0.05, meaning that the absorber performance can decrease of a maximum of 5% to consider the absorber in good working conditions. From equation 7.19 is possible to calculate the service lifetime as:

$$t_{LT} = \frac{PC_{LIM}}{D_{Arrh}\, exp\left(-\frac{E_T}{R\,T}\right)} \tag{7.20}$$

Where PC_{LIM} is fixed to 0.05, D_{Arrh} and E_T were already calculated (section 7.3), and T is replaced by the effective constant temperature (T_{eff}) that produces the same aging effect than the real $f(T)$ as described in section 7 and 7.2.

To calculate the service lifetime for the Mirotherm®, following the standard procedure (t_{LT}-st.), the E_T-st. was used and the T_{eff} was computed from equation 7.3 using the re-scaled $f(T)$ for an absorber with 300 °C of stagnation temperature (fig 7.4 in section 7.2). The T_{eff} values slightly depend on the E_T-st., as expected from equation 7.3, and they are 185, 187 and 192 °C for 57, 59, 65 E_T-st. respectively. The t_{LT}-st. results are reported in figure 7.13. The figure clearly shows how the t_{LT}-st. increase, increasing the absorber operating temperature. This result looks to be in the opposite way as expected, because increasing the operating temperature the absorber has more thermal stress, and consequently lower service lifetime. This happen because the standard procedure fixes the $f(T)$, based on the absorber stagnation temperature, without taking in account the real absorber operating temperature. The increase in service lifetime, fixing the $f(T)$, is explained both by the higher E_T-st. for higher operating temperature, and by the re-scaled $f(T)$ shape. For the re-scaled $f(T)$ most hours are concentrated before 100°C, for this reason the re-scaled $f(T)$ could be reasonable only for an operating temperature of 100 °C, and consequently t_{LT}-st. = 32 years for 100 °C operating temperature, is the only acceptable value obtained from standard procedure.

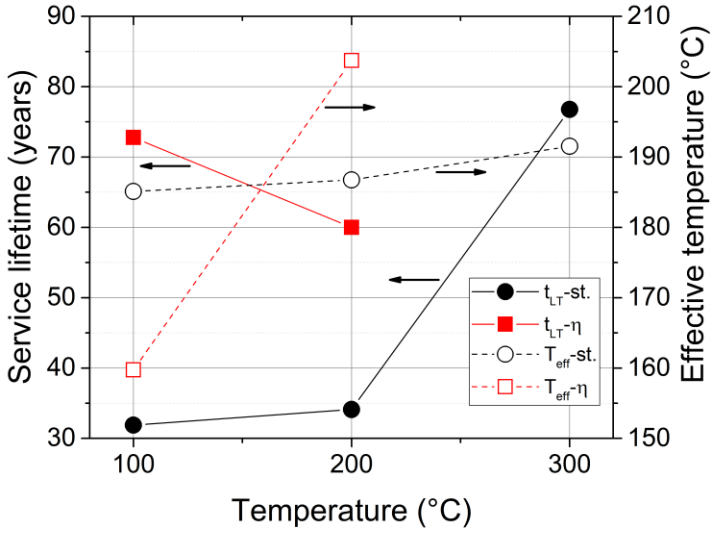

Figure 7.13. Left axis: Service lifetime following the standard (black circles) and the novel (red squares) procedure for 100, 200 and 300°C operating temperature; Right axis: Effective temperatures following the standard (black open circles) and the novel (red open squares) procedure for 100, 200 and 300°C operating temperature.

To understand how the different E_T and $f(T)$ impact the service lifetime calculation, the t_{LT} was calculated also following the novel procedure (t_{LT}-η). The T_{eff} used in this calculation is derived from equation 7.3 using the $f(T)$ reported in figure 7.9, obtained using the simulation model, for 100 and 200 °C operating temperature and with and 30 stagnation days. The results are reported in fig. 7.13, compared with t_{LT}-st., the stagnation length was chosen because the standard $f(T)$ consider the same stagnation period length. Using the novel procedure, the t_{LT}-η decrease, increasing the operating temperature, from 73 years to 60 years for 100 and 200 °C operating temperature respectively. The two-procedure lead to obtain very different results. About the 100 °C operating temperature results, we have very similar E_T (E_T-η = 55 kJ/mol, E_T-st = 57 kJ/mol), but the different shape of $f(T)$ allows to have a different T_{eff}, and consequently a different t_{LT} value. In this case, the $T_{eff}^{100°C}$ evaluated following the novel procedure ($T_{eff}^{100°C}$-η = 160 °C), is lower compared with the one obtained from standard procedure ($T_{eff}^{100°C}$-st. = 185 °C), because most of the hours of the novel $f(T)$ (fig. 7.9a) are concentrated before 100 °C, and for this reason the $t_{LT}^{100°C}$-η (73 years) is higher than $t_{LT}^{100°C}$-st. (32 years). Indeed, about the 200 °C operating temperature results, in this case, the $T_{eff}^{200°C}$-η (204 °C) is higher than $T_{eff}^{200°C}$-st. (187 °C), because the novel $f(T)$ (fig. 7.9b) presents most of the hours around 200 °C, while the re-scaled $f(T)$ (fig 7.4) have a very little amount of hours at high temperatures. The huge increase in the T_{eff}- η (from 160 to 204 °C, for 100 and 200 °C operating temperature), leads to obtain a decrease in the t_{LT}-η, despite the increase of the E_T-η ($E_T^{100°C}$-η = 55 kJ/mol, $E_T^{200°C}$-η = 77 kJ/mol). But, thanks to E_T-η increase, the t_{LT}-η values don't decrease drastically, otherwise the t_{LT}-η would have reached very

low values, leading to an unrealistic prediction of service lifetime. The t_{LT}-η trend, with a decrease, increasing the operating temperatures, looks to be more reasonable compared to the t_{LT}-st. trend.

These results suggest that the standard procedure looks to make an error in both E_T and $f(T)$. The re-scaled $f(T)$ could leads to a too high T_{eff} for the 100 °C operating temperature case, but to a too low T_{eff} for the 200 °C operating temperature case, demonstrating that assuming only one $f(T)$ for the different operating temperature result in a huge error in the service lifetime calculation. On the other hand, also not considering the relative weight of absorptance and thermal emittance, during E_T estimation, leads to a large error in the service lifetime calculation. For this reason, the novel procedure looks to be a more realistic way to predict the service lifetime for absorber working in HVFPCs.

The service lifetime calculation, following the novel procedure, was made also considering 0-10-20 stagnation days, and the results are summarized in fig. 7.14. The T_{eff} values are strongly affected by the stagnation length, as explained in section 7.2, and consequently the t_{LT}-η decrease, increasing the stagnation days.

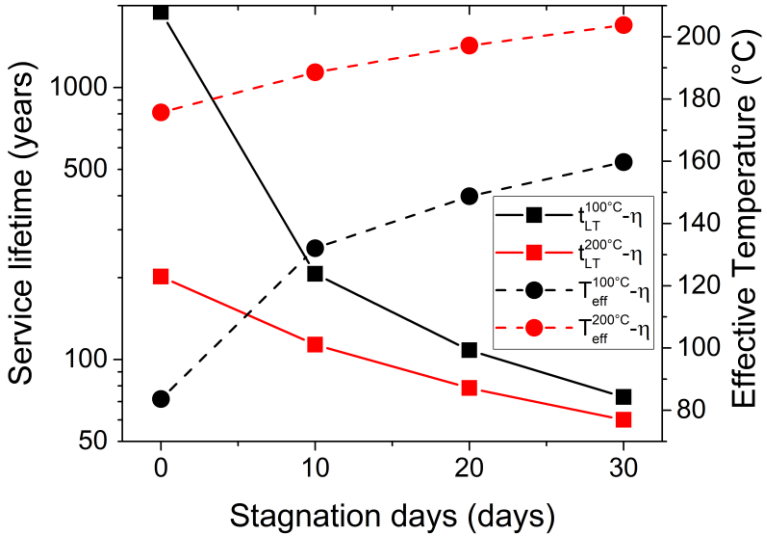

Figure 7.14. Left axis: Service lifetime following the novel procedure for 100 (black squares) and 200°C (red squares) operating temperature; Right axis: Effective temperatures following the novel procedure for 100 (black circles) and 200°C (red circles) operating temperature.

The results clearly show the strong impact that different E_T and $f(T)$ can have on the service lifetime calculation. As previously discussed (section 7.1 and 7.3), The E_T can be calculated thanks to the evaluation of the PC trend during different thermal aging tests, for this reason, is very important to define a correct performance criterion, in order to obtain a more realist energy activation that is able to better describe the absorber aging process. In this work we proposed a novel definition of the performance criterion ($PC_\eta(T)$ in section 7.1), that results to be a better parameter to describe the change in absorber performance during thermal aging test, because is

able to adapt the relative weight of absorptance and thermal emittance, depending on absorber working temperature, and also take in account the influence of the substrate thermal radiation losses. Indeed, the $PC_{\eta}(T)$ is equally effective to standard PC, if we consider 90 °C as absorber working temperature but enlarge the application also to high absorber working temperature, making the $PC_{\eta}(T)$ a more precise and versatile criterion. Moreover, figures 7.13 and 7.14 show how different operating temperatures can strongly impact on the service lifetime calculation. This happen because in equation 7.20, the effective constant temperature (T_{eff}) is influenced by the temperature frequency function, $f(T)$, that is not the same for the different operating temperatures. Furthermore, the $f(T)$ can be affected also by different technologies (standard solar collectors, HVFPCs, evacuated tubes collectors, etc) and location, for this reason, is very important to define correctly the $f(T)$ to obtain the exact T_{eff}. In this work we proposed to evaluate the $f(T)$ using a simulation model able to take in account the different location and operating temperatures for HVFPCs technologies (section 7.2). The $f(T)$, evaluate thanks to this simulation model, results to be more precise, versatile, and realistic compared to the one proposed by the standard (fig. 7.4).

Summarizing, to correctly predict the service lifetime of an absorber, the most precise definition of the activation energy (E_T) and of the effective constant temperature (T_{eff}) is mandatory. Consequently, the definition of a performance criterion (PC) and a temperature frequency function ($f(T)$) able to better describe the absorber behaviour during the time is necessary. For this reason, in this work the current standard, used to calculate the absorber service lifetime for standard collector working in air at low temperature, was revised, and a novel and more versatile procedure was proposed in order to obtain a more realist prevision of the service lifetime for absorber working in HVFPCs. The novel PC definition ($PC_{\eta}(T)$ in section 7.1) can automatically take in account the absorber working temperature, changing the relative weight of absorptance and thermal emittance, while the novel proposed way to calculate $f(T)$ (section 7.2) can take in account different location and operating temperatures for HVFPCs technologies. In conclusion, the revised procedure is able to better predict the absorber behaviour during the time for different operating temperatures and location for HVFPCs, and it could be easily adapted also for new emerging technologies.

8. Conclusions

Many optical applications require spectral selectivity, including solar absorption, high-temperature radiation, hyperspectral sensors, and optical communications. Although many new materials have been developed, often their properties and/or production costs do not favor their use. The main purpose of this work is to increase the flexibility of optical materials by including periodic or more complex structures to obtain the desired functionality, but also to maintain a low production cost and a design that is reproducible on a large scale. In this work, we considered the problem of reducing losses for solar devices to improve their overall efficiencies. The concept investigated was to introduce selective coatings to improve the solar conversion efficiency in thermal or thermo-photovoltaic (TPV) devices. Moreover, the prediction of the service lifetime of solar absorbers for High Vacuum Flat Plate Collector (HVFPC) was investigated, in order to obtain a more realistic prediction for this type of collector.

The High Vacuum Flat Plate Collector (HVFPC) is the new frontier to renewably produce industrial process heat in the mid-temperature range 100 °C – 200 °C. To improve the solar conversion efficiency, the development of an optimize solar selective absorber (SSA) and the reduction of the SSA's substrate radiative losses has been proposed. The optimized selective solar absorber presented in the thesis is a five-layer structure on copper substrate based on sputter deposited chromium oxide and chromium metal ($Cr/Cr_2O_3/Cr/Cr_2O_3/SiO_2$). For this coating the optimization algorithm is developed aiming at obtaining multilayer SSA suitable for a mass industrial production. To guarantee the best result the efficiency of the real coating is used as the fitness function of the optimization algorithm. The algorithm incorporates as a binding parameter the robustness of the coating in terms of efficiency loss when errors on layer thickness are made. Two coatings are designed to obtain the highest efficiency at 200 °C and 300 °C operating temperature while having a small sensitivity to thickness variations. Results of the optimization procedure predict an overall efficiency of the proposed SSAs in a HVFPC as high as 0.74 and 0.56 at 200 °C and 300 °C, respectively. Efficiency loss is less than 2 percentage points if the layer thickness variation is less than 20%. The optimized SSAs were fabricated via sputtering depositions on optically smooth samples. The deposited samples have been characterized via optical analysis, showing excellent results, in agreement to the simulation. Short duration high temperature thermal stability tests of the fabricated absorbers delivered encouraging results on the resistance of the coating to high operating temperatures.

The HVFPC performances would benefit from a substrate thermal emittance reduction. Such reduction could be obtained with a better finishing of the back side of the aluminum substrate or using a substrate with a lower thermal emittance (such as copper or silver). A simple yet effective way to enhance the performances of this solar absorber could be to deposit low emissive coating (LEC) of copper or silver (thermal emittance ≈ 0.02) on the back side of the absorber, on the aluminum surface. To test the properties of the copper or silver coating on the aluminum a Cu and Ag coating was deposited via electron beam deposition technique on aluminum bulk substrates on one side or both sides. A 25% thermal emittance reduction can be observed for the one side coated

samples, while a 50% reduction can be observed for the double side Cu coated sample. The best result is obtained with the double side Ag coated samples, with a thermal emittance reduction of 60-65%. The thermal stability test demonstrated the necessary to have a diffusion barrier to preserve the benefits of the LECs also at high temperatures (up to 360 °C). The overall efficiency of an optimized selective coating on aluminum substrate with diffusion barrier and low emissive coating at 200 °C increases from 0.64 up to 0.72, with 13% enhancement in performances, and the stagnation temperature increases of about 30 °C. It is worth to note that the advantages of the low emissive coating increase with increasing temperature, in fact at 300 °C the overall efficiency increase from 0.19 to 0.37, having an almost doubled enhancement in performances.

Instead, the development and use of selective emitters (SE) could play a key role in increasing the efficiency of TPV devices and in reducing heat losses. TPV systems represent one of the newest technologies to direct convert the thermal radiation emitted from an object heated at temperatures typically higher than 1000 K into electricity. During my abroad period at Purdue University - Electrical & Computer Engineering - Birck Nanotechnology Center (West Lafayette, IN, USA), the optimization, development, and realization of selective emitters has been studied. The proposed SE was fabricated via sputtering deposition and made of SiN_x, SiO_2, and TiO_2 on a W substrate. The SE emissivity spectrum was simulated, by means of the transfer matrix method, starting from experimentally evaluated refractive indices. Through a genetic algorithm, its efficiency is optimized for a chosen operating temperature of 1000 °C and an extended range of bandgap energies, i.e. from 0.55 to 0.72 eV, to ensure proper functioning with most of the commonly used PV cells for Solar-TPV systems (semiconductors of the III-V groups). The deposited sample behaves very similarly to what was expected from simulations, reaching a maximum efficiency of 50% at 0.63 eV (at 1000 °C). Its thermal stability was demonstrated after a long thermal stress test carried out in a vacuum furnace at 1000 °C: its efficiency only slightly decreased, reaching 46%. For a more reliable analysis of the SE properties, the refractive indices of the materials involved in the design were measured at various temperatures, from room temperature up to 1000 °C. Hence, a new simulation was performed, and the results showed an efficiency equal to 44%. In addition, the behavior of a realistic PV cell exposed to the fabricated SE was also simulated: the results show a maximum efficiency of 15% at 1000 °C and the possibility of reaching an efficiency of 25% at 1600 °C, exceeding the theoretical limit of Shockley-Quisser. In conclusion, the proposed structure demonstrated high efficiency, thermal stability up to 1000 °C and versatility, as it can efficiently operate in the energy bandgap range of 0.55 to 0.72 eV.

The last part of this Ph.D. thesis was concentrated on the elaboration of a novel procedure for the prediction of the service lifetime of solar absorbers for HVFPCs. The current standard is developed for standard collector working in air at low temperature, and it cannot be used also for HVPCs. The Performance Criterion (PC), that represent the degree of aging of a coating, the temperature frequency function $f(T)$, that represents how many hours the absorber is at temperature T during one-year operation, and the procedure flow were revised and adapted to be suitable to evaluate the service lifetime of solar absorbers for HVFPCs. The proposed performance criterion ($PC_\eta(T)$),

given by the difference in the overall efficiency of the virgin and after test absorbers, results to be a better parameter to describe the change in absorber performance during thermal aging test, because is able to adapt the relative weight of absorptance and thermal emittance, depending on absorber working temperature, and also take in account the influence of the substrate thermal radiation losses. Indeed, the $PC_\eta(T)$ is equally effective to standard PC, if we consider 90 °C as absorber working temperature but enlarge the application also to high absorber working temperature, making the $PC_\eta(T)$ a more precise and versatile criterion. Instead, the $f(T)$ presented by the standard, is a fixed function for any location and operating temperatures. For this reason, a dynamic simulation to build the absorber temperature history in operating conditions is presented. The results show clearly that there is a difference in the evaluation of the $f(T)$ following the current standard and using the simulation model with any operating temperature considered. This difference leads to a different effective temperature calculated value, and consequently to a different failure time. For this reason, the use of the simulation model to predict the $f(T)$ for HVFPCs is more reasonable. Thanks to the simulation model, the $f(T)$ trend in different location and for different operating temperature can be investigated. The final results, using the novel proposed performance criterion and $f(T)$, lead to a very different service lifetime calculation compared with the standard procedure. The service lifetime calculated with the novel procedure looks to be more reasonable because it decreases, increasing the operating temperature, from 73 years to 60 years for 100 and 200 °C operating temperature respectively, instead the one obtained from standard procedure goes in the opposite way (32, 34 and 76 years for 100, 200 and 300 °C operating temperature respectively).

Summarizing, the results of the study conducted during this Ph.D. program present for both selective solar absorbers and selective emitters, a simple and cost-effective solution, which is easily reproducible on a large-scale production and used daily in industrial applications. The proposed improvement could allow the HVFPCs to produce heat up to 300 °C with high efficiency. Currently the range of mid-high temperature (150 - 400 °C) heat represents the 22% of the worldwide heat request [9] but is not very well covered by the renewable source. This Ph.D. thesis could represent the starting point for the transition from fossil fuel to renewable energy also for the mid-high temperature applications. The multi-layered structures proposed for both solar selective coatings and selective emitters avoid complex techniques, the choice of materials inexpensive and easy to handle. The sputtering techniques is widely demonstrated to be a very cost effective solution [163,164] and multi-layered sputtered structures result to be more sustainable on a cost approach than other techniques (e.g. electrochemical deposition) [165]. Currently, this technique is one of the most used to produce a large number of devices and represents the best choice to implement on a large scale the proposed solutions. In fact, this work represents the first step towards the broader, industrial development of these elements, where all the aforementioned characteristics are fundamental. The proposed solutions could allow the production of abundant renewable energy and the mismatch between available and demanded energy could represent a problem. For this reason, the energy storage is a critical challenge to manage intermittent renewable energies. The thermal energy storage is one of the most attractive energy storage

solutions since the energy storage efficiency of the thermal storage system can reach 95%-97%. The commonly used materials are usually listed into three categories: sensible heat storage (e.g water, air, oil, rocks, brine, concrete, sand, and soil), latent heat storage (e.g. organic, inorganic, eutectics, and low melting point metals), and thermochemical heat storage (e.g. sorption and thermochemical) [166]. About the latent heat storage, one of the most attractive solutions are the PCM materials. Their efficiency as thermal storage is widely demonstrated [167–169] and their optimization and cost analysis was also investigated [170]. Anyway, the thermal energy storage represents a valid option for continuous power production and to shift the solar energy of peak sunshine hours to peak consumption hours, and for this reason a massive and comprehensive research have to be implemented.

Moreover, a novel procedure for HVFPCs (easily adaptable also for new emerging technologies) able to better predict the service lifetime for different operating temperatures and location for HVFPCs is presented. All the results presented above could certainly play a key role in increasing and expansion of the solar energy market and they will ultimately benefit our planet and our health.

9. Future developments

Experimental measurements of the investigated selective coatings show that thermal emittance of the multilayers deposited on bulk substrate is higher than expected from simulations (simulation are for smooth samples). A possible source of such increase could be due to factors like the influence of the surface roughness or in the presence of copper oxides at the interface between the substrate and the multilayer. So, in future works the origin of the increased emittance should be investigated, allowing to further improve the SSA performances.

Thermal stability is a rather important parameter for selective solar absorbers because a stable absorber guarantees its performances all along its service lifetime: even if literature and preliminary experimental tests showed encouraging results in terms of thermal stability for the selective coatings developed in this work, a detailed and accurate study of the aging mechanisms which are characteristic of the fabricated selective absorbers should be provided. The novel proposed procedure will be applied on the developed coating and their service lifetime will be calculated.

A comprehensive study about the thermal energy storage, its applications to solar fields and the development and optimization of novel solutions have to be realized.

The correct measurement of the Performance Criterion will be mandatory and for this purpose, the enhance of optical properties measurements is necessary. In particular we will focus on the improvement of MTB apparatus, leading to a higher sensibility to obtain more precise thermal emittance measurements.

Moreover, an economic study on the energy production losses for a HVFPCs field, considering the selective solar absorber aging degradation could be necessary to define a more precise Performance Criterion limit.

Bibliography

[1] A. Sayigh, Renewable energy — the way forward, Appl. Energy. 64 (1999) 15–30. https://doi.org/10.1016/S0306-2619(99)00117-8.

[2] A. Shahsavari, M. Akbari, Potential of solar energy in developing countries for reducing energy-related emissions, Renew. Sustain. Energy Rev. 90 (2018) 275–291. https://doi.org/10.1016/j.rser.2018.03.065.

[3] M. Meinshausen, N. Meinshausen, W. Hare, S.C.B. Raper, K. Frieler, R. Knutti, D.J. Frame, M.R. Allen, Greenhouse-gas emission targets for limiting global warming to 2°C, Nature. 458 (2009) 1158–1162. https://doi.org/10.1038/nature08017.

[4] L. Kranzl, M. Hartner, A. Müller, G. Resch, S. Fritz, T. Fleiter, A. Herbst, M. Rehfeldt, P. Manz, A. Zubaryeva, HOTMAPS 2030/2050 SCENARIOS FOR THE HEATING AND COOLING SECTORS, 2018. https://www.hotmaps-project.eu/hotmaps-2030-2050-scenarios-for-the-heating-and-cooling-sectors/.

[5] T. Fleiter, R. Elsland, M. Rehfeldt, J. Steinbach, U. Reiter, G. Catenazzi, M. Jakob, C. Rutten, R. Harmsen, F. Dittmann, P. Rivière, P. Stabat, Profile of heating and cooling demand in 2015, 2017. https://heatroadmap.eu/wp-content/uploads/2018/11/HRE4_D3.1.pdf.

[6] C. Lauterbach, B. Schmitt, U. Jordan, K. Vajen, The potential of solar heat for industrial processes in Germany, Renew. Sustain. Energy Rev. 16 (2012) 5121–5130. https://doi.org/10.1016/j.rser.2012.04.032.

[7] ANNUAL ENERGY OUTLOOK 2022, 2022. https://www.eia.gov/outlooks/aeo/.

[8] Tracking Clean Energy Progress, 2023. https://www.iea.org/topics/tracking-clean-energy-progress.

[9] PERSPECTIVES FOR THE ENERGY TRANSITION, (2017). https://www.irena.org/-/media/Files/IRENA/Agency/Publication/2017/Mar/Perspectives_for_the_Energy_Transition_2017.pdf.

[10] National Renewable Energy Laboratory, (2023). https://www.nrel.gov/research/re-solar.html.

[11] S.C. Bhatia, ed., Advanced Renewable Energy Systems, (Part 1 and 2), WPI Publishing, 2014. https://doi.org/10.1201/b18242.

[12] C.B. Eaton, H.A. Blum, The use of moderate vacuum environments as a means of increasing the collection efficiencies and operating temperatures of flat-plate solar collectors, Sol. Energy. 17 (1975) 151–158. https://doi.org/10.1016/0038-092X(75)90053-5.

[13] TVP Solar, (2023). https://www.tvpsolar.com/.

[14] A. Buonomano, F. Calise, M.D. D'Accadia, G. Ferruzzi, S. Frascogna, A. Palombo, R. Russo, M. Scarpellino, Experimental analysis and dynamic simulation of a novel high-temperature solar cooling system, Energy Convers. Manag. 109 (2016) 19–39. https://doi.org/10.1016/j.enconman.2015.11.047.

[15] R.W. Moss, P. Henshall, F. Arya, G.S.F. Shire, T. Hyde, P.C. Eames, Performance and operational effectiveness of evacuated flat plate solar collectors compared with conventional thermal, PVT and PV panels, Appl. Energy. 216 (2018) 588–601. https://doi.org/10.1016/j.apenergy.2018.01.001.

[16] C.E. Kennedy, Review of Mid- to High-Temperature Solar Selective Absorber Materials, Golden, CO, 2002. https://doi.org/10.2172/15000706.

[17] P. Bermel, J. Lee, J.D. Joannopoulos, I. Celanovic, M. Soljacie, SELECTIVE SOLAR ABSORBERS, Annu. Rev. Heat Transf. 15 (2012) 231–254. https://doi.org/10.1615/AnnualRevHeatTransfer.2012004119.

[18] H.C. Barshilia, P. Kumar, K.S. Rajam, A. Biswas, Structure and optical properties of AgAl2O3 nanocermet solar selective coatings prepared using unbalanced magnetron sputtering, Sol. Energy Mater. Sol. Cells. 95 (2011) 1707–1715. https://doi.org/10.1016/j.solmat.2011.01.034.

[19] E. Wäckelgård, A. Mattsson, R. Bartali, R. Gerosa, G. Gottardi, F. Gustavsson, N. Laidani, V. Micheli, D. Primetzhofer, B. Rivolta, Development of W-SiO2and Nb-TiO2 solar absorber coatings for combined heat and power systems at intermediate operation temperatures, Sol. Energy Mater. Sol. Cells. 133 (2015) 180–193. https://doi.org/10.1016/j.solmat.2014.10.022.

[20] D. Dias, L. Rebouta, P. Costa, A. Al-Rjoub, M. Benelmeki, C.J. Tavares, N.P. Barradas, E. Alves, P. Santilli, K. Pischow, Optical and structural analysis of solar selective absorbing coatings based on AlSiOx:W cermets, Sol. Energy. 150 (2017) 335–344. https://doi.org/10.1016/j.solener.2017.04.055.

[21] J. Zhou, X. Chen, L.J. Guo, Efficient Thermal-Light Interconversions Based on Optical Topological Transition in the Metal-Dielectric Multilayered Metamaterials, Adv. Mater. 28 (2016) 3017–3023. https://doi.org/10.1002/adma.201505451.

[22] R. Sakakibara, V. Stelmakh, W.R. Chan, M. Ghebrebrhan, J.D. Joannopoulos, M. Soljačić, I. Čelanović, Practical emitters for thermophotovoltaics: a review, J. Photonics Energy. 9 (2019) 1. https://doi.org/10.1117/1.jpe.9.032713.

[23] T. Bauer, Thermophotovoltaics, Springer Berlin Heidelberg, Berlin, Heidelberg, 2011. https://doi.org/10.1007/978-3-642-19965-3.

[24] Y. Wang, H. Liu, J. Zhu, Solar thermophotovoltaics: Progress, challenges, and opportunities, APL Mater. 7 (2019). https://doi.org/10.1063/1.5114829.

[25] A. Datas, Optimum semiconductor bandgaps in single junction and multijunction

thermophotovoltaic converters, Sol. Energy Mater. Sol. Cells. 134 (2015) 275–290. https://doi.org/10.1016/j.solmat.2014.11.049.

[26] Z. Wang, D. Kortge, Z. He, J. Song, J. Zhu, C. Lee, H. Wang, P. Bermel, Selective emitter materials and designs for high-temperature thermophotovoltaic applications, Sol. Energy Mater. Sol. Cells. 238 (2022) 111554. https://doi.org/10.1016/j.solmat.2021.111554.

[27] Y. Wenming, C. Siawkiang, S. Chang, X. Hong, L. Zhiwang, Research on micro-thermophotovoltaic power generators with different emitting materials, J. Micromechanics Microengineering. 15 (2005). https://doi.org/10.1088/0960-1317/15/9/S11.

[28] L. Fraas, J. Samaras, J. Avery, L. Minkin, Antireflection coated refractory metal matched emitters for use with GaSb thermophotovoltaic generators, Conf. Rec. IEEE Photovolt. Spec. Conf. 2000-Janua (2000) 1020–1023. https://doi.org/10.1109/PVSC.2000.916059.

[29] V.M. Andreev, A.S. Vlasov, V.P. Khvostikov, O.A. Khvostikova, P.Y. Gazaryan, S. V. Sorokina, N.A. Sadchikov, Solar thermophotovoltaic converters based on tungsten emitters, J. Sol. Energy Eng. Trans. ASME. 129 (2007) 298–303. https://doi.org/10.1115/1.2734576.

[30] B. Bitnar, W. Durisch, J.C. Mayor, H. Sigg, H.R. Tschudi, Characterisation of rare earth selective emitters for thermophotovoltaic applications, Sol. Energy Mater. Sol. Cells. 73 (2002) 221–234. https://doi.org/10.1016/S0927-0248(01)00127-1.

[31] P.N. Dyachenko, S. Molesky, A.Y. Petrov, M. Störmer, T. Krekeler, S. Lang, M. Ritter, Z. Jacob, M. Eich, Controlling thermal emission with refractory epsilon-near-zero metamaterials via topological transitions, Nat. Commun. 7 (2016). https://doi.org/10.1038/ncomms11809.

[32] B.J. Lee, C.J. Fu, Z.M. Zhang, Coherent thermal emission from one-dimensional photonic crystals, Appl. Phys. Lett. 87 (2005) 1–4. https://doi.org/10.1063/1.2010613.

[33] V. Rinnerbauer, A. Lenert, D.M. Bierman, Y.X. Yeng, W.R. Chan, R.D. Geil, J.J. Senkevich, J.D. Joannopoulos, E.N. Wang, M. Soljačić, I. Celanovic, Metallic Photonic Crystal Absorber-Emitter for Efficient Spectral Control in High-Temperature Solar Thermophotovoltaics, Adv. Energy Mater. 4 (2014) 1400334. https://doi.org/10.1002/aenm.201400334.

[34] M. Garín, D. Hernández, T. Trifonov, R. Alcubilla, Three-dimensional metallo-dielectric selective thermal emitters with high-temperature stability for thermophotovoltaic applications, Sol. Energy Mater. Sol. Cells. 134 (2015) 22–28. https://doi.org/10.1016/j.solmat.2014.11.017.

[35] M. Suemitsu, T. Asano, M. De Zoysa, S. Noda, Wavelength-selective thermal emitters using Si-rods on MgO, Appl. Phys. Lett. 112 (2018) 1–5. https://doi.org/10.1063/1.5010805.

[36] K. Cui, P. Lemaire, H. Zhao, T. Savas, G. Parsons, A.J. Hart, Tungsten–Carbon Nanotube

Composite Photonic Crystals as Thermally Stable Spectral-Selective Absorbers and Emitters for Thermophotovoltaics, Adv. Energy Mater. 8 (2018) 1–9. https://doi.org/10.1002/aenm.201801471.

[37] H. Sai, H. Yugami, Y. Kanamori, K. Hane, Solar selective absorbers based on two-dimensional W surface gratings with submicron periods for high-temperature photothermal conversion, Sol. Energy Mater. Sol. Cells. 79 (2003) 35–49. https://doi.org/10.1016/S0927-0248(02)00364-1.

[38] N. Jeon, J.J. Hernandez, D. Rosenmann, S.K. Gray, A.B.F. Martinson, J.J. Foley IV, Pareto Optimal Spectrally Selective Emitters for Thermophotovoltaics via Weak Absorber Critical Coupling, Adv. Energy Mater. 8 (2018) 1–9. https://doi.org/10.1002/aenm.201801035.

[39] M. Chirumamilla, G.V. Krishnamurthy, K. Knopp, T. Krekeler, M. Graf, D. Jalas, M. Ritter, M. Störmer, A.Y. Petrov, M. Eich, Metamaterial emitter for thermophotovoltaics stable up to 1400 °C, Sci. Rep. 9 (2019) 7241. https://doi.org/10.1038/s41598-019-43640-6.

[40] M. Shimizu, A. Kohiyama, H. Yugami, Evaluation of thermal stability in spectrally selective few-layer metallo-dielectric structures for solar thermophotovoltaics, J. Quant. Spectrosc. Radiat. Transf. 212 (2018) 45–49. https://doi.org/10.1016/j.jqsrt.2018.02.037.

[41] A. Kohiyama, M. Shimizu, H. Yugami, Unidirectional radiative heat transfer with a spectrally selective planar absorber/emitter for high-efficiency solar thermophotovoltaic systems, Appl. Phys. Express. 9 (2016) 112302. https://doi.org/10.7567/APEX.9.112302.

[42] B. Carlsson, K. Moeller, U. Frei, M. Koehl, Accelerated life testing of solar absorber coatings, in: V. Wittwer, C.G. Granqvist, C.M. Lampert (Eds.), 1994: pp. 79–90. https://doi.org/10.1117/12.185359.

[43] The Electromagnetic Spectrum, (2016). https://www.miniphysics.com/electromagnetic-spectrum_25.html.

[44] M. Fox, Optical Properties of Solids, 2010.

[45] E. Hecht, Optics, 4th ed., Addison-Wesley, 2001.

[46] F.P. INCROPERA, D.P. DEWITT, T.L. BERGMAN, A.S. LAVINE, Fundamentals of Heat and Mass Transfer, 6th ed., John Wiley & Sons, 2006.

[47] M. Planck, On the Law of the Energy Distribution in the Normal Spectrum, Ann. Phys. 4 (1901) 553.

[48] M.J. Riedl, Optical Design Fundamentals for Infrared Systems, Second Edition, SPIE, 2001. https://doi.org/10.1117/3.412729.

[49] Standard Tables for Reference Solar Spectral Irradiances: Direct Normal and Hemispherical on 37° Tilted Surface, in: 2020: p. 21. https://doi.org/10.1520/G0173-

03R20.

[50] L. Evangelisti, R. De Lieto Vollaro, F. Asdrubali, Latest advances on solar thermal collectors: A comprehensive review, Renew. Sustain. Energy Rev. 114 (2019) 109318. https://doi.org/10.1016/j.rser.2019.109318.

[51] T. Kodama, High-temperature solar chemistry for converting solar heat to chemical fuels, Prog. Energy Combust. Sci. 29 (2003) 567–597. https://doi.org/10.1016/S0360-1285(03)00059-5.

[52] A. Stollo, T. Chiarappa, A. D'Angelo, A. Maccari, F. Matino, LCOE reduction for parabolic trough CSP: Innovative solar receiver with improved performance at medium temperature, in: 2016: p. 030034. https://doi.org/10.1063/1.4949086.

[53] M. Orosz, R. Dickes, Solar thermal powered Organic Rankine Cycles, in: Org. Rank. Cycle Power Syst., Elsevier, 2017: pp. 569–612. https://doi.org/10.1016/B978-0-08-100510-1.00016-8.

[54] F. Calise, M.D. D'Accadia, M. Vicidomini, M. Scarpellino, Design and simulation of a prototype of a small-scale solar CHP system based on evacuated flat-plate solar collectors and Organic Rankine Cycle, Energy Convers. Manag. 90 (2015) 347–363. https://doi.org/10.1016/j.enconman.2014.11.014.

[55] N. BENZ, T. BEIKIRCHER, HIGH EFFICIENCY EVACUATED FLAT-PLATE SOLAR COLLECTOR FOR PROCESS STEAM PRODUCTION, Sol. Energy. 65 (1999) 111–118. https://doi.org/10.1016/S0038-092X(98)00122-4.

[56] The Performance of Concentrated Solar Power (CSP) Systems, Elsevier, 2017. https://doi.org/10.1016/C2014-0-03695-7.

[57] Comprehensive Energy Systems, 2018.

[58] Future Energy, Elsevier, 2014. https://doi.org/10.1016/C2012-0-07119-0.

[59] C. Benvenuti, The SRB solar thermal panel, Europhys. News. 44 (2013) 16–18. https://doi.org/10.1051/epn/2013301.

[60] DIN CERTCO - Register-Nr. 011-7S1890 F, (n.d.). https://www.dincertco.tuv.com/registrations/60081291.

[61] P. Henshall, P. Eames, F. Arya, T. Hyde, R. Moss, S. Shire, Constant temperature induced stresses in evacuated enclosures for high performance flat plate solar thermal collectors, Sol. Energy. 127 (2016) 250–261. https://doi.org/10.1016/j.solener.2016.01.025.

[62] T. Beikircher, N. Benz, W. Spirkl, Gas Heat Conduction in Evacuated Flat-Plate Solar Collectors: Analysis and Reduction, J. Sol. Energy Eng. 117 (1995) 229–235. https://doi.org/10.1115/1.2847807.

[63] S.A. Sakhaei, M.S. Valipour, Performance enhancement analysis of The flat plate collectors: A comprehensive review, Renew. Sustain. Energy Rev. 102 (2019) 186–204.

https://doi.org/10.1016/j.rser.2018.11.014.

[64] B. Liu, C. Wang, S. Bazri, I.A. Badruddin, Y. Orooji, S. Saeidi, S. Wongwises, O. Mahian, Optical properties and thermal stability evaluation of solar absorbers enhanced by nanostructured selective coating films, Powder Technol. 377 (2021) 939–957. https://doi.org/10.1016/j.powtec.2020.09.040.

[65] R. Russo, M. Monti, F. di Giamberardino, V.G. Palmieri, Characterization of selective solar absorber under high vacuum, Opt. Express. 26 (2018) A480. https://doi.org/10.1364/OE.26.00A480.

[66] F. Cao, K. McEnaney, G. Chen, Z. Ren, A review of cermet-based spectrally selective solar absorbers, Energy Environ. Sci. 7 (2014) 1615. https://doi.org/10.1039/c3ee43825b.

[67] M. Bello, S. Shanmugan, Achievements in mid and high-temperature selective absorber coatings by physical vapor deposition (PVD) for solar thermal Application-A review, J. Alloys Compd. 839 (2020) 155510. https://doi.org/10.1016/j.jallcom.2020.155510.

[68] C.M. Lampert, Coatings for enhanced photothermal energy collection I. Selective absorbers, Sol. Energy Mater. 1 (1979) 319–341. https://doi.org/10.1016/0165-1633(79)90001-7.

[69] M. Okuyama, K. Saji, T. Adachi, H. Okamoto, Y. Hamakawa, Selective absorber using glow-discharge amorphous silicon for solar photothermal conversion, Sol. Energy Mater. 3 (1980) 405–413. https://doi.org/10.1016/0165-1633(80)90029-5.

[70] A. Donnadieu, B.O. Seraphin, Optical performance of absorber-reflector combinations for photothermal solar energy conversion, J. Opt. Soc. Am. 68 (1978) 292. https://doi.org/10.1364/JOSA.68.000292.

[71] C. D'Alessandro, D. de Maio, D. de Luca, E. di Gennaro, M. Gioffrè, M. Iodice, M. Musto, G. Rotondo, D. Dalena, R. Russo, Solar Selective Coating for Thermal Applications, Key Eng. Mater. 813 (2019) 316–321. https://doi.org/10.4028/www.scientific.net/KEM.813.316.

[72] N.P. Sergeant, O. Pincon, M. Agrawal, P. Peumans, Design of wide-angle solar-selective absorbers using aperiodic metal-dielectric stacks, Opt. Express. 17 (2009) 22800. https://doi.org/10.1364/OE.17.022800.

[73] F. Cao, D. Kraemer, T. Sun, Y. Lan, G. Chen, Z. Ren, Enhanced Thermal Stability of W-Ni-Al 2 O 3 Cermet-Based Spectrally Selective Solar Absorbers with Tungsten Infrared Reflectors, Adv. Energy Mater. 5 (2015) 1401042. https://doi.org/10.1002/aenm.201401042.

[74] M.H. Huang, S. Mao, H. Feick, H. Yan, Y. Wu, H. Kind, E. Weber, R. Russo, P. Yang, Room-Temperature Ultraviolet Nanowire Nanolasers, Science (80-.). 292 (2001) 1897–1899. https://www.jstor.org/stable/3083931.

[75] J. Zhu, Z. Yu, G.F. Burkhard, C.-M. Hsu, S.T. Connor, Y. Xu, Q. Wang, M. McGehee, S.

Fan, Y. Cui, Optical Absorption Enhancement in Amorphous Silicon Nanowire and Nanocone Arrays, Nano Lett. 9 (2009) 279–282. https://doi.org/10.1021/nl802886y.

[76] I. Celanovic, N. Jovanovic, J. Kassakian, Two-dimensional tungsten photonic crystals as selective thermal emitters, Appl. Phys. Lett. 92 (2008) 193101. https://doi.org/10.1063/1.2927484.

[77] P. Li, B. Liu, Y. Ni, K.K. Liew, J. Sze, S. Chen, S. Shen, Large-Scale Nanophotonic Solar Selective Absorbers for High-Efficiency Solar Thermal Energy Conversion, Adv. Mater. 27 (2015) 4585–4591. https://doi.org/10.1002/adma.201501686.

[78] F. Cverna, ed., ASM Ready Reference: Thermal Properties of Metals, ASM International, 2002.

[79] K. Zhang, L. Hao, M. Du, J. Mi, J.-N. Wang, J. Meng, A review on thermal stability and high temperature induced ageing mechanisms of solar absorber coatings, Renew. Sustain. Energy Rev. 67 (2017) 1282–1299. https://doi.org/10.1016/j.rser.2016.09.083.

[80] H.C. Barshilia, N. Selvakumar, K.S. Rajam, A. Biswas, Optical properties and thermal stability of TiAlN/AlON tandem absorber prepared by reactive DC/RF magnetron sputtering, Sol. Energy Mater. Sol. Cells. 92 (2008) 1425–1433. https://doi.org/10.1016/j.solmat.2008.06.004.

[81] K.D. Lee, Characterization of Cr-O Cermet Solar Selective Coatings Deposited by Using Direct-Current Magnetron Sputtering Technology, J. Korean Phys. Soc. 49 (2006) 187–194. https://www.jkps.or.kr/journal/download_pdf.php?spage=187&volume=49&number=1.

[82] Handbook of Physical Vapor Deposition (PVD) Processing, Elsevier, 2010. https://doi.org/10.1016/C2009-0-18800-1.

[83] D.R. Baer, S. Thevuthasan, Characterization of Thin Films and Coatings, in: Handb. Depos. Technol. Film. Coatings, Elsevier, 2010: pp. 749–864. https://doi.org/10.1016/B978-0-8155-2031-3.00016-8.

[84] ISASI – SciencesApp | Eduardo Caianiello, (n.d.). https://www.isasi.cnr.it/.

[85] H. Adachi, K. Wasa, Thin Films and Nanomaterials, in: Handb. Sputtering Technol., Elsevier, 2012: pp. 3–39. https://doi.org/10.1016/B978-1-4377-3483-6.00001-2.

[86] K. Strijckmans, R. Schelfhout, D. Depla, Tutorial: Hysteresis during the reactive magnetron sputtering process, J. Appl. Phys. 124 (2018) 241101. https://doi.org/10.1063/1.5042084.

[87] A. Bashir, T.I. Awan, A. Tehseen, M.B. Tahir, M. Ijaz, Interfaces and surfaces, in: Chem. Nanomater., Elsevier, 2020: pp. 51–87. https://doi.org/10.1016/B978-0-12-818908-5.00003-2.

[88] C. D'Alessandro, D. De Maio, A. Caldarelli, M. Musto, F. Di Giamberardino, M. Monti,

T. Mundo, E. Di Gennaro, R. Russo, V.G. Palmieri, Calorimetric testing of solar thermal absorbers for high vacuum flat panels, Sol. Energy. 243 (2022) 81–90. https://doi.org/10.1016/j.solener.2022.07.039.

[89] C. D'Alessandro, D. De Maio, T. Mundo, M. Musto, F. Di Giamberardino, M. Monti, D. Dalena, V.G. Palmieri, D. De Luca, E. Di Gennaro, R. Russo, Low cost high intensity LED illumination device for high uniformity solar testing, Sol. Energy. 221 (2021) 140–147. https://doi.org/10.1016/j.solener.2021.04.017.

[90] C.D. Alessandro, D. De Maio, D. De Luca, M. Musto, E. Di Gennaro, G. Rotondo, D. Dalena, R. Russo, Measurements of Spectrally Averaged Absorptivity and Emissivity for a Selective Solar Absorber in High Vacuum Under Direct Solar Illumination, J. Phys. Conf. Ser. 1599 (2020) 012027. https://doi.org/10.1088/1742-6596/1599/1/012027.

[91] R. Russo, M. Monti, C. D'Alessandro, D. De Maio, M. Musto, C. Koral, A. Andreone, F. Di Giamberardino, V.G. Palmieri, The Absorptance of Selective Solar Absorber Working in High Vacuum, in: 20th Ital. Natl. Conf. Photonic Technol. (Fotonica 2018), Institution of Engineering and Technology, 2018: pp. 56 (4 pp.)-56 (4 pp.). https://doi.org/10.1049/cp.2018.1665.

[92] D. De Maio, C.D. Alessandro, D. De Luca, M. Musto, E. Di Gennaro, G. Rotondo, R. Russo, Thermal Efficiency of a Concentrating Solar Collector Under High-Vacuum, J. Phys. Conf. Ser. 1599 (2020) 012029. https://doi.org/10.1088/1742-6596/1599/1/012029.

[93] Spectroscopic Ellipsometry - HORIBA, (n.d.). https://www.horiba.com/en_en/products/scientific/surface-characterization/spectroscopic-ellipsometry/.

[94] A.R. Forouhi, I. Bloomer, Optical dispersion relations for amorphous semiconductors and amorphous dielectrics, Phys. Rev. B. 34 (1986) 7018–7026. https://doi.org/10.1103/PhysRevB.34.7018.

[95] A.R. Forouhi, I. Bloomer, Optical properties of crystalline semiconductors and dielectrics, Phys. Rev. B. 38 (1988) 1865–1874. https://doi.org/10.1103/PhysRevB.38.1865.

[96] D. Barchiesi, T. Grosges, Fitting the optical constants of gold, silver, chromium, titanium, and aluminum in the visible bandwidth, J. Nanophotonics. 8 (2014) 083097. https://doi.org/10.1117/1.JNP.8.083097.

[97] D.-H. Lee, N.-G. Cho, Assessment of surface profile data acquired by a stylus profilometer, Meas. Sci. Technol. 23 (2012) 105601. https://doi.org/10.1088/0957-0233/23/10/105601.

[98] Alanod, (n.d.). https://alanod.com/.

[99] ALMECO GROUP - Alluminio - ALMECO GROUP, (n.d.). https://www.almecogroup.com/it.

[100] N.H. Thomas, Z. Chen, S. Fan, A.J. Minnich, Semiconductor-based Multilayer Selective

Solar Absorber for Unconcentrated Solar Thermal Energy Conversion, Sci. Rep. 7 (2017) 5362. https://doi.org/10.1038/s41598-017-05235-x.

[101] X.-F. Li, Y.-R. Chen, J. Miao, P. Zhou, Y.-X. Zheng, L.-Y. Chen, Y.-P. Lee, High solar absorption of a multilayered thin film structure, Opt. Express. 15 (2007) 1907. https://doi.org/10.1364/OE.15.001907.

[102] A.B. Khelifa, S. Khamlich, Z.Y. Nuru, L. Kotsedi, A. Mebrahtu, M. Balgouthi, A.A. Guizani, W. Dimassi, M. Maaza, Growth and characterization of spectrally selective Cr2O3/Cr/Cr2O3 multilayered solar absorber by e-beam evaporation, J. Alloys Compd. 734 (2018) 204–209. https://doi.org/10.1016/j.jallcom.2017.11.036.

[103] A.B. Khelifa, A. Soum-Glaude, S. Khamlich, H. Glénat, M. Balghouthi, A.A. Guizani, M. Maaza, W. Dimassi, Optical simulation, characterization and thermal stability of Cr2O3/Cr/Cr2O3multilayer solar selective absorber coatings, J. Alloys Compd. 783 (2019) 533–544. https://doi.org/10.1016/j.jallcom.2018.12.286.

[104] D. De Maio, C. D'Alessandro, A. Caldarelli, D. De Luca, E. Di Gennaro, R. Russo, M. Musto, A Selective Solar Absorber for Unconcentrated Solar Thermal Panels, Energies. 14 (2021) 900. https://doi.org/10.3390/en14040900.

[105] D. De Maio, C. D'Alessandro, A. Caldarelli, D. De Luca, E. Di Gennaro, M. Casalino, M. Iodice, M. Gioffre, R. Russo, M. Musto, Multilayers for efficient thermal energy conversion in high vacuum flat solar thermal panels, Thin Solid Films. 735 (2021) 138869. https://doi.org/10.1016/j.tsf.2021.138869.

[106] A.D. Rakić, A.B. Djurišić, J.M. Elazar, M.L. Majewski, Optical properties of metallic films for vertical-cavity optoelectronic devices, Appl. Opt. 37 (1998) 5271. https://doi.org/10.1364/AO.37.005271.

[107] H.C. Barshilia, N. Selvakumar, K.S. Rajam, A. Biswas, Structure and optical properties of pulsed sputter deposited CrxOy/Cr/Cr2O3 solar selective coatings, J. Appl. Phys. 103 (2008) 023507. https://doi.org/10.1063/1.2831364.

[108] M.F. Al-Kuhaili, S.M.A. Durrani, Optical properties of chromium oxide thin films deposited by electron-beam evaporation, Opt. Mater. (Amst). 29 (2007) 709–713. https://doi.org/10.1016/j.optmat.2005.11.020.

[109] R. Boidin, T. Halenkovič, V. Nazabal, L. Beneš, P. Němec, Pulsed laser deposited alumina thin films, Ceram. Int. 42 (2016) 1177–1182. https://doi.org/10.1016/j.ceramint.2015.09.048.

[110] M.A. Muriel, A. Carballar, Internal field distributions in fiber Bragg gratings, IEEE Photonics Technol. Lett. 9 (1997) 955–957. https://doi.org/10.1109/68.593364.

[111] D.W.B. Brace, P. Prevost, B. Stewart, G. Kirchhoff, R. Bunsen, The Laws of Radiation and Absorption: Memoirs by Prévost, Stewart, Kirchhoff, and Kirchhoff and Bunsen, 1901.

[112] R. Siegel, J.R. Howell, Thermal Radiation Heat Transfer, Hemisphere Publishing Corporation, 1981. http://ntrs.nasa.gov/archive/nasa/casi.ntrs.nasa.gov/19710021465.pdf.

[113] R. Keçili, S. Büyüktiryaki, C.M. Hussain, Engineered Nanosensors Based on Molecular Imprinting Technology, in: Handb. Nanomater. Ind. Appl., Elsevier, 2018: pp. 1031–1046. https://doi.org/10.1016/B978-0-12-813351-4.00059-6.

[114] Solar Electric Power Generation, Springer Berlin Heidelberg, Berlin, Heidelberg, 2006. https://doi.org/10.1007/978-3-540-31346-5.

[115] Engineered Nanomaterials for Energy Applications, in: Handb. Nanomater. Ind. Appl., Elsevier, 2018: pp. 751–767. https://doi.org/10.1016/B978-0-12-813351-4.00043-2.

[116] O.E. Semonin, J.M. Luther, M.C. Beard, Quantum dots for next-generation photovoltaics, Mater. Today. 15 (2012) 508–515. https://doi.org/10.1016/S1369-7021(12)70220-1.

[117] I. Fraunhofer Institute for Solar Energy Systems, PHOTOVOLTAICS REPORT, (n.d.). https://www.ise.fraunhofer.de/content/dam/ise/de/documents/publications/studies/Photovoltaics-Report.pdf.

[118] V. Rinnerbauer, S. Ndao, Y.X. Yeng, W.R. Chan, J.J. Senkevich, J.D. Joannopoulos, M. Soljačić, I. Celanovic, Recent developments in high-temperature photonic crystals for energy conversion, Energy Environ. Sci. 5 (2012) 8815. https://doi.org/10.1039/c2ee22731b.

[119] M. Herrando, C.N. Markides, Hybrid PV and solar-thermal systems for domestic heat and power provision in the UK: Techno-economic considerations, Appl. Energy. 161 (2016) 512–532. https://doi.org/10.1016/j.apenergy.2015.09.025.

[120] I. Guarracino, J. Freeman, N. Ekins-Daukes, C.. Markides, PERFORMANCE ASSESSMENT AND COMPARISON OF SOLAR ORC AND HYBRID PVT SYSTEMS FOR THE COMBINED DISTRIBUTED GENERATION OF DOMESTIC HEAT AND POWER, in: 12th Int. Conf. Heat Transf. Fluid Mech. Thermodyn., 2016.

[121] B. Sanner, L. Angelino, M. De Gregorio, W. Haslinger, A. Kujbus, S. Landolina, W. Sparber, W. van Helden, Strategic Research and Innovation Agenda for Renewable Heating & Cooling, 2013.

[122] A. de La Tour, M. Glachant, Y. Ménière, Predicting the costs of photovoltaic solar modules in 2020 using experience curve models, Energy. 62 (2013) 341–348. https://doi.org/10.1016/j.energy.2013.09.037.

[123] A. Mellor, D. Alonso Alvarez, I. Guarracino, A. Ramos, A. Riverola Lacasta, L. Ferre Llin, A.J. Murrell, D.J. Paul, D. Chemisana, C.N. Markides, N.J. Ekins-Daukes, Roadmap for the next-generation of hybrid photovoltaic-thermal solar energy collectors, Sol. Energy. 174 (2018) 386–398. https://doi.org/10.1016/j.solener.2018.09.004.

[124] S. Hassan, C.F. Doiron, G. V. Naik, Optimum selective emitters for efficient thermophotovoltaic conversion, Appl. Phys. Lett. 116 (2020) 023903.

https://doi.org/10.1063/1.5131367.

[125] C. Meola, G.M. Carlomagno, Recent advances in the use of infrared thermography, Meas. Sci. Technol. 15 (2004) R27–R58. https://doi.org/10.1088/0957-0233/15/9/R01.

[126] A.P. Raman, M.A. Anoma, L. Zhu, E. Rephaeli, S. Fan, Passive radiative cooling below ambient air temperature under direct sunlight, Nature. 515 (2014) 540–544. https://doi.org/10.1038/nature13883.

[127] N.N. Shi, C.-C. Tsai, F. Camino, G.D. Bernard, N. Yu, R. Wehner, Keeping cool: Enhanced optical reflection and radiative heat dissipation in Saharan silver ants, Science (80-.). 349 (2015) 298–301. https://doi.org/10.1126/science.aab3564.

[128] B.H. Stuart, Infrared Spectroscopy: Fundamentals and Applications, Wiley, 2004. https://doi.org/10.1002/0470011149.

[129] Y. De Wilde, F. Formanek, R. Carminati, B. Gralak, P.-A. Lemoine, K. Joulain, J.-P. Mulet, Y. Chen, J.-J. Greffet, Thermal radiation scanning tunnelling microscopy, Nature. 444 (2006) 740–743. https://doi.org/10.1038/nature05265.

[130] W.E.S.W.A. Rashid, P.J. Ker, M.Z. Bin Jamaludin, M.M.A. Gamel, H.J. Lee, N.B.A. Rahman, Recent Development of Thermophotovoltaic System for Waste Heat Harvesting Application and Potential Implementation in Thermal Power Plant, IEEE Access. 8 (2020) 105156–105168. https://doi.org/10.1109/ACCESS.2020.2999061.

[131] Z. Wang, D. Kortge, Z. He, J. Song, J. Zhu, C. Lee, H. Wang, P. Bermel, Selective emitter materials and designs for high-temperature thermophotovoltaic applications, Sol. Energy Mater. Sol. Cells. 238 (2022) 111554. https://doi.org/10.1016/j.solmat.2021.111554.

[132] J.-J. Greffet, R. Carminati, K. Joulain, J.-P. Mulet, S. Mainguy, Y. Chen, Coherent emission of light by thermal sources, Nature. 416 (2002) 61–64.

[133] D.M. Bierman, A. Lenert, W.R. Chan, B. Bhatia, I. Celanović, M. Soljačić, E.N. Wang, Enhanced photovoltaic energy conversion using thermally based spectral shaping, Nat. Energy. 1 (2016) 16068. https://doi.org/10.1038/nenergy.2016.68.

[134] M. Chirumamilla, G.V. Krishnamurthy, K. Knopp, T. Krekeler, M. Graf, D. Jalas, M. Ritter, M. Störmer, A.Y. Petrov, M. Eich, Metamaterial emitter for thermophotovoltaics stable up to 1400 °C, Sci. Rep. 9 (2019) 7241. https://doi.org/10.1038/s41598-019-43640-6.

[135] P. Hidnert, W.T. Sweeney, Scientific Papers of the Bureau of Standards: Thermal Expansion of Tungsten, Sci. Pap. Bur. Stand. 20 (1925) 483. https://nvlpubs.nist.gov/nistpubs/ScientificPapers/nbsscientificpaper515vol20p483_A2b.pdf.

[136] C.-L. Tien, T.-W. Lin, Thermal expansion coefficient and thermomechanical properties of SiN x thin films prepared by plasma-enhanced chemical vapor deposition, Appl. Opt. 51 (2012) 7229. https://doi.org/10.1364/AO.51.007229.

[137] C. Tsou, Y.S. Huang, H.C. Li, T.H. Lai, Determination of thermal expansion coefficient of thermal oxide, Sensors Mater. 17 (2005) 441–451.

[138] H.M. Albetran, Thermal expansion coefficient determination of pure, doped, and co-doped anatase nanoparticles heated in sealed quartz capillaries using in-situ high-temperature synchrotron radiation diffraction, Heliyon. 6 (2020) e04501. https://doi.org/10.1016/j.heliyon.2020.e04501.

[139] W. Shockley, H. Queisser, Detailed Balance Limit of Efficiency of p–n Junction Solar Cells, J. Appl. Phys. 32 (1961) 35–54. https://doi.org/10.1063/1.1736034.

[140] H. Nejadriahi, A. Friedman, R. Sharma, S. Pappert, Y. Fainman, P. Yu, Thermo-optic properties of silicon-rich silicon nitride for on-chip applications, Opt. Express. 28 (2020) 24951. https://doi.org/10.1364/OE.396969.

[141] L. Gao, F. Lemarchand, M. Lequime, Exploitation of multiple incidences spectrometric measurements for thin film reverse engineering, Opt. Express. 20 (2012) 15734. https://doi.org/10.1364/OE.20.015734.

[142] T. Siefke, S. Kroker, K. Pfeiffer, O. Puffky, K. Dietrich, D. Franta, I. Ohlídal, A. Szeghalmi, E. Kley, A. Tünnermann, Materials Pushing the Application Limits of Wire Grid Polarizers further into the Deep Ultraviolet Spectral Range, Adv. Opt. Mater. 4 (2016) 1780–1786. https://doi.org/10.1002/adom.201600250.

[143] R. Bhatt, I. Kravchenko, M. Gupta, High-efficiency solar thermophotovoltaic system using a nanostructure-based selective emitter, Sol. Energy. 197 (2020) 538–545. https://doi.org/10.1016/j.solener.2020.01.029.

[144] W.R. Chan, V. Stelmakh, M. Ghebrebrhan, M. Soljačić, J.D. Joannopoulos, I. Čelanović, Enabling efficient heat-to-electricity generation at the mesoscale, Energy Environ. Sci. 10 (2017) 1367–1371. https://doi.org/10.1039/C7EE00366H.

[145] M. Shimizu, A. Kohiyama, H. Yugami, High-efficiency solar-thermophotovoltaic system equipped with a monolithic planar selective absorber/emitter, J. Photonics Energy. 5 (2015) 053099. https://doi.org/10.1117/1.JPE.5.053099.

[146] S. Roberts, Optical Properties of Nickel and Tungsten and Their Interpretation According to Drude's Formula, Phys. Rev. 114 (1959) 104–115. https://doi.org/10.1103/PhysRev.114.104.

[147] J. Šik, J. Hora, J. Humlíček, Optical functions of silicon at high temperatures, J. Appl. Phys. 84 (1998) 6291–6298. https://doi.org/10.1063/1.368951.

[148] H.H. Li, Refractive index of silicon and germanium and its wavelength and temperature derivatives, J. Phys. Chem. Ref. Data. 9 (1980) 561–658. https://doi.org/10.1063/1.555624.

[149] C.Z. Tan, J. Arndt, Temperature dependence of refractive index of glassy SiO2 in the infrared wavelength range, J. Phys. Chem. Solids. 61 (2000) 1315–1320.

https://doi.org/10.1016/S0022-3697(99)00411-4.

[150] F. Zhang, R.-J. Zhang, D.-X. Zhang, Z.-Y. Wang, J.-P. Xu, Y.-X. Zheng, L.-Y. Chen, R.-Z. Huang, Y. Sun, X. Chen, X.-J. Meng, N. Dai, Temperature-Dependent Optical Properties of Titanium Oxide Thin Films Studied by Spectroscopic Ellipsometry, Appl. Phys. Express. 6 (2013) 121101. https://doi.org/10.7567/APEX.6.121101.

[151] P. Bermel, M. Ghebrebrhan, W. Chan, Y.X. Yeng, M. Araghchini, R. Hamam, C.H. Marton, K.F. Jensen, M. Soljačić, J.D. Joannopoulos, S.G. Johnson, I. Celanovic, Design and global optimization of high-efficiency thermophotovoltaic systems, Opt. Express. 18 (2010) A314. https://doi.org/10.1364/OE.18.00A314.

[152] S. Rühle, Tabulated values of the Shockley–Queisser limit for single junction solar cells, Sol. Energy. 130 (2016) 139–147. https://doi.org/10.1016/j.solener.2016.02.015.

[153] A. Olivares, J. Rekstad, M. Meir, S. Kahlen, G. Wallner, Degradation model for an extruded polymeric solar thermal absorber, Sol. Energy Mater. Sol. Cells. 94 (2010) 1031–1037. https://doi.org/10.1016/j.solmat.2010.02.001.

[154] M. Köhl, M. Heck, S. Brunold, U. Frei, B. Carlsson, K. Möller, Advanced procedure for the assessment of the lifetime of solar absorber coatings, Sol. Energy Mater. Sol. Cells. 84 (2004) 275–289. https://doi.org/10.1016/j.solmat.2004.01.041.

[155] B. Carlsson, K. Möller, M. Köhl, U. Frei, S. Brunold, Qualification test procedure for solar absorber surface durability, Sol. Energy Mater. Sol. Cells. 61 (2000) 255–275. https://doi.org/10.1016/S0927-0248(99)00111-7.

[156] MathWorks, Inc., (n.d.). https://it.mathworks.com/products/simulink.html.

[157] S.A. Kalogirou, Solar thermal collectors and applications, Prog. Energy Combust. Sci. 30 (2004) 231–295. https://doi.org/10.1016/j.pecs.2004.02.001.

[158] W.J. Platzer, D. Mills, W. Gardner, Linear Fresnel Collector (LFC) solar thermal technology, in: Conc. Sol. Power Technol., Elsevier, 2021: pp. 165–217. https://doi.org/10.1016/B978-0-12-819970-1.00006-2.

[159] S. Hess, V.I. Hanby, Collector Simulation Model with Dynamic Incidence Angle Modifier for Anisotropic Diffuse Irradiance, Energy Procedia. 48 (2014) 87–96. https://doi.org/10.1016/j.egypro.2014.02.011.

[160] ISO 9806:2017 Solar energy — Solar thermal collectors — Test methods, (n.d.). https://www.iso.org/standard/67978.html.

[161] W.R. McIntire, Factored approximations for biaxial incident angle modifiers, Sol. Energy. 29 (1982) 315–322. https://doi.org/10.1016/0038-092X(82)90246-8.

[162] Solar radiation tool of the Joint Research Centre (JRC), (n.d.). https://re.jrc.ec.europa.eu/pvg_tools/it/#MR.

[163] S. Wang, F. Chen, R. Ji, M. Hou, F. Yi, W. Zheng, T. Zhang, W. Lu, Large-Area Low-

Cost Dielectric Perfect Absorber by One-Step Sputtering, Adv. Opt. Mater. 7 (2019) 1801596. https://doi.org/10.1002/adom.201801596.

[164] I. Latchford, A. Riposan, V. Kudriavtsev, T. Bluck, C. Smith, Cost of Ownership Analysis for a High Productivity Thin Film PVD System, in: 2015: pp. 516–519. https://doi.org/10.14332/svc14.proc.1883.

[165] B. Carlsson, Suitability analysis of selective solar absorber surfaces based on a total cost accounting approach, Sol. Energy Mater. Sol. Cells. 91 (2007) 1338–1349. https://doi.org/10.1016/j.solmat.2007.05.011.

[166] F. Alnaimat, Y. Rashid, Thermal Energy Storage in Solar Power Plants: A Review of the Materials, Associated Limitations, and Proposed Solutions, Energies. 12 (2019) 4164. https://doi.org/10.3390/en12214164.

[167] E. Risueño, S. Doppiu, J. Rodríguez-Aseguinolaza, P. Blanco, A. Gil, M. Tello, A. Faik, B. D'Aguanno, Experimental investigation of Mg-Zn-Al metal alloys for latent heat storage application, J. Alloys Compd. 685 (2016) 724–732. https://doi.org/10.1016/j.jallcom.2016.06.222.

[168] A. Bayon, R. Bader, M. Jafarian, L. Fedunik-Hofman, Y. Sun, J. Hinkley, S. Miller, W. Lipiński, Techno-economic assessment of solid–gas thermochemical energy storage systems for solar thermal power applications, Energy. 149 (2018) 473–484. https://doi.org/10.1016/j.energy.2017.11.084.

[169] A. Awad, A. Burns, M. Waleed, M. Al-Yasiri, D. Wen, Latent and sensible energy storage enhancement of nano-nitrate molten salt, Sol. Energy. 172 (2018) 191–197. https://doi.org/10.1016/j.solener.2018.04.012.

[170] N. Bianco, S. Busiello, M. Iasiello, G.M. Mauro, Finned heat sinks with phase change materials and metal foams: Pareto optimization to address cost and operation time, Appl. Therm. Eng. 197 (2021) 117436. https://doi.org/10.1016/j.applthermaleng.2021.117436.